UCL Université catholique de Louvain

École polytechnique de Louvain (EPL)

Design and implementation of a test bench for an aerospike nozzle

Dissertation presented by
Diego GARCIA WEBER , Antoine MAINDIAUX

for obtaining the Master's degree in
Electro-mechanical & Mechanical Engineering

Supervisor(s)
Yann BARTOSIEWICZ, Philippe CHATELAIN

Reader(s)
Vincent LEGAT, Tony ARTS

Academic year 2015-2016

Acknowledgements

At the end of our thesis we would like to thank all the people who made this work possible and helped us in all the time of research and writing.

First of all, we would like to express our deepest sense of gratitude to our supervisors Professors Yann Bartosiewicz and Philippe Chatelain, for their guidance, their patience and their continuous advice and encouragement throughout this work.

Besides our advisors, we would like to thank Olivier Lamberts, research assistant and Ph.D. student associated to this thesis, for his insightful comments and his passionate participation, and for making himself available all along this work.

We would also like to acknowledge the different technicians and research assistants from the TFL department as well as the other professionals we worked with for their time and precious help in the implementation of the test bench. More specifically we would like to thank:

- François Vercheval for his precious advices during the design steps of the nozzle and the set up of the test bench.
- Yan Liu and Julien Vervotte for their assistance all along the assembly, set up and utilization of the test bench.
- The technicians from AF compressors for their help during the use of the compressor.
- Hervé Laurent and his team for his reactivity and excellent work during the machining of the designed nozzle.

Last but not the least, we would like to thank our families and friends for their unfailing support and continuous encouragement throughout our years of study. This accomplishment would not have been possible without them.

Table of contents

List of Figures

List of Symbols

Introduction **1**

1 Nozzle pre-design **5**
1.1 Assumptions . . . 5
1.2 Methodology . . . 7
1.2.1 Design parameters . . . 7
1.2.2 Procedure . . . 7
1.3 Geometry . . . 10
1.3.1 Limiting parameters and criteria of choice . . . 10
1.3.2 Final geometry and flow characteristics . . . 11

2 Simulations **13**
2.1 Numerical model . . . 13
2.1.1 Categorization of the flow . . . 13
2.1.2 Turbulence model . . . 14
2.2 Parametrization . . . 15
2.2.1 Mesh . . . 15
2.2.2 Boundary conditions . . . 18
2.3 Validations . . . 19
2.4 Simulation results . . . 21

3 Design **27**
3.1 Test bench description . . . 27
3.1.1 Air intake system . . . 28
3.1.2 Visualization by Shadowgraph . . . 30
3.1.3 User interface . . . 33
3.2 Design and assembly . . . 34

3.2.1 Transition piece 36
3.2.2 Nozzle 37
3.2.3 Chimneys and secondary flows 44

4 Experimental results **47**
4.1 Phenomena description 47
4.2 Standard flows results and comparison with simulations 50
4.3 Air-ejecting flow results 55
4.3.1 Secondary flow valves 55
4.3.2 Closing mechanism 58
4.4 Major issues 63

Conclusions **66**

A Design blueprints **71**

B Lab procedure **79**

Bibliography **89**

List of Figures

1 Aerospike/Bell nozzle exhaust plume comparisons [1] 3

1.1 Axes definition for the bi-dimensional hypothesis. 6
1.2 Core design parameters of the nozzle. 7
1.3 Altitude compensation effect of an aerospike nozzle [2]. 8
1.4 Parameters choice procedure. 9
1.5 Final geometry main characteristics. 11

2.1 Simulation mesh with zoom on the throat. 18
2.2 Simulation mesh with different boundaries. 19
2.3 Evolution of the mass within the simulation domain. 20
2.4 Mach number distribution over the symmetry plane for various refinement of the mesh. 21
2.5 Simulations with $p_0 = 2$ $[bar]$, Mach number and pressure. 22
2.6 Simulations with $p_0 = 4$ $[bar]$, Mach number and pressure. 23
2.7 Simulations with $p_0 = 8$ $[bar]$, Mach number and pressure. 24
2.8 Simulations with $p_0 = 10$ $[bar]$, Mach number and pressure. 25

3.1 3D representation of the complete test bench. 27
3.2 Compressor [19]. 28
3.3 Air tank [19]. 28
3.4 P&ID of the test bench. 28
3.5 Differential pressure flow-meter. 29
3.6 Shadowgraph principle [11]. 30
3.7 Layout of the shadowgraph installation. 31
3.8 The shadowgraph installation. 32
3.9 Observation of a burning match through the shadowgraph. 33
3.10 Test bench user interface. 33
3.11 Final design of the aerospike nozzle. 34
3.12 Split view of the three main parts of the nozzle and the connection back-piece. 35
3.13 Inlet of the nozzle. 36

3.14 Outlet of the compressor pipe. 36
3.15 Transition piece. 36
3.16 Split view of the nozzle. 37
3.17 The canal. 38
3.18 Von Mises Stress for a uniform pressure of 10 *bar*. 40
3.19 Von Mises stress for a 10 *bar* pressure applied on a 40 *mm* radius circular area around the spike. 41
3.20 Von Mises stress for a 10 *bar* pressure applied on two 10 *mm* radius circular areas around the throats. 42
3.21 Plexiglas frame. 43
3.22 Exterior frame and O-ring joint seated in the frame groove. 43
3.23 Sealing and alignment are ensured by the exterior frame. 43
3.24 Secondary flow chimneys. 44

4.1 Sketch of compressible flow phenomena within an aerospike nozzle. 48
4.2 Initial flow angle α as a function of the ratio p_0/p_a. 50
4.3 Shadowgraph visualization of the flow around the spike for $p_0 = 2\,bar$ (bottom) and equivalent numerical shadowgraph (top). 51
4.4 Shadowgraph visualization of the flow around the spike for $p_0 = 4\,bar$ (bottom) and equivalent numerical shadowgraph (top). 52
4.5 Shadowgraph visualization of the flow around the spike for $p_0 = 6\,bar$ (bottom) and equivalent numerical shadowgraph (top). 52
4.6 Shadowgraph visualization of the flow at the throat with schematics of phenomena. 53
4.7 Shadowgraph visualization of the flow at the end of the spike with schematics of phenomena on one side of the flow. 54
4.8 Shadowgraph visualization of the flow at the throat with wave curvature drawing. 55
4.9 Shadowgraph comparison between flows for open and closed chimneys. 56
4.10 Pressure measurements for flows in open and closed chimneys configurations. 57
4.11 Sketch of the flow deflection. 58
4.12 Simulation view of positive and negative horizontal velocities within the canal and closing mechanism. 58
4.13 Closing mechanism designed to be attached downstream of the nozzle. 59
4.14 Shadowgraph visualization of the flow around the spike for different outlet apertures. 60
4.15 Secondary flow pressure as a function of the motive pressure for an outlet aperture of 90 *mm*. 60
4.16 Secondary flow pressure as a function of the motive pressure for an outlet aperture of 60 *mm*. 61

4.17 Secondary flow pressure as a function of the motive pressure for an outlet aperture of 40 mm. 61
4.18 Secondary flow pressure as a function of the motive pressure for an outlet aperture of 30 mm. 62
4.19 Secondary flow pressure as a function of the motive pressure for different outlet apertures. 62
4.20 Condensation created within the nozzle when conducting tests with open chimneys. 64
4.21 Additional piece for limiting the noises generated by the air flow through the nozzle. 69

List of Symbols

Symbols	Units	Description
θ	$^\circ$	Throat angle
γ	$-$	Heat capacity ratio
μ	$kg/(m \cdot s)$	Dynamic (shear) viscosity
ν	m^2/s	Kinematic viscosity
ν_t	m^2/s	Eddy viscosity
ρ	kg/m^3	Density
σ_{el}	MPa	Yield strength
τ_w	N/m^2	Wall shear stress
D	m	Diameter
A_c	m^2	Throat area
c	m/s	Sound velocity
C	$-$	Discharge coefficient
C_f	$-$	Skin friction coefficient
h_c	m	Throat height
M	$-$	Mach number
n	m/s	Refractive index
p	Pa	Static pressure
p_0	Pa	Stagnation pressure
p_a	Pa	Atmospheric pressure
$\dot{m}$	kg/s	Mass flow rate
Q_v	m^3/s	Volumetric flow rate
r	m	Radius
R^*	$J \cdot kg^{-1} \cdot K^{-1}$	Universal gas constant
Re_D	$-$	Reynolds number
T_0	K	Stagnation temperature
u	m/s	Fluid velocity
$\overline{u}_\tau$	m/s	Shear velocity
V	$-$	Abbe Number, or constringence
W	m	Canal width

Introduction

Context

Numerous mechanics-related fields require a deep and complete understanding of compressible fluid flows. At the Université catholique de Louvain, these flows are more particularly studied during the courses of *Fluid mechanics and Transfers II [LMECA2322]* for flows within converging and diverging nozzles, and *Aerodynamics of external flows [LMECA2323]* for external compressible flows. The simplified approach and the underlying assumptions used during these lectures however make the theoretical results slightly differ from the real behaviour of compressible flows.

In order to confront this theory with real flows, two methods can be implemented. The first one is numerical simulation of the studied compressible flows. This first method is very time consuming, requires a lot of computing resources and still implies the use of numerical models to approximate reality. It is thus not very practical for teaching purposes. The second option is the use of a test bench that allows student to visualize, observe and measure the properties of real flows in different situations. This method is by far the best to give students a practical insight into the behaviour of compressible flows.

The objective of this thesis is to design and implement such a test bench, allowing the visualization of the air flow within and around an aerospike nozzle. This type of nozzle offers the opportunity to observe an internal subsonic flow (within the convergent) as well as an external supersonic flow in contact with air at atmospheric conditions. A panel of phenomena can hence be visualized:

- A **sonic throat** separating a subsonic convergent section and a supersonic divergent section.

- A Prandtl-Meyer **expansion wave** due to the convex deviation of the flow, accelerating the air from sonic to supersonic velocity.

- Several oblique **compression shocks** downstream from the nozzle due to the sudden pressure change once the supersonic flow interacts with the ambient air.

- A **transonic shear layer** separating the supersonic flow exhausting from the nozzle and the driven subsonic flow of ambient air.

This wide range of observable phenomena makes the use of an aerospike nozzle experiment particularly suited to teaching purposes.

Furthermore, aerospike nozzles have aerospace propulsion as main application domain, where they differ from conventional "bell" shaped nozzle thanks to the *altitude compensation* effect illustrated on figure 1. It can be seen that, as the atmospheric pressure drops due to the rise of the vehicle, the plume of supersonic, hot exhaust gases changes in shape along the spike of the nozzle.

In a conventional bell-shaped nozzle the exhaust gases are expanded and accelerated to supersonic velocities in the bell exclusively through a increase in flow cross section. The shape of the bell nozzle being fixed, the expansion ratio is fixed. Unfortunately, the high atmospheric pressure encountered at low altitude can deform an over-expanded exhaust plume to the point of flow separation, as represented on the bottom left corner of figure 1. This effect leads to performance losses that can be critical in the case of a space launch vehicle. Inversely, low pressures encountered at high altitudes mean that the flow could be under-expanded. Thus, there is residual pressure within the flow at the end of the bell that could have been used to accelerate the exhaust gases even more and achieve more thrust.

The aerospike nozzle doesn't suffer from the flow separation effect and adapts its shape to the ambient pressure. This is due to the fact that it relies mainly on expansion through deviation of the flow once in contact with the atmosphere, and this deviation depends on the atmospheric pressure. Since the expansion will be different for different atmospheric pressures, and thus different altitudes, the term *altitude compensation* is often used to refer to this adaptation effect. The expansion change of the aerospike nozzle gives it a better overall efficiency over the whole ascent profile followed by space launch vehicles.

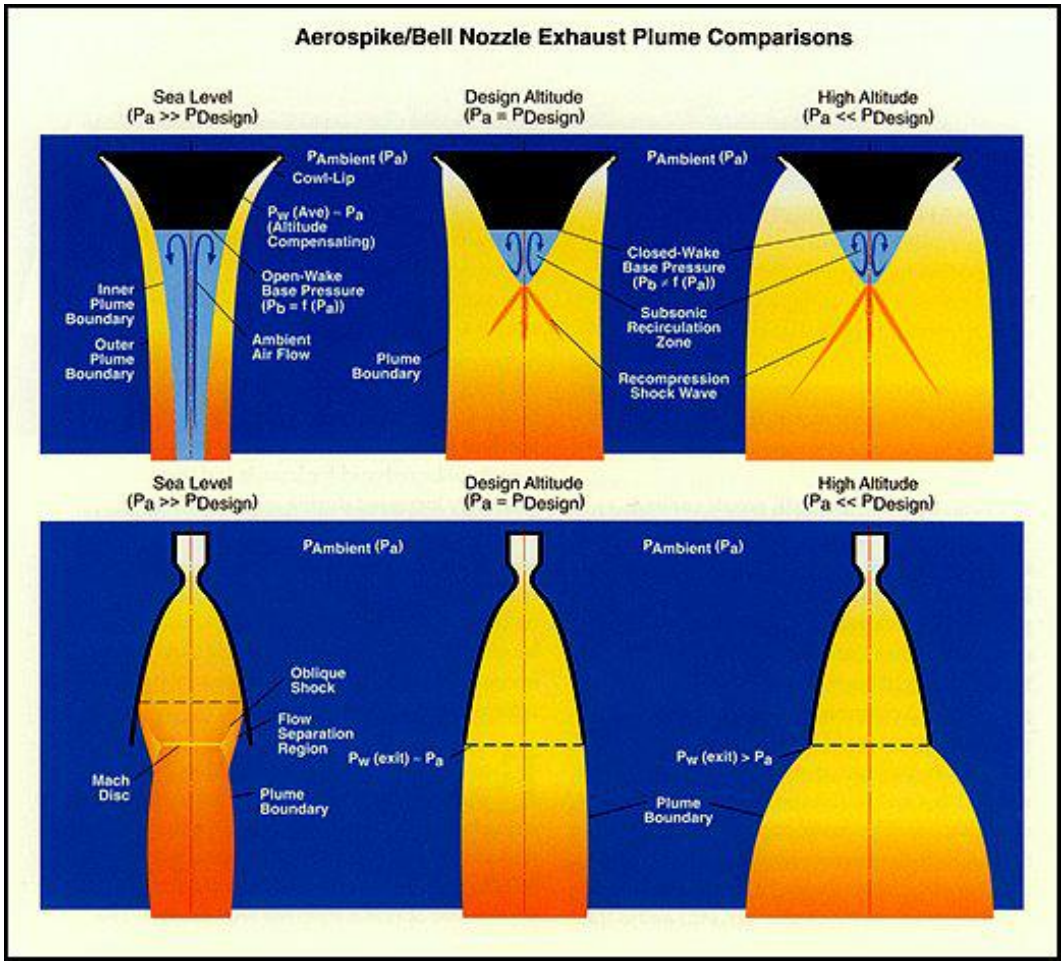

Figure 1: Aerospike/Bell nozzle exhaust plume comparisons [1] .

Objectives

Given that the test bench to be implemented is going to be used for teaching purposes, its design and operation have to be student friendly, this implies to take into account the following criteria:

- It must enable a good visualization of the air flow within the nozzle. Hence, reasonable dimensions have to be considered in order to allow students to observe as clearly as possible the different phenomena that characterize the flow.

- A user interface must be implemented, allowing the students to modify the stagnation pressure imposed at the nozzle inlet and to visualize the measured values during the experiment.
- The observation of the different conditions represented on figure 1.3 has to be possible because a potential application of aerospike nozzle is spacecraft propulsion as explained previously. This phenomenon of flow deformation with the atmospheric pressure, the *altitude compensation* effect, should increase the overall efficiency of the rocket engine during its ascent through the atmosphere and is a main reason for the work on aerospike nozzles in the industry.

This work is organised in four steps in order to achieve these goals.

First a uni-dimensional, pre-design analysis of the nozzle is achieved, relying on compressible flow theory. This allowed to establish the global characteristics of the geometry to implement in order to observe the expected phenomena.

Once those characteristics were established the OpenFOAM software was used to run bi-dimensional simulations of the flow at various regimes. These simulations confirmed the presence of the expected flow phenomena over the span of available regimes. Moreover numerical simulations helped in refining the spike geometry to avoid unexpected flow detachment and related shock waves as far as possible.

The third step was the design of the nozzle itself using SolidWorks and its integration in the pre-existing test-bench [19]. This design took into account all engineering issues relative to machining design such as good sealing of the flow, stresses on the various parts, precision of assembly and so on.

Finally the test bench was used to perform a range of experiments in order to test it and compare the results with the numerical simulations.

Chapter 1

Nozzle pre-design

In order to determine the main geometrical characteristics of the nozzle to be built, a theoretical pre-design analysis is required. This pre design is presented in this chapter. First, the different assumptions required in the various theoretical aspects addressed are discussed. The pre-design methodology and the limiting parameters that have to be taken into account are then described in detail. Finally, the chosen geometry to implement is disclosed.

1.1 Assumptions

Bi-dimensional flow

The flow is considered to be bi-dimensional, meaning that the effects of depth are neglected. The velocity vector of the fluid at any point of the flow is considered to only have components in the x direction (along the spike) and y direction, as represented in figure 1.1. This means that boundary layers on the side walls of the nozzle are neglected which is equivalent to considering a *perfect slip* flow on those walls.
This hypothesis will be confronted with the experimental results visualizations to asses the impact of depth effects.

Perfect gas

The air flowing through the nozzle is approximated as a perfect gas. Perfect gases are entirely defined by two parameters that are considered to be constant for all thermodynamic states:

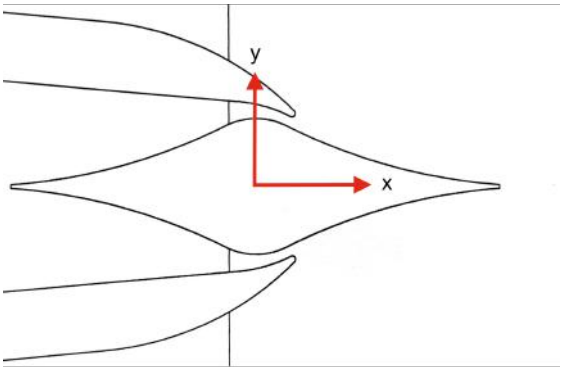

Figure 1.1: Axes definition for the bi-dimensional hypothesis.

- The **heat capacity ratio γ**

$$\gamma = \frac{C_p}{C_v} = \frac{7}{5} = 1.4\ [-]$$

- The **individual perfect gas constant R^***

$$R^* = \frac{R}{M_{m,\text{air}}} = 287.1\ [J/kgK]$$

Steady state flow

The studied flow is considered to be in a steady state. This hypothesis makes sense due to the air tank placed between the outlet of the compressor and the inlet of the nozzle. The tank acts as a damper and allows for a relatively constant mass flow rate within the pressure panel to be used.

Isentropic flow

The flow is considered to be isentropic all along the nozzle, which means that heat transfers and friction are neglected.
This hypothesis is only used for the nozzle pre-design, the numerical simulations disclosed later on do not use an inviscid flow model and thus do not neglect wall friction. Furthermore, the behaviour of the flow in the nozzle may eventually lead to shock waves which are, by definition, non isentropic.

1.2 Methodology

1.2.1 Design parameters

The two design parameters that are relevant for an aerospike nozzle are shown on figure 1.2 and are defined as:

- The **throat angle $\boldsymbol{\theta}$**. It is the angle between the throat plane and the vertical direction. It is thus also the angle between the direction of the flow at the throat (and thus the spike contour tangent at the throat), and its final direction which is horizontal.
- The **throat area $\boldsymbol{A_c} = 2 \cdot h \cdot W$** with h being the throat height and W the depth of the canal. The factor 2 comes from the choice of designing a double nozzle with a planar symmetry.

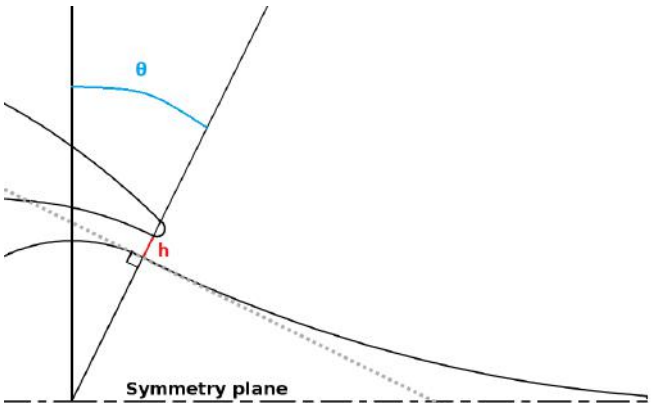

Figure 1.2: Core design parameters of the nozzle.

1.2.2 Procedure

The nozzle geometry will be set by considering the flow state when it is perfectly compensated by standard stagnant atmosphere (subfigure (b) of figure 1.3). The objective with this design point choice is to be able to visualize the different flow states with an atmospheric pressure of $p_a = 1\ [bar]$. Later design choices will however allow to lower the ambient pressure around the nozzle.

The first equation used is the **Prandtl-Meyer expansion function** $\nu(M)$, giving the required deviation angle of a sonic flow ($M = 1$) in order to reach a

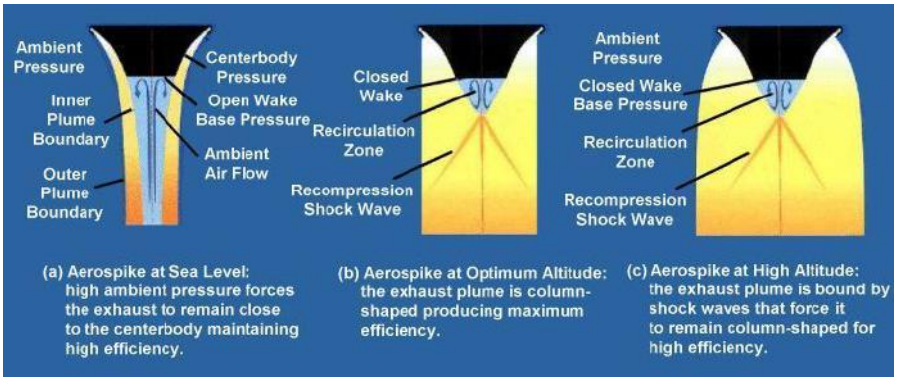

Figure 1.3: Altitude compensation effect of an aerospike nozzle [2].

final Mach number M.

$$\nu(M) = \sqrt{\frac{\gamma+1}{\gamma-1}} \arctan\left(\sqrt{\frac{\gamma-1}{\gamma+1}(M^2-1)}\right) - \arctan(\sqrt{M^2-1}) \; [rad] \qquad (1.1)$$

From this equation, with a fixed final Mach number M_f determined later in this procedure, the design angle θ of the throat will be computed so that $\theta = \nu(M_f)$.

The second equation used is the **pressure ratio** relation between the pressure of a supersonic flow over the stagnation pressure p_0 as a function of the Mach number M. In this case, the Mach number used is the one after the Prandtl-Meyer expansion, M_f.

$$\frac{p_0}{p} = \left(1 + \frac{\gamma-1}{2}M^2\right)^{\frac{\gamma}{\gamma-1}} \; [-] \qquad (1.2)$$

This relation is used to find the required stagnation pressure p_0 in order for the pressure beyond the Prandtl-Meyer expansion to be equal to the atmospheric pressure. Therefore, the flow pressure will be compensated by the atmospheric pressure and the altitude compensation effect will be optimal.

The final relation used gives the **mass flow rate** through the sonic throat as a function of the stagnation pressure p_0, the stagnation temperature T_0, the gas parameters γ and R, and the throat area A_c. By setting $\gamma = 1.4\,[-]$, $R = 287.1\,[J/kg \cdot K]$ and $T_0 = 298.15\,[K]$, this equation can be written in a more compact form, with only the two interesting parameters p_0 and A_c remaining :

$$\dot{m} = \left(\frac{2}{\gamma+1}\right)^{\frac{\gamma+1}{2(\gamma-1)}} \cdot \sqrt{\frac{\gamma}{R}} \frac{p_0}{\sqrt{T_0}} A_c = 2.34 \cdot 10^{-3} \cdot p_0 \cdot A_c \; [kg/s] \qquad (1.3)$$

This equation enables to establish the geometry characteristics of the throat, depending on the requested flow conditions and without exceeding the maximal mass flow rate of the compressor. Since a double rectangular throat profile was chosen, the throat area will be given by $A_c = 2 \cdot h \cdot W$.

The complete procedure can be visualized on figure 1.4. To summarize, the

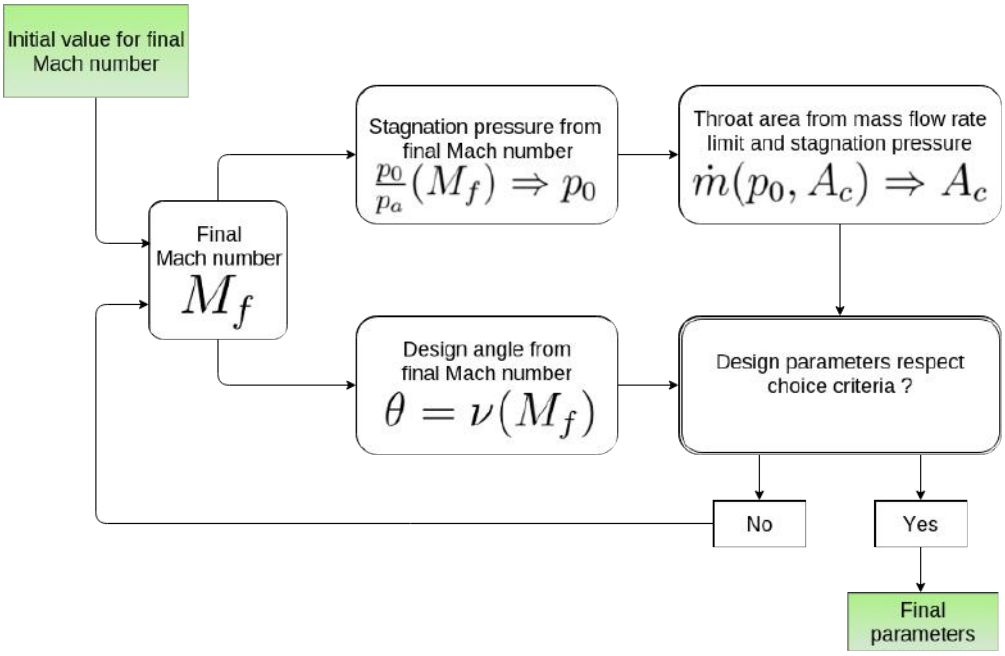

Figure 1.4: Parameters choice procedure.

procedure starts with an initial desired value for the final Mach number M_f, which in this case was set to 2.5 bar. Using this Mach number, the design angle θ and the stagnation pressure p_0 in order to have a supersonic flow pressure of 1 bar can be computed. Using the stagnation pressure computed and the known maximal mass flow rate of the compressor the throat area A_c is computed. The next step is to check if the design parameters computed respect the choice criteria and limiting parameters disclosed in the next subsection. If the choice criteria or limiting parameters are not respected iterations on the desired final Mach number M_f are required until reaching a group of parameters $(\theta\,,\, p_0\,,\, A_c)$ meeting the requirements.

1.3 Geometry

1.3.1 Limiting parameters and criteria of choice

Some parameters are limited by the equipment available (in this case the compressor), while other are dependant of the hypotheses previously made. Other parameters have to be chosen while taking into account the teaching purpose of the experiment and thus the importance of clear flow visualization.

Regarding the parameters limited by the compressor:

- The stagnation pressure p_0 is of course determined by the equipment. Although the compressor could theoretically provide pressurized air up to 40 bar, the experience will be limited to a maximal pressure level of 10 bar in the air-tank for security reasons.

- The mass flow rate $\dot{m}$ is also limited by the compressor. The theoretical upper limit of the volume flow rate is $\dot{V}_{max} = 1200\ [m_N^3/hour]$, which corresponds to a maximal mass flow rate of $\dot{m}_{max} = \dot{V}_{max} \cdot \rho_{\text{air}} = 0.43\ [kg/s]$.

The parameters to take into account in order to satisfy the previous assumptions are:

- A depth over height ratio $\frac{W}{h}$ as large as possible in order to be as close as possible to a bi-dimensional flow, where the depth effects are negligible. The throat total area will given by $A_c = 2 \cdot h \cdot W$ and will be determined by the compressor characteristics.

- A continuous convergent profile, without brutal changes of section, in order to be as close as possible to an isentropic flow as assumed and avoid any discontinuity that could lead to boundary layer detachment.

Finally for a better visualization, some design criteria need to be considered:

- The height h of each throat has to be large enough to allow a good visualization of the air flow.

- The dimensions and fixations of the spike have to be designed to withstand the pressure gradient and shear stresses generated by the air flow and to allow the observation of air expansion around the throat.

1.3.2 Final geometry and flow characteristics

The final core parameters chosen for the geometry are represented on figure 1.5, and are the following:

- A throat height of $h = 3\ [mm]$ and a nozzle depth of $W = 30\ [mm]$, giving a throat area of $A_c = 2 \cdot h \cdot W = 18 \cdot 10{-}5\ [m^2]$, and a depth over height ratio $\frac{W}{h} = 10\ [-]$.
- The nozzle throat forms a 26.5° angle with the vertical line, so the flow at the throat forms the same angle with the horizontal line.

With this geometry the final Mach number reached will be $M_f = 2.1\ [-]$ and the following flow states will be observable:

- For $1.9\ [bar] < p_0 < 7.8\ [bar]$ the flow will be over-expanded, as represented in subfigure (a) of figure 1.3.
- At $p_0 = 7.8\ [bar]$ the flow expansion will be optimal, as represented in subfigure (b) of figure 1.3.
- For $7.8\ [bar] < p_0 < 10\ [bar]$ the flow will be under-expanded, as represented in subfigure (a) of figure 1.3. At a pressure of $p_0 = 10\ [bar]$ the compressor will provide a mass flow rate of $\dot{m} = 0.35\ [kg/s]$, providing a safety margin compared to its maximum.

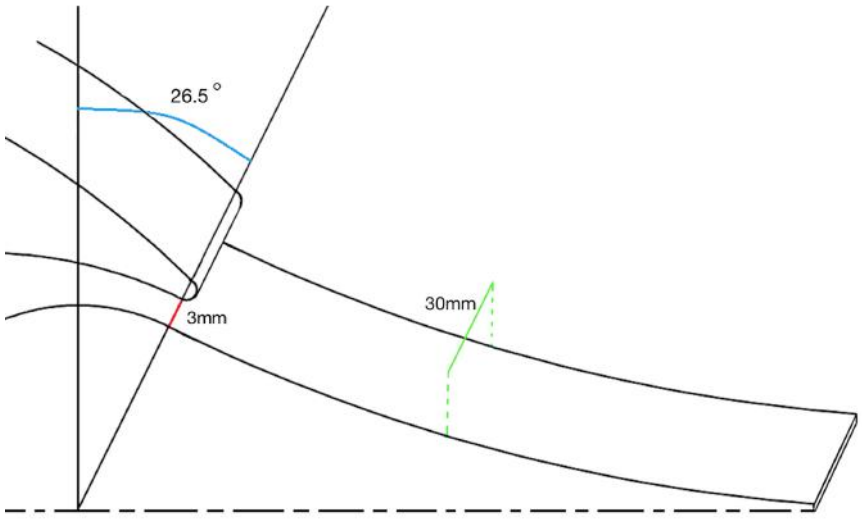

Figure 1.5: Final geometry main characteristics.

Chapter 2

Simulations

In order to validate the geometry established during the pre-design analysis it was decided to simulate the flow in two dimensions using the free OpenFOAM software. This software allows to solve turbulent compressible flow equations using the finite element method. This chapter will cover the numerical model used, the reasons it was chosen and the implications of that choice before presenting the validation methods used to check the model and the mesh and finally disclosing the results obtained.

2.1 Numerical model

2.1.1 Categorization of the flow

First it is necessary to establish the kind of flow to be simulated. In order to do that, the Reynolds number of the flow must be computed using the perfect gas law and the definition of the Mach number:

$$Re = \frac{\rho u L}{\mu} = \frac{p}{RT}(c \cdot M)\frac{L}{\mu} = \frac{p}{RT}(\sqrt{\gamma RT} \cdot M)\frac{L}{\mu} = p\sqrt{\frac{\gamma}{RT}}M\frac{L}{\mu} \tag{2.1}$$

Many parameters found in this expression vary across the flow. Since only a simple approximation for upper and lower limits of the Reynolds number is required, extreme values can be used for the parameters of this equation. Using the throat height $h = 3\,mm$ as representative length and thus computing the Reynolds number around the throat where $M \simeq 1$, these boundaries ca, be computed:

$$1.5 \cdot 10^5 \leq Re \leq 8.3 \cdot 10^5$$

These values put the studied flow in the compressible turbulent flow category, whose simulations require a number of choices to be made regarding the simulation models to use.

2.1.2 Turbulence model

To parametrize the simulation a turbulence model must be chosen. It was decided to use the RANS equations (*Reynolds-Averaged Navier-Stokes*) because it is light in computing requirements, relatively easy to use, and has been proven to be effective. These equations come from splitting the NAVIER-STOKES equations into a mean and a turbulent time-varying value and considering the time-varying part as an additional (turbulent) stress, also called *Reynolds stress*. The good modelling of those stresses remains a research area in the domain of Computational Fluid Dynamics (or CFD) and various possibilities exist.

Nowadays, two equations models are one of the most common type of turbulence models for CFD. By definition, these models include two additional transport equations to represent the turbulent properties of the flow allowing them to take into account turbulent energy convection and diffusion. One of the transported variables is almost always the turbulent kinetic energy $k = \frac{\overline{u_i' u_i'}}{2}$, which represents the intensity of the turbulence.

The second transported variable varies from one model to another, with the most used ones being:

- **The $k - \epsilon$ models** introduce the turbulent dissipation ϵ which determines the rate of dissipation of turbulent kinetic energy. This model is robust and has been used with good results for free shear-layer flows with relatively small pressure gradients. Similarly, the model gives good results for wall-bounded flows only if mean pressure gradients are small. This could be problematic in the case studied in this paper since both a free shear-layer and wall-bounded flow with relatively high pressure gradients need to be simulated.

  Furthermore, due to the hypotheses underlying this model, which include a high Reynolds number, it doesn't solve entirely the boundary layer equations where the Reynolds number is low, but rather uses a wall-law to predict the behaviour of the turbulent flow near a wall without solving the equations. This lightens the computing requirements of the model but is a source of imprecisions and thus another reason to dismiss the use of this model.

- **The $k-\omega$ models** introduces the specific dissipation $\omega = \epsilon/k$ which is similar to the variable ϵ. No hypothesis of high Reynolds number is made during

the derivation of the equations of the model, meaning that the boundary layer can be entirely simulated. This, however, requires a boundary layer mesh extremely thin in the near-wall region and thus more computing resources.

This model gives good results in the near-wall region, it tends however to be too sensitive to the inlet free-stream turbulence properties making its results sometimes unreliable in free-stream conditions.

- **The SST $k-\omega$ model**, for *Shear-Stress-Transport* model, tries to combine the best of two worlds by using the $k-\omega$ model in the boundary layer and the $k-\epsilon$ model in free-stream conditions. Since the whole boundary layer is to be simulated, a refined mesh is needed in the near-wall region.

  This model also limits the shear stress under certain conditions, this stress being overestimated by the two precedent models.

  Since this model gives the best results of the three it was the one used for the simulations disclosed in this chapter.

2.2 Parametrization

2.2.1 Mesh

When doing computational fluid dynamics, the next step after choosing the equation model is to generate a mesh adapted at the same time to the problem to be solved and to the chosen model. As said previously, the SST $k-\omega$ model chosen requires a complete resolution of the boundary layer flow equations and thus a mesh adapted to the near-wall region. This imposes a condition on the size of the first cell at the wall in order to be inside the laminar sub-layer region of the flow.

To estimate the size of that laminar sub-layer it is needed to go back to the basics of turbulent flow theory. The equation describing the velocity of a fluid in a two dimensional canal of height $2h$ as a function of the distance to the wall y is:

$$(\nu + \nu_t)\frac{d\bar{u}}{dy} = \bar{u}_\tau^2(1 - \frac{y}{h}) \tag{2.2}$$

with:

- $\nu_t = \frac{-\overline{u'v'}}{\frac{d\bar{u}}{dy}}$ the effective turbulent velocity.
- $\bar{u}_\tau = \sqrt{\frac{\bar{\tau}_w}{\rho}}$ the shear velocity.

Since only the near-wall region is considered it means that $y \ll h$ and thus $\frac{y}{h} \ll 1$, implying that the right hand side can be simplified as just $\bar{u}_\tau^2$. Furthermore, only the laminar sub-layer of the flow is of importance here, meaning that mathematically speaking $\nu_t \ll \nu$ and the left hand side of the equation can be simplified as $\nu \frac{d\bar{u}}{dy}$, allowing to rewrite the equation:

$$\nu \frac{d\bar{u}}{dy} = \bar{u}_\tau^2 \tag{2.3}$$

This relationship can now be rewritten in so called *internal coordinates* defined as:

- $\bar{u}^+ = \frac{\bar{u}}{\bar{u}_\tau}$.
- $y^+ = \frac{y\bar{u}_\tau}{\nu}$.

The differential equation then becomes as simple as it could get:

$$\frac{d\bar{u}^+}{dy^+} = 1 \tag{2.4}$$

and its solution is simply $\bar{u}^+ = y^+$. Experimental results show that this linear relationship is valid up to $y^+ \simeq 5$ and this is the condition that to be imposed on the size of the first cell at the wall: $y^+ < 5$. To translate this dimensionless condition y^+ into a size condition y it is necessary to go through various transformation steps:

1. The definition of the variable $y^+ = \frac{y\bar{u}_\tau}{\nu}\,[-] \quad \Rightarrow \quad y = \frac{y^+\nu}{\bar{u}_\tau} = \frac{y^+\mu}{\bar{u}_\tau \rho}\,[m]$

2. The definition of the shear velocity $\bar{u}_\tau = \sqrt{\bar{\tau}_w/\rho}\,[m]$ is then injected in the previous relationship to give:

$$y = \frac{y^+\mu}{\rho\sqrt{\bar{\tau}_w/\rho}} = \frac{y^+\mu}{\sqrt{\bar{\tau}_w \rho}}\,[m]$$

3. The definition of the shear stress at the wall $\bar{\tau}_w = \frac{1}{2} C_f \rho U^2\,[N/m^2]$ is also injected to get:

$$y = \frac{y^+\mu}{\sqrt{\frac{1}{2}C_f \rho^2 U^2}} = \frac{y^+\mu}{\rho U\sqrt{\frac{1}{2}C_f}} = \frac{\mu}{\rho U}\frac{y^+}{\sqrt{\frac{1}{2}C_f}}\,[m]$$

4. An empirical correlation is used in order to link the friction coefficient C_f to the Reynolds number in an smooth canal: $C_f = 0.059 \cdot Re^{-0.2}$ $[-]$. It gives:

$$y = \frac{\mu}{\rho U} \cdot \frac{y^+}{\sqrt{\frac{1}{2}0.059 \cdot Re^{-0.2}}} = \frac{\mu}{\rho U} \cdot \frac{y^+}{\sqrt{\frac{1}{2}0.059}} Re^{0.1} = \frac{\mu}{\rho U} \cdot 5.8 \cdot y^+ \cdot Re^{0.1} \; [m]$$

5. Finally the use of the definition of the Reynolds number $Re = \rho U L/\mu$ yields:

$$y = \frac{L}{Re} \cdot 5.8 \cdot y^+ \cdot Re^{0.1} = 5.8 \cdot y^+ \cdot L \cdot Re^{-0.9} \; [m] \tag{2.5}$$

Using the Reynolds number values computed earlier and the throat height of $3\,[mm]$ the last independent variable is y^+ which has to be $y^+ \leq 5$. In order to have some margin a value of $y^+ = 1$ was chosen, finally allowing the computing of the size of the first mesh cell: $y \simeq 4 \cdot 10^{-7}$ $[m]$. Since such a refined mesh over the whole domain could not be afforded for computing resources reasons, several mesh generating functions provided by OpenFOAM were used to stretch the cells in the direction perpendicular to the wall. Finally, since the problem is symmetric, only half the flow was meshed and simulated with a symmetry plane condition imposed on one side of the domain.

The mesh on which most of the simulations have been made has a ratio of $0.003 = 0.3\,[\%]$ between the width of the first cell at the wall and the innermost cell with a constant stretching. The complete mesh has a total of 54 400 elements and 110 162 points. This mesh has been modified later on to check the mesh convergence of the simulation, which means that the solution obtained has to be independent of the mesh used as long as it satisfies the model's conditions.

The mesh used for the simulations and its refining at the throat and near the walls is shown on figure 2.1.

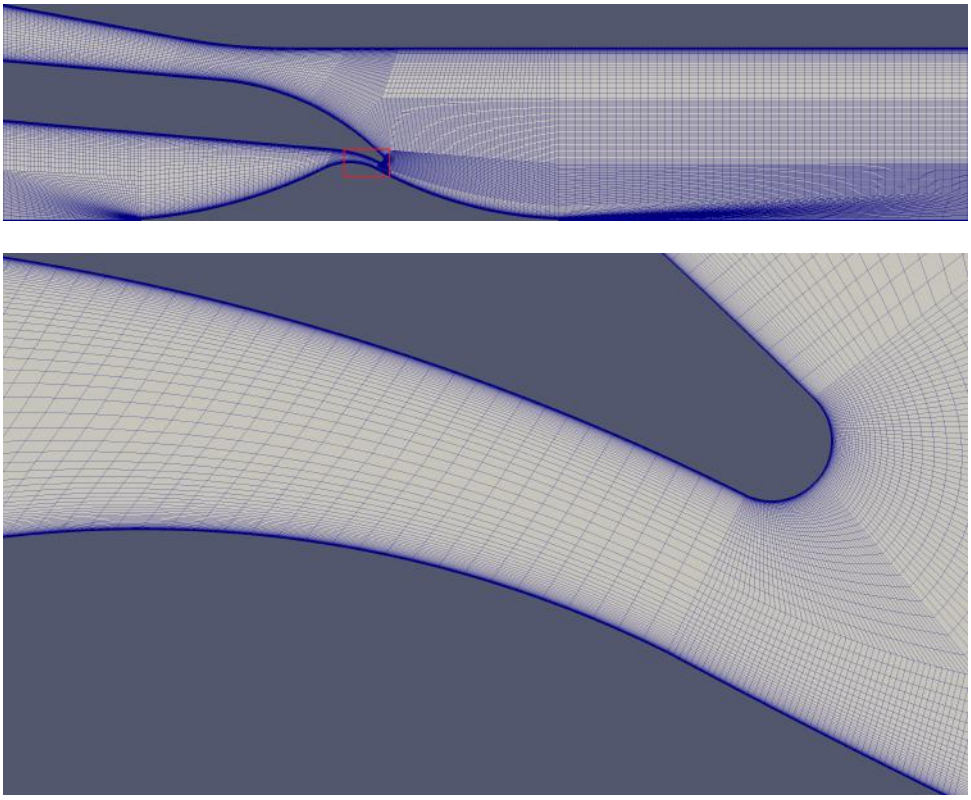

Figure 2.1: Simulation mesh with zoom on the throat.

2.2.2 Boundary conditions

Once the mesh has been generated, the last step of the parametrization is to impose boundary conditions corresponding to the flow that will be studied. In this study, three types of boundary conditions have been used. They are shown in figure 2.2 and are:

- A **symmetry plane** on the bottom side of the mesh so that only half the flow has to be simulated. It is shown in RED on figure 2.2.
- Three **Inlet-Outlet** conditions are imposed. These conditions allow a flow in both directions through the boundary depending on the thermodynamic variables imposed on the flow. They are shown in GREEN on figure 2.2. The different types of imposed conditions are:

  - At the **primary inlet** (bottom left of the figure),connected to the compressor, a condition of stagnation pressure p_0 is imposed. The value given to p_0 can be controlled through the compressor's outlet valve.
  - The **secondary inlet** (top left of the figure) is connected to the atmosphere through standard valves making it possible to affect the driven secondary flow.
  - At the **outlet** (right of the figure) a stagnation pressure equal to the atmospheric pressure is imposed if the the flow of air is negative (recirculation coming from outside), if the flow of air is positive the flow pressure is simply extrapolated from inside the domain.

- The **wall conditions** are *null velocity* (often referred to as *no slip* condition) and *no heat transfer*. The walls are considered to be hydraulically smooth. These boundaries are not shown in a specific color but can be noticed through the refining of the mesh near the walls.

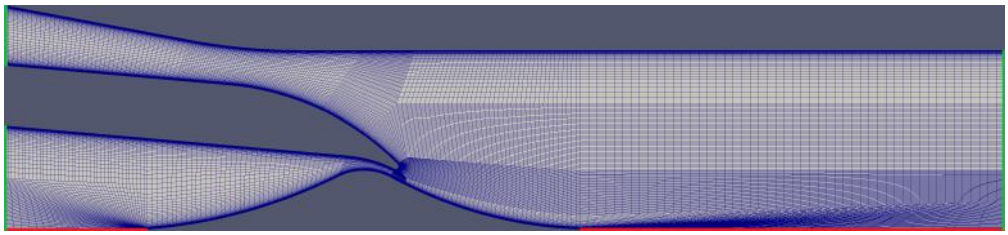

Figure 2.2: Simulation mesh with different boundaries.

2.3 Validations

Before using the chosen model and the generated mesh to perform a numerical analysis of the nozzle to be designed it is important to validate them. In order to do that, the model and the mesh were used to simulate a test case slightly more complex than the simulations that will be computed for the nozzle analysis. This demonstration case was set by imposing a stagnation pressure p_0 of $4\,bar$ on an initially at rest air inside the convergent. The simulation was then run over enough time steps in order to converge before performing the checks discussed further in this section.

First it is important to check whether or not the simulation shows a **convergence towards a steady state flow**. In a steady state solver the basic test to perform is to check for a decrease in the residuals. Since the solver used is not a steady state solver, this test doesn't apply here. Instead, convergence can be verified by checking if various computed values converge towards a steady state value. The choice of those values being arbitrary, the convergence of the mass within the simulation domain was chosen. This allows to perform another validation which is the **conservation of mass** over the simulation domain. This is done by integrating the mass over the whole domain and verifying that the computed values converges. This process is shown on figure 2.3. The great variations observed are due to the fact that the flow studied here is compressible, meaning that changes in the density of the air inside the domain, for example around a compression shock, could lead to some mass of air being "stored" in the flow over a small period of time.

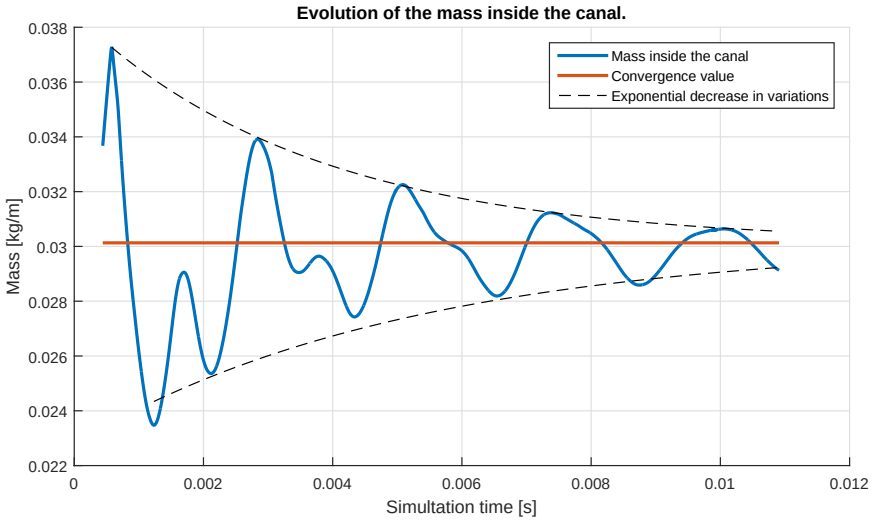

Figure 2.3: Evolution of the mass within the simulation domain.

When simulating a flow it is important to verify that the mesh generated has no influence on the computed solution other that of augmenting accuracy with the refining of the mesh. This process is known as **mesh convergence**. To achieve this, the converged solution is mapped towards new meshes with different number of elements before computing a few iterations on the new mesh in order to get the solution to converge on those meshes. Various results computed are then compared between meshes to check whether the computed solution is dependent from the mesh. As a comparison method the Mach number distribution over the symmetry

plane has been used, as represented on figure 2.4.

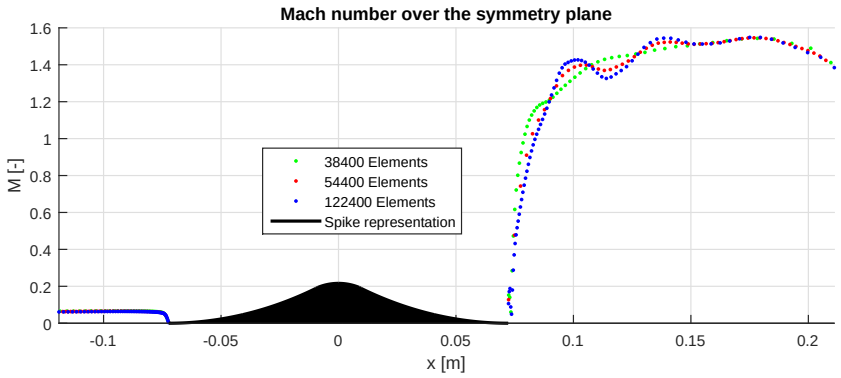

Figure 2.4: Mach number distribution over the symmetry plane for various refinement of the mesh.

It can be seen that the mesh with 38400 elements is less precise than the two other meshes, whereas the difference between the meshes of 54400 and 122400 elements is relatively small even if the number of elements was doubled. That is because the precision gained with the refinement of the mesh is not linear but decreases exponentially. This means that the number of elements has to rise exponentially for the precision to rise steadily.

To make sure that the mesh is refined enough, the root-mean-square error is computed between the most refined mesh and the other two meshes using the next formulae.

$$\sum_{i=1}^{n} \sqrt{\frac{(M_{i,\text{ refined}} - M_{i,\text{ unrefined}})^2}{n}} \tag{2.6}$$

The computed errors are 4.1% and 9.5% for the mesh of 54400 and 38400 elements respectively. The error being bellow the 5% margin for the initial mesh it can be concluded that the mesh is refined enough for the scope of this study.

2.4 Simulation results

Since all the results obtained with the OpenFOAM simulation software cannot be disclosed here, only a few relevant cases will be analysed.

One of the primary uses of aerospike nozzles being in the aerospace propulsion domain, due to the altitude compensation effect, The results are disclosed following an "ascent profile" of sort: the successive flow regimes considered would correspond to an altitude variation during the launch of a rocket. The expansion of the flow depends on the ratio $\frac{p_0}{p_a}$. Since the altitude cannot be altered, and thus the atmospheric pressure p_a remains unchanged, it was replaced by a change in stagnation pressure p_0.

Extremely over-expanded flow

On the ground, the ratio $\frac{p_0}{p_a}$ is low. For the purpose of this study, this is achieved by setting the stagnation pressure p_0 to a relatively small value. A value of $p_0 = 2\ [bar]$ was chosen.

The flow is extremely over expanded, meaning the final pressure of the supersonic flow is much lower than the ambient pressure. The plume of supersonic air is thus compressed against the spike. The expansion fan at the throat is relatively small and reflected between the spike and the shear layer.

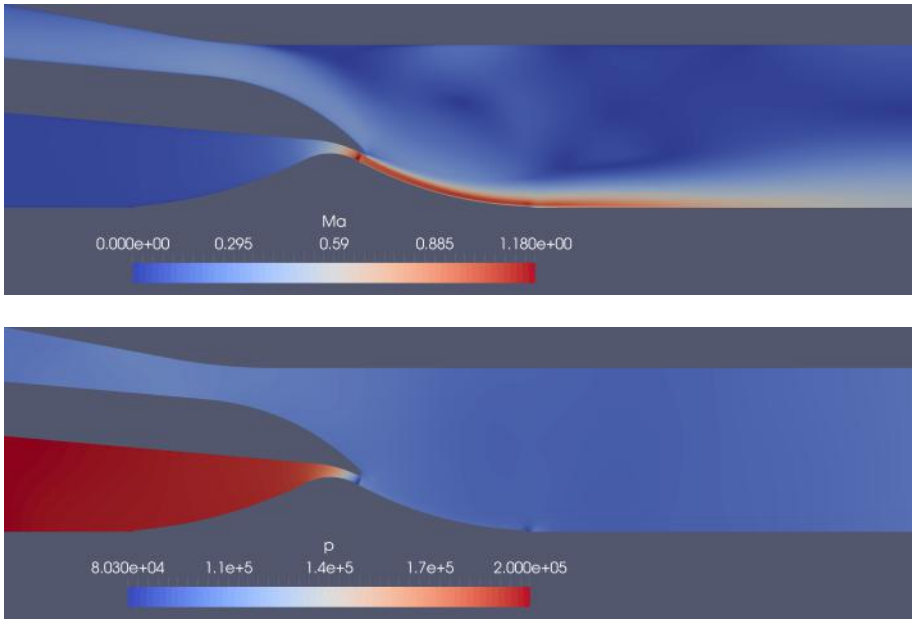

Figure 2.5: Simulations with $p_0 = 2\ [bar]$, Mach number and pressure.

Over-expanded flow

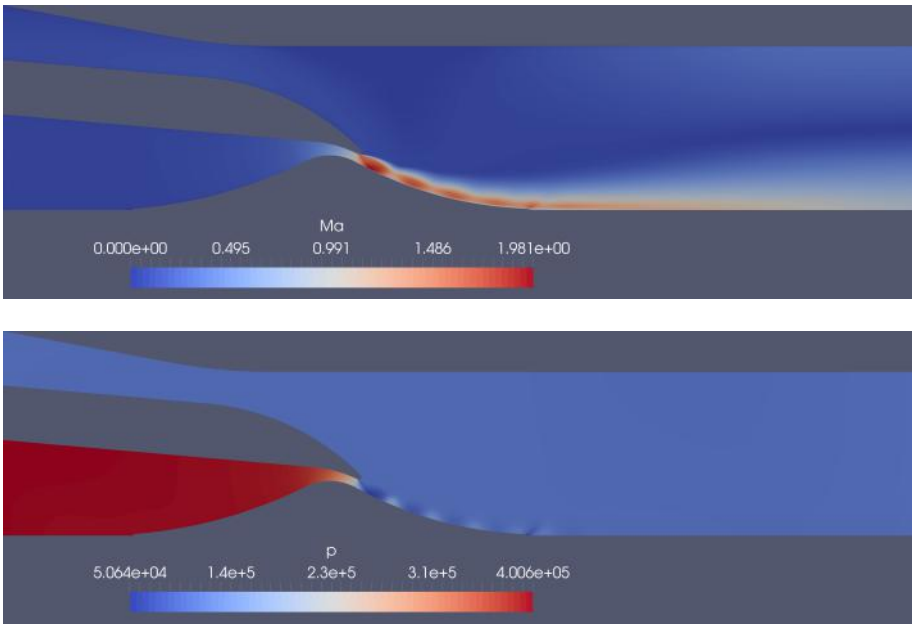

Figure 2.6: Simulations with $p_0 = 4\,[bar]$, Mach number and pressure.

As the vehicle rises through the atmosphere, the ratio $\frac{p_0}{p_a}$ increases. The case disclosed here corresponds to $p_0 = 4\,[bar]$. The flow is still over-expanded but the effects of altitude compensation start to be observable. The expansion fan at the throat diverts the supersonic flow of air so that it acquires more horizontal momentum. This expansion fan is reflected between the spike and the shear layer.

Optimally expanded flow

At a certain altitude, or stagnation pressure in this study, the ratio $\frac{p_0}{p_a}$ reaches a value for which the nozzle was designed and its expansion is optimal. The nozzle analysed here was designed for an optimum expansion when $p_0 = 7.8\,[bar]$ and $p_a = 1\,[bar]$ meaning that the initial direction of the shear layer after leaving the throat is purely horizontal.

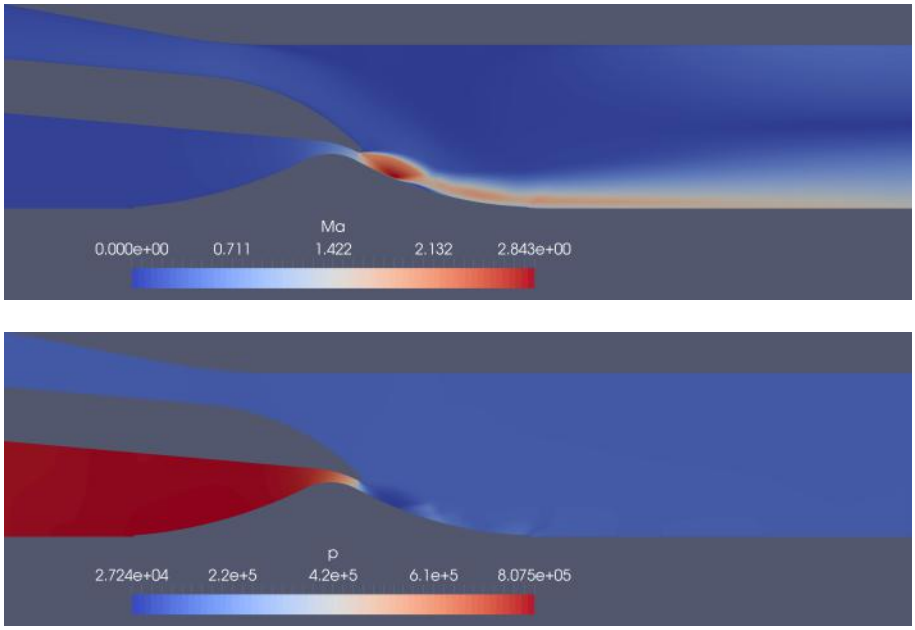

Figure 2.7: Simulations with $p_0 = 8\ [bar]$, Mach number and pressure.

It can be observed on figure 2.7 that the boundary layer does not adhere to the spike all the way through its expansion. This is due to the size of the spike. The supersonic flow expands extremely fast when it exits the throat augmenting its cross section. The spike however couldn't end right with the expansion fan for design reasons. The supersonic flow having acquired horizontal velocity through the expansion fan is then driven on by its momentum and partially detaches from the spike. Ideally, the spike should end where the boundary layer separates from the spike, but that would have given an extremely thin spike which could not be fixed properly to the nozzle.

Under-expanded flow

Once the vehicle passes the point corresponding to the optimal $\frac{p_0}{p_a}$ ratio and continues to rise, the flow becomes under-expanded. This means that the ambient pressure is so low compared to the stagnation pressure of the fluid that the supersonic plume expands outward from the spike. This gives the fluid momentum in an non horizontal direction and thus doesn't generate thrust. It is, so to say, a waste of the energy contained in the flow.

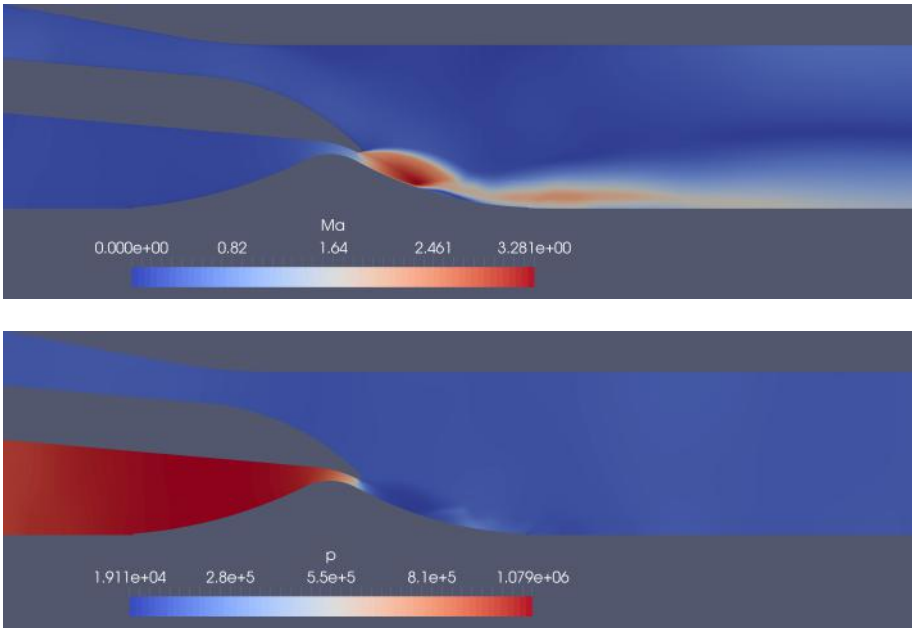

Figure 2.8: Simulations with $p_0 = 10\ [bar]$, Mach number and pressure.

Chapter 3

Design

3.1 Test bench description

The test bench consists of four parts. An air intake system (1) connected to a compressor, the aerospike nozzle (2), a visualization system (3), and a user interface (4). All these parts will be presented in the following pages, but the objective of this thesis being the design of the aerospike nozzle, it is this design, and its manufacture and assembly aspects that will mostly be discussed. All the blueprints of the design are presented in appendix A.

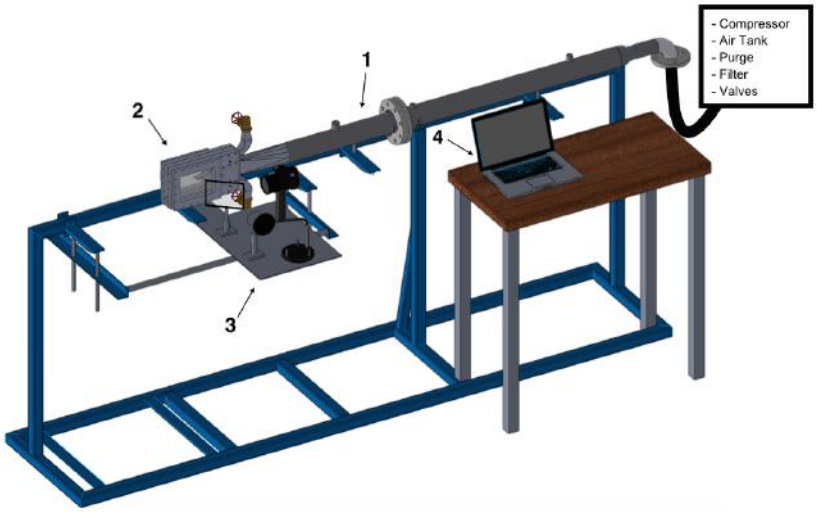

Figure 3.1: 3D representation of the complete test bench.

3.1.1 Air intake system

The air intake system consists of different elements providing clean air at a constant pressure (imposed by the user) to the nozzle connected at the end of the device.

Figure 3.2: Compressor [19].

Figure 3.3: Air tank [19].

The volumetric compressor is a three stages compressor, from the company AF COMPRESSORS, and can provide a flow rate of 1200 m^3_N/h at a maximal pressure of 40 bar. The compressor directly fills an air tank of a capacity of 2000 L. Although this tank is designed to held a maximal pressure of 42 bar, a security valve is installed to limit this pressure to 16 bar.

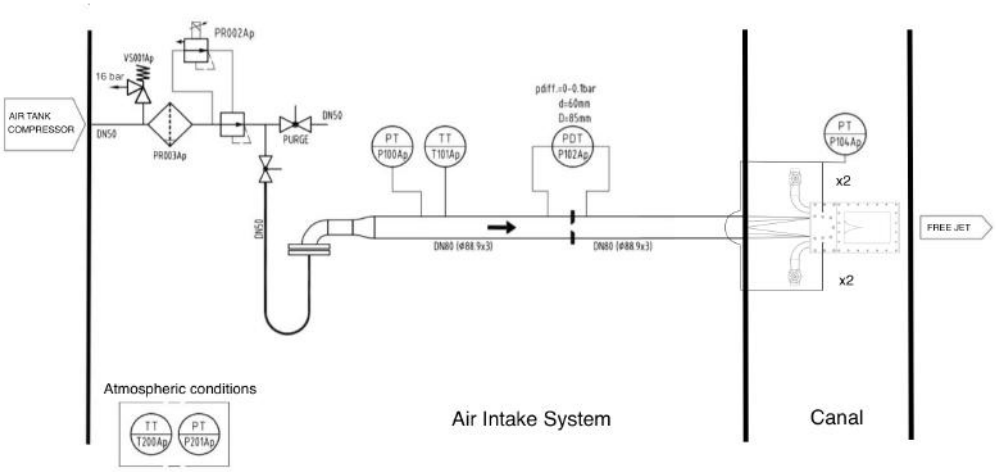

Figure 3.4: P&ID of the test bench.

As it can be seen on figure 3.4, which represents the piping & instrumentation diagram that describes the test bench, after the tank and a second security valve (set to 6 bar)comes a filter (PR003Ap). This filter is trapping particles larger than 40 μm. It is followed by a regulation valve that controls the test bench pressure with a PID controller (proportional-integral-derivative controller) connected to the pressure sensor P100Ap and an electro-valve PR002Ap. This pressure is imposed by the user via the computer and the user interface. After the regulation valve, a purge is installed to evacuate potential impurities that could be present in the air tank and damage the device.

The pressure and temperature sensors P100Ap and T101Ap are used to measure the characteristics of the air injected into the nozzle, while the sensor P104Ap reports the different pressures in the nozzle during the flow expansion. A differential pressure flow-meter is set up half way of the stabilisation pipe and is connected to the pressure sensor P102Ap, the principle of such a device is illustrated in figure 3.5.

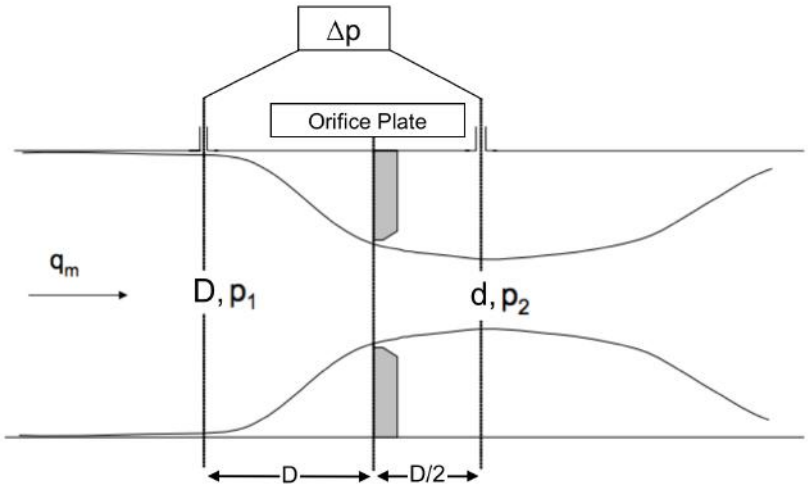

Figure 3.5: Differential pressure flow-meter.

In order to calculate the flow rate through the nozzle an orifice plate is placed across the stabilisation pipe and pressure is measured on each side of this diaphragm. These two pressures are connected to the P102Ap sensor in order to get the differential pressure Δp. By following the international standard ISO-5167-2000 [6], the flow rate can thus be calculated thanks to the following formula [23]:

$$Q_m = \frac{C}{\sqrt{1-(d/D)^4}} e \frac{\pi}{4} d^2 \sqrt{2\Delta p \rho_1} \tag{3.1}$$

Where C is the discharge coefficient, ρ_1 is the volumetric mass density of the fluid at the first pressure sensor, and ϵ is called expansion factor and is the coefficient used to take into account the compressibility of the fluid.

3.1.2 Visualization by Shadowgraph

The shadowgraph is a simple optical method used to reveal density inhomogeneities in transparent media. This method relies on a simple principle : a light source projects light rays towards a transparent media, and as the refraction of light rays is altered by the media's density a pattern of refraction can be observed on a recording plane [17]. In this case, the transparent media is air which density is altered by the different compressible flow phenomena.

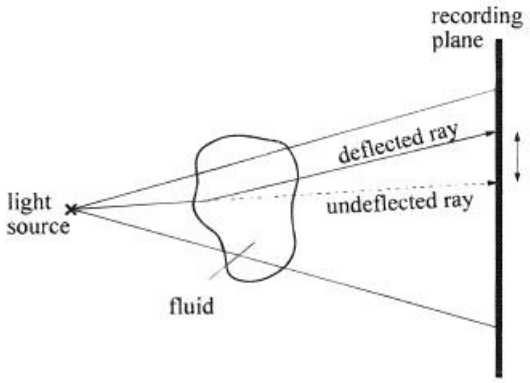

Figure 3.6: Shadowgraph principle [11].

The areas of high and low density within the flow refractively deflect light rays in different ways resulting in brighter and darker spots on the recording plane. A visible pattern of density variation is thus produced permitting qualitative observations of the phenomena occurring in the flow.

For this experiment this device will allow to observe expansion waves, shear layers and compression shocks since these phenomena alter locally the air density and thus distort the light rays.

On a practical point of view, the installed device is composed of a light point source, a parabolic mirror, a filter and a camera. It has been set up last year by Kevin Gevers and Thibaut Libbrecht for their master thesis : "Conception et réalisation d'un banc d'essai pour la mesure et la visualisation d'écoulements supersoniques en canal"[19]. However, in order for the device to fit the aerospike nozzle, it had to be adjusted.

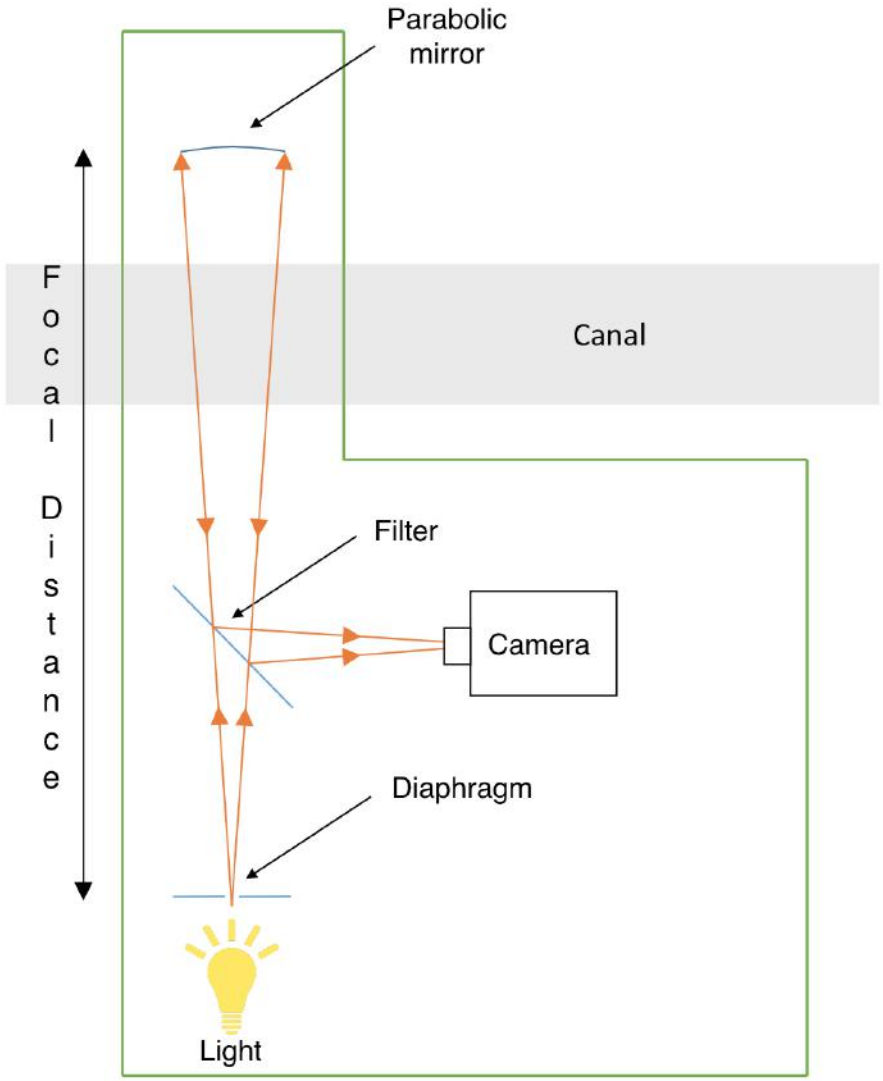

Figure 3.7: Layout of the shadowgraph installation.

First the light point source is created using a diaphragm placed before a light source. This prevent the final image from being too diffuse. The light emitted then

travels through a filter towards the nozzle. The filter is inclined by 45° regarding to the light-mirror alignment and allows 50% of the light to pass. The objective of this filter is at the end to deviate the reflected rays towards the camera.

Once it has reached the nozzle the light passes through the air flow (thanks to the portholes) where its path is altered by the flow density, and reaches the parabolic mirror on the other side.

The parabolic mirror will reflect the light rays towards its focal point, also called focus of the parabola. Hence if the device is correctly set up, that is if the focal point coincides with the source point, then the reflected rays will follow the exact same path as the incident rays, and will be partly deviated by the filter towards the camera. This will re-converge the light rays and allow to observe the density gradients of the flow without being aligned with the light and nozzle.

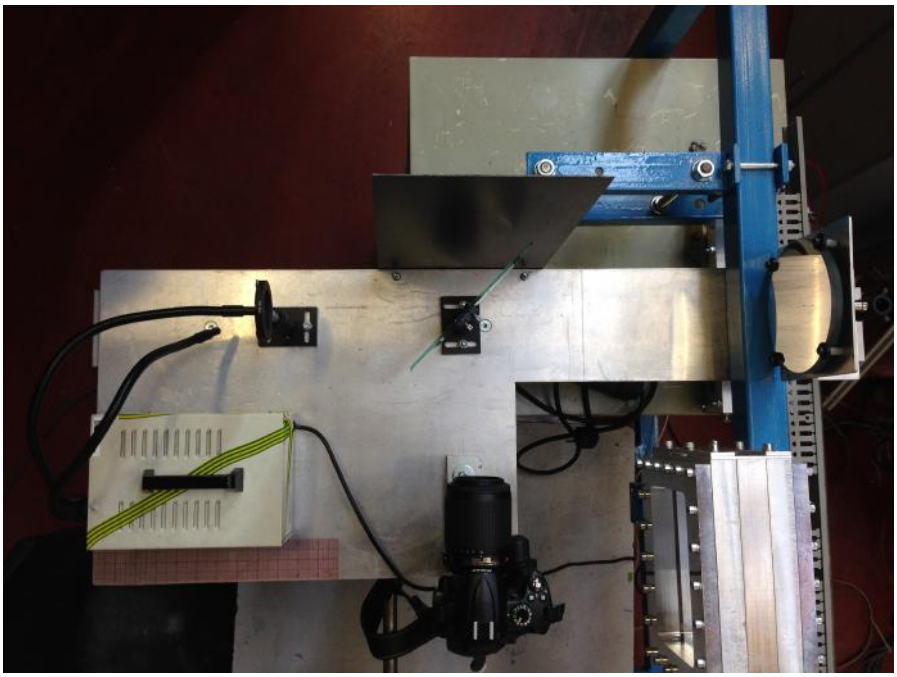

Figure 3.8: The shadowgraph installation.

If the device isn't correctly set up the light rays will undergo two refractions, resulting in a false final visualization.

This visualization system is placed on a mobile frame which is part of the test bench. This mobile frame can be shifted along the flow axis (the horizontal direction) in order to observe the flow phenomena along the canal.

The obtained image reveals darker areas where the fluid is denser and lighter areas where the fluid has lower density. For instance, the figure 3.9 represents a picture captured looking at a burning match with the shadowgraph installation.

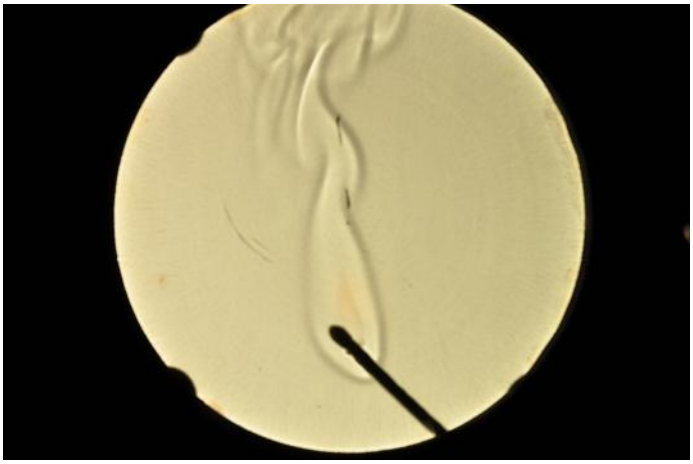

Figure 3.9: Observation of a burning match through the shadowgraph.

3.1.3 User interface

The user interface developed for the aerospike nozzles is represented on the figure 3.10. This user interfaced is used to set the test bench pressure, and display and record the values measured by the different sensors.

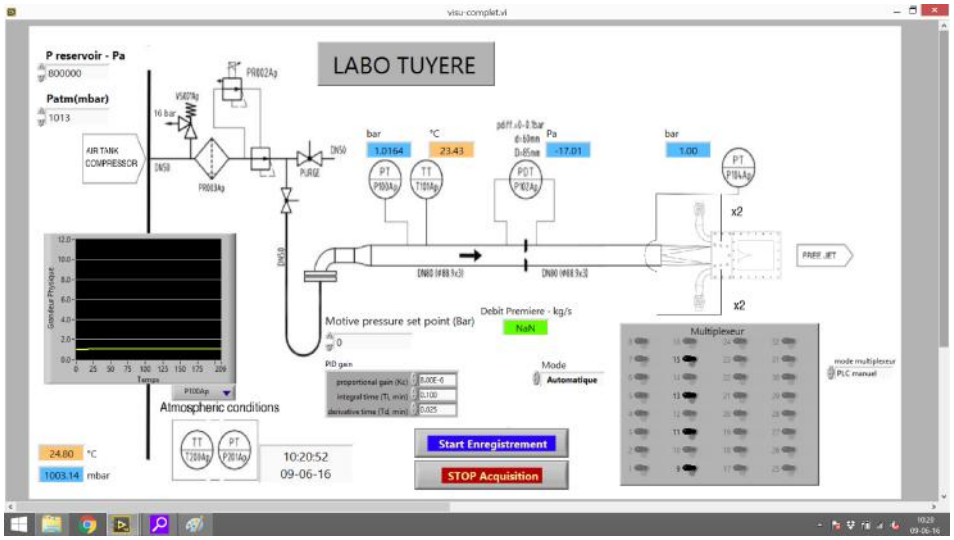

Figure 3.10: Test bench user interface.

The graph on the left of the interface displays, regarding to the elapsed time, the value measured by the sensors currently selected in the rolling menu.
The multiplexer is represented on the right of the user interface and allows the user to activate the record one of the four pressure. Two modes are available on the multiplexer : PLC manual and PLC sequence. In the first case the user can manually choose the pressure sensor from which the value has to be recorded. In the second option the system automatically switches from one pressure sensor to another at the end of a time interval set by the user. In order to get correct values it is advised not to set a time interval smaller than 12 seconds.

The user interface was realized with the Lab View software (V14.0.1) and is a modified version of the user interface from Kevin Gevers and Thibaut Libbrecht [19].

3.2 Design and assembly

The final design of the aerospike nozzle is presented on figure 3.11.

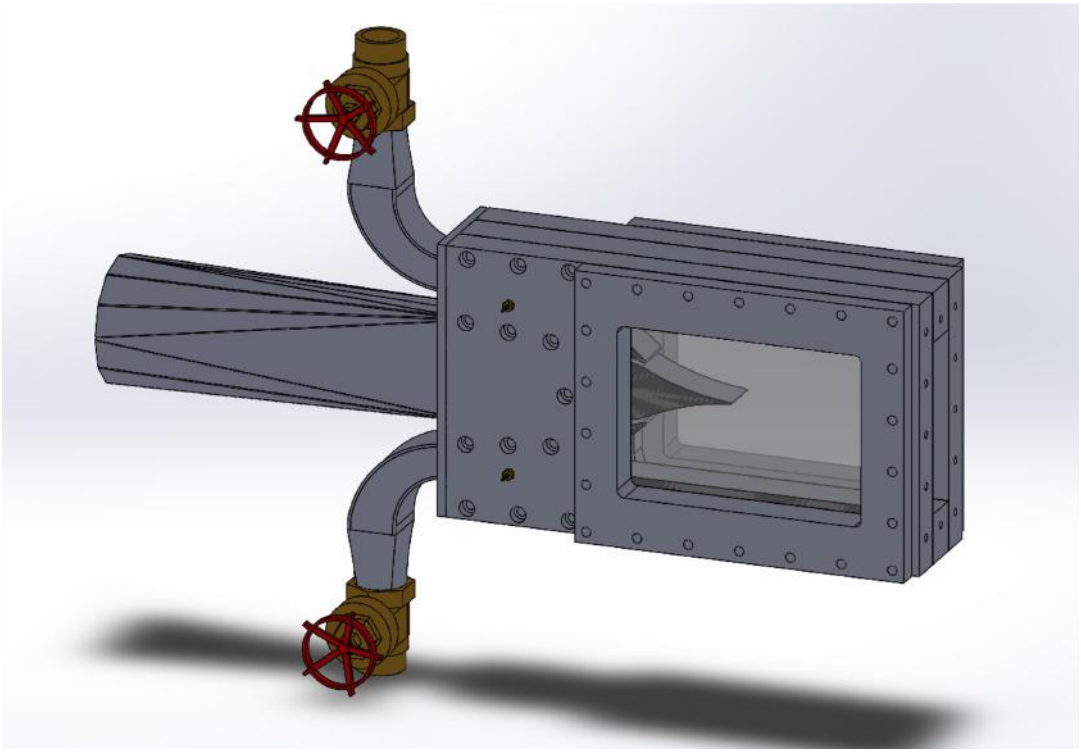

Figure 3.11: Final design of the aerospike nozzle.

As represented on figure 3.12, the designed nozzle consists of three main parts:

- The transition piece (1) between the air intake system and the entry of the primary flow of the nozzle.
- The aerospike nozzle (2), in which the fluid expansion occurs.
- The two chimneys (3) regulating the secondary flows in the nozzle.

All these parts are connected together thanks to the green piece on the figure 3.12. This back-piece is screwed on the nozzle on one side and welded to the transition piece and the chimneys on the other side.

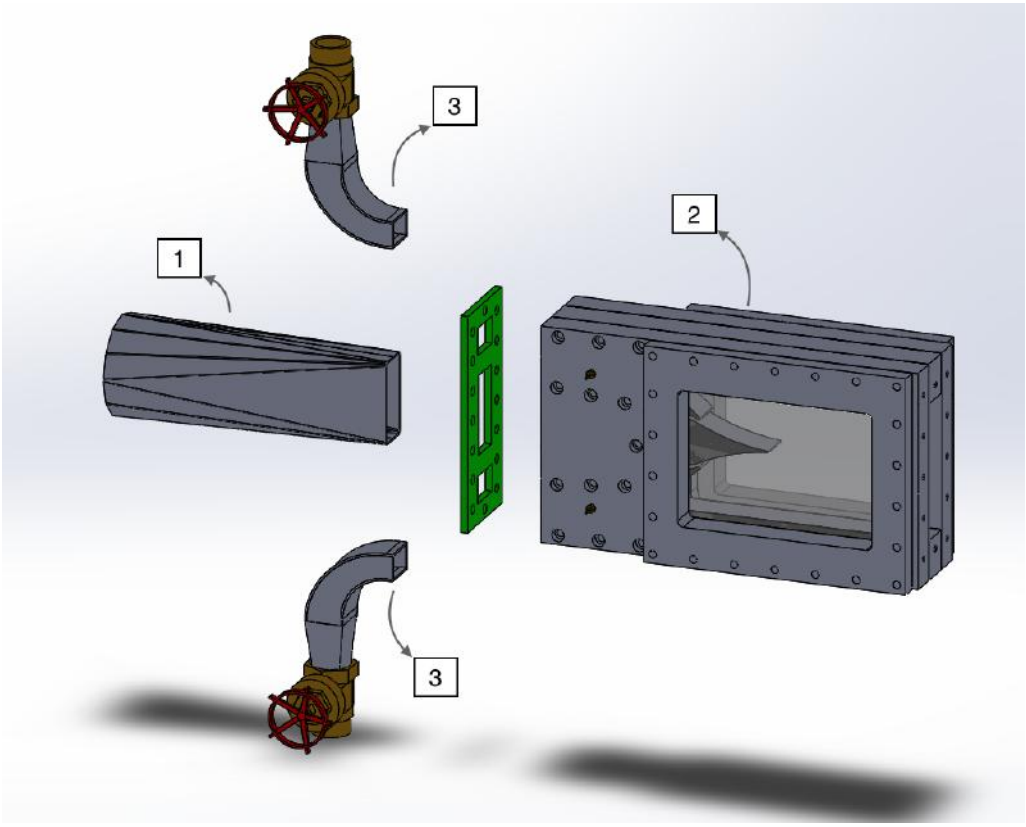

Figure 3.12: Split view of the three main parts of the nozzle and the connection back-piece.

3.2.1 Transition piece

A transition piece had to be installed in order to link the nozzle to the air intake system. Indeed the end of the air intake system is a pipe (coming from the compressor) with a diameter of $D = 88.9\,mm$, whereas the entry of the primary flow canal have a rectangular shape with the following dimensions : $h = 70\,mm$ and $w = 30\,mm$.

Figure 3.13: Inlet of the nozzle.

Figure 3.14: Outlet of the compressor pipe.

This piece consists of two parts, each made of a 1.5 mm thick aluminium plate, cut to the right shape and bent in order to obtain a circular section on one side and a rectangular one on the other.

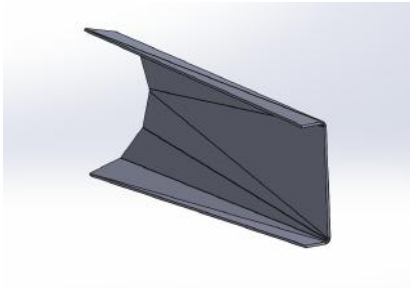

(a) Half of the transition piece.

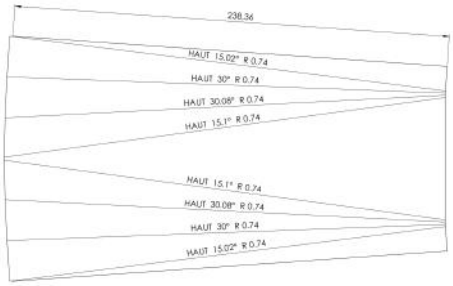

(b) Unfolded drawing of one of the two part.

Figure 3.15: Transition piece.

To avoid the fluid to have a too large vertical velocity at the entry of the nozzle the slope of the transition was limited to a maximal value of 7°.

3.2.2 Nozzle

The nozzle is the heart of the design. It consists of a central flow canal surrounded by different frame pieces to create a box. This assembly is mostly made of aluminium and PMMA (also known as Plexiglas) pieces. A split view is presented in the figure 3.16. This view only presents the pieces composing the nozzle as well as the back piece that links the nozzle to the other parts of the device.

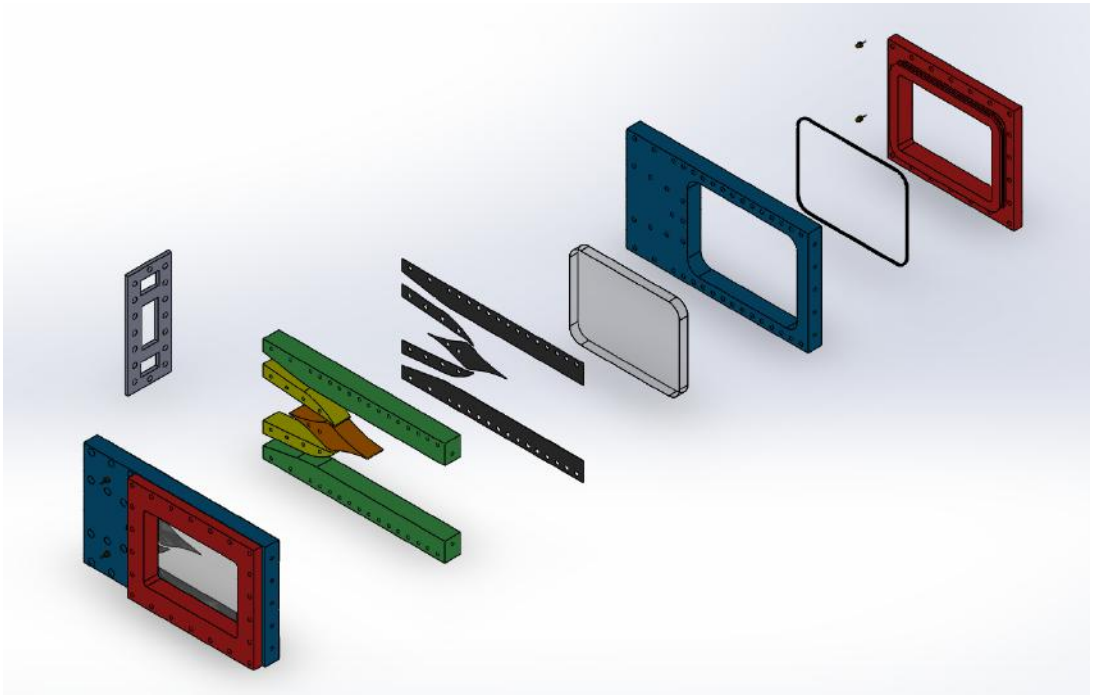

Figure 3.16: Split view of the nozzle.

The canal

The canal defines the flow and is composed of five pieces : the spike (in orange), the two spike borders (in yellow) and the canal borders (the green pieces). The spike borders delimit the primary air flow and direct it to ensure that the flow angle is 26.5° as decided in the pre-design chapter. The primary flow will later be split by the spike and will expand and accelerate. This acceleration will result in shear layers dragging static air and creating secondary driven flows in the two

end canals. These secondary flow canals are each delimited by the spike and canal borders.

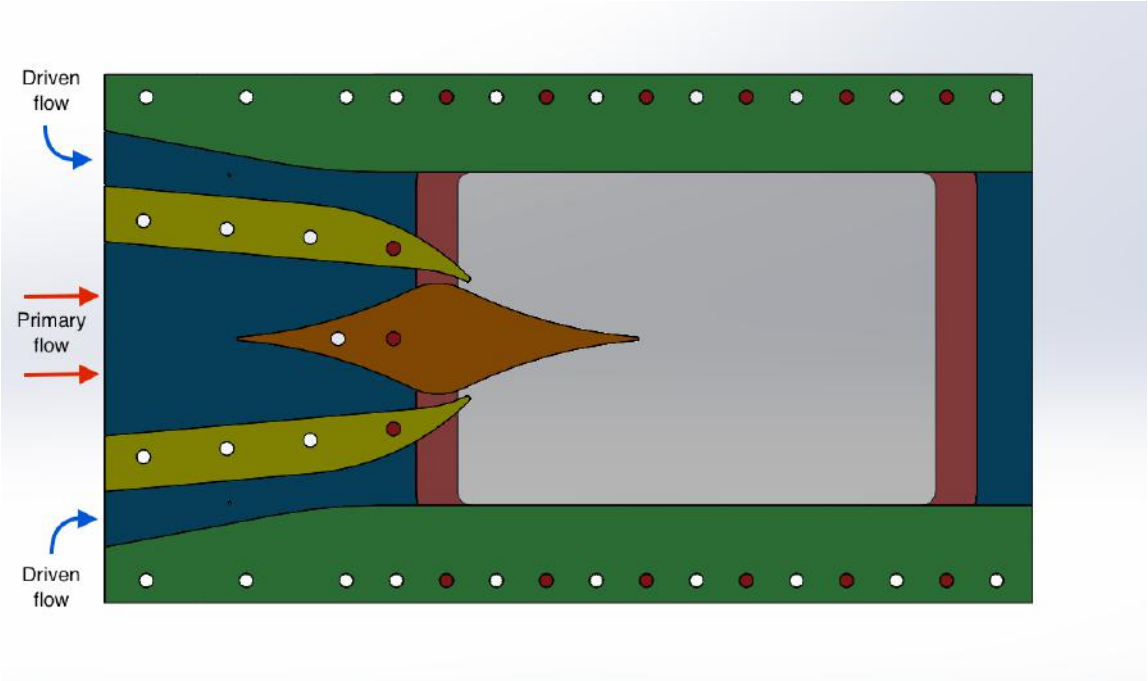

Figure 3.17: The canal.

The canal geometry has been designed in order to ensure a 3 mm throat with a 26.5° angle flow direction. Moreover the objective was to keep the design as simple as possible, by using only circular and linear shapes, mainly to reduce machining costs.

For the assembly, sealing joints are placed on each side of the canal pieces to avoid any leaks of the flow.

The PMMA portholes

The transparent PMMA portholes allow the observation of the fluid expansion within the nozzle.

In order to observe the fluid expansion within the nozzle, transparent portholes need to be installed. For this part, three different materials commonly used in optics were considered : PMMA, fused quartz, and crown glass (N-BK7). Their characteristics are presented in table 3.1.

Material	V [-] [1]	n [-] [2]	$\sigma_{el}[MPa]$	Price [€]
Fused quartz	67.56 [9]	1.4584 [9]	48 [9]	672 [19]
Crown glass (BK7)	64.17 [8]	1.516 [8]	63.5 [8]	428 [19]
PMMA	58 [10]	1.4906 [10]	70 [7]	85.67 [19]

Table 3.1: Characteristics of materials commonly used in optics.

These three materials present roughly the same refractive index n and are all considered being low dispersion materials since their constringence, or Abbe number, V is above 45 [14].

Regarding the price, last year group asked for a quote request to PLASTISERVICE (Jumet, Belgium) and PRÄZISIONS GLAS & OPTIK GMBH (Iserlohn, Germany) [19]. It turned out PMMA was at least five times cheaper than the other materials.

Hence, the PMMA having similar optical properties than the other considered materials at a more affordable price, it was chosen to make the portholes out of this material.

In order to design the PMMA portholes it was required to simulate the stresses they will undergo during the nozzle utilization, the CAD software AUTODESK FUSION 360 was used to conduct these simulations. As the exact loads are difficult to implement, studies for different load cases were conducted.

[1] The constringence, or Abbe Number V of a transparent material is a measure of the material dispersion, the variation of refractive index with the wavelength [3].

[2] The refractive index n describes how light propagates through a medium and is defined as $n = \frac{c}{v}$, where c is the speed of light in vacuum and v is the light velocity in the medium [4].

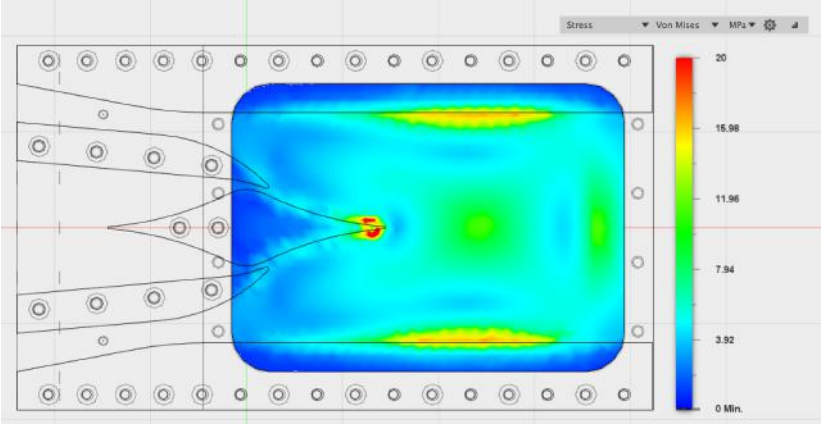

(a) Von Mises stress on the inside of the porthole.

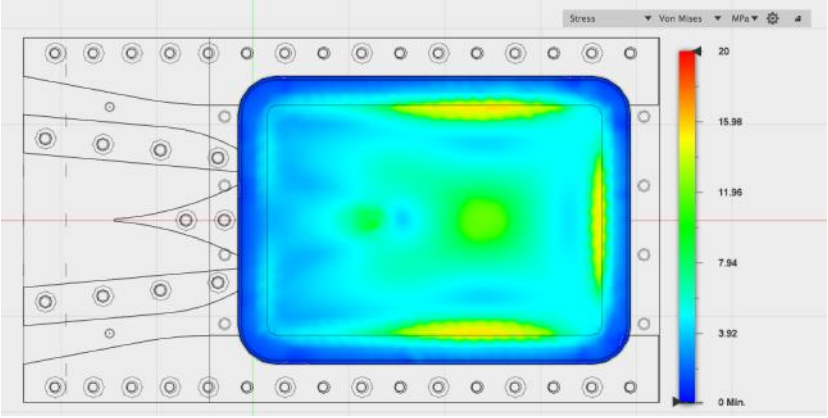

(b) Von Mises stress on the outside of the porthole.

Figure 3.18: Von Mises Stress for a uniform pressure of 10 *bar*.

- The first load case considered was a homogeneous pressure of 10 *bar* on the entire portholes. As it can be seen the maximal Von Mises stress is around 20 MPa. This stress, represented on figure 3.18, is quite high but stays below the yield strength of the PMMA which is of 70 MPa [7].

  Moreover this simulation is far away from the real cases since a 10 *bar* pressure in the entire nozzle is not meant to occur. Due to the fluid expansion the nozzle will rather experience a high pressure around the throat and a pressure close to the atmospheric pressure in the rest of the nozzle (due to the fluid expansion).

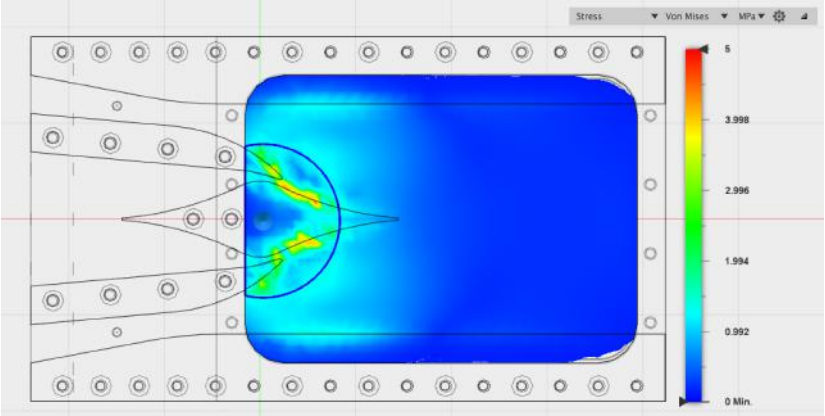

(a) Von Mises stress on the inside of the porthole.

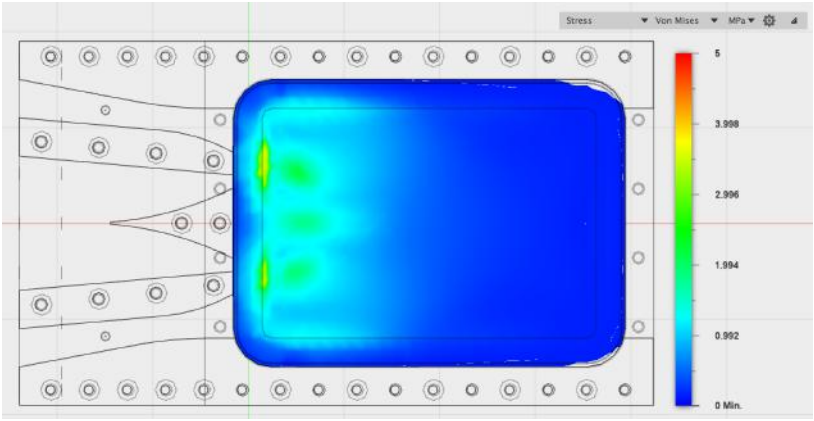

(b) Von Mises stress on the outside of the porthole.

Figure 3.19: Von Mises stress for a 10 bar pressure applied on a 40 mm radius circular area around the spike.

- In a second case illustrated on figure 3.19 a 10 bar pressure on a circular area of 40 mm radius around the spike was applied. In this case it can be noted that the maximal Von Mises stress is around 6 MPa.

- The last conducted simulation consisted in the application of a 10 bar pressure in two circular areas of 10 mm radius located at each throat. As illustrated here the maximal Von Mises stress stays way below the yield strength, as it doesn't exceed 1.5 MPa.

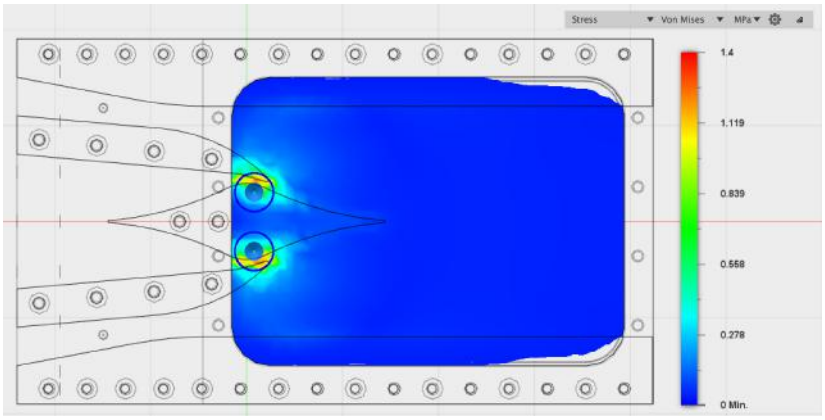

(a) Von Mises stress on the inside of the porthole.

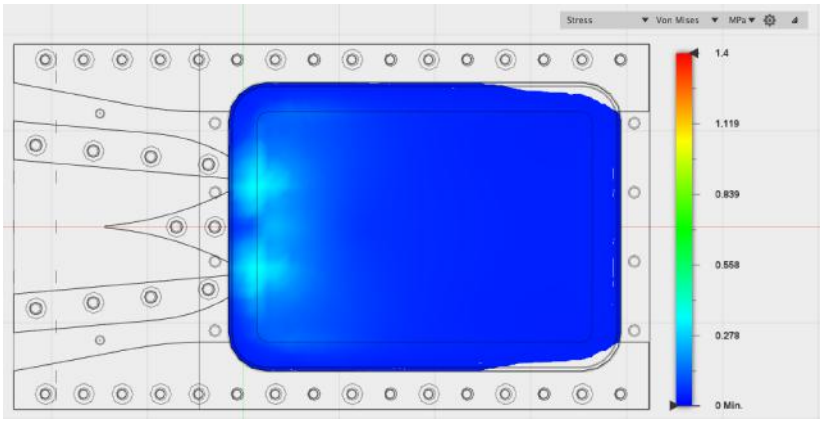

(b) Von Mises stress on the outside of the porthole.

Figure 3.20: Von Mises stress for a 10 *bar* pressure applied on two 10 *mm* radius circular areas around the throats.

To conclude the PMMA portholes should not be plastically deformed since the Von Mises stress never exceed the yield strength of the material. Moreover according to the simulations the maximal pressure applied on the portholes, which is around the throat, doesn't exceed 6 *bar* for a motive pressure of 10 *bar* .

The Plexiglas frames

The blue pieces are framing the PMMA portholes. These frames, here called Plexiglas frames, also close the flow on both side of the canal and contain it to a bi-dimensional flow. The combination of both Plexiglas frames (one on each side)

enables to position and clamp the canal pieces. In addition each frame will host two pressure sensors to measure the pressure drop created in the secondary canals by the primary flow drag effect.

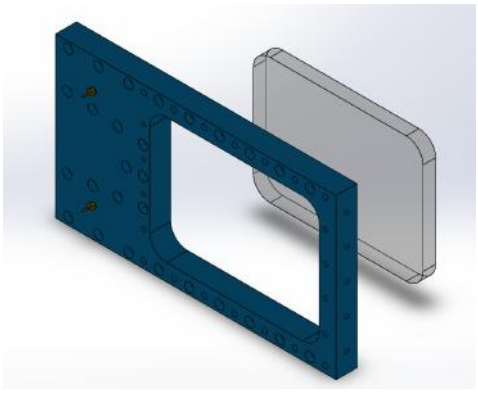

(a) The blue piece is framing the PMMA porthole.

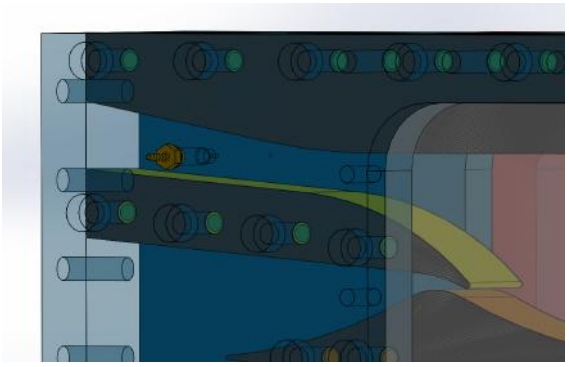

(b) Pressure sensors are hosted by the frame to measure the pressure drop created by the driven flow.

Figure 3.21: Plexiglas frame.

The exterior frames

The last pieces of the nozzle are the exterior frames. These frames ensure the sealing around the portholes and their alignment with the Plexiglas frames.

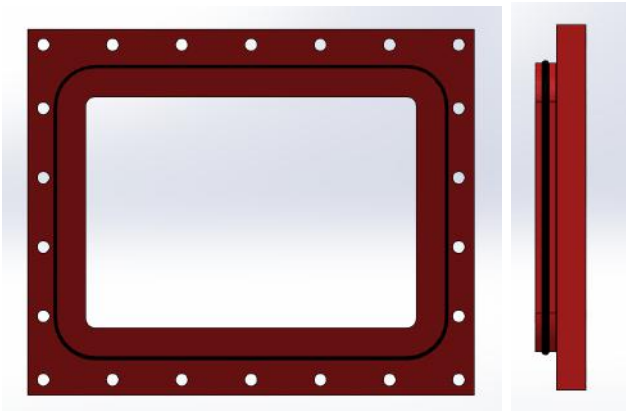

Figure 3.22: Exterior frame and O-ring joint seated in the frame groove.

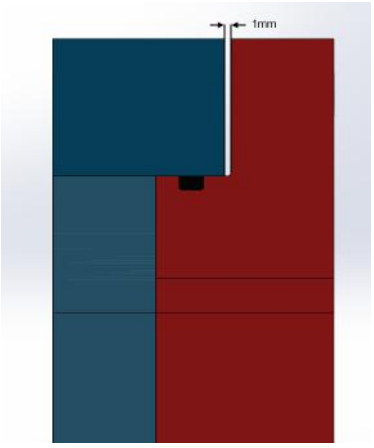

Figure 3.23: Sealing and alignment are ensured by the exterior frame.

As it can be seen on figures 3.22 the exterior frame is provided with a groove meant to host a O-ring joint. This joint is compressed during assembly between the two frames (Plexiglas and exterior) and creates a seal at the interface, as represented on figure 3.23.

Moreover, to be able to adjust the alignment of the PMMA portholes with the Plexiglas frames, a 1 mm slack was intentionally designed. This slack can be observed on figure 3.23 and prevent the porthole from not being compressed and aligned if its thickness were slightly thinner than 15 mm.

3.2.3 Chimneys and secondary flows

The last main part of the assembly is the pair of chimneys upstream of the secondary flow canals. Each chimney consists in a valve welded to a 90 ° angle canal, linked to the secondary flow canal via the back piece as represented on figure 3.24.

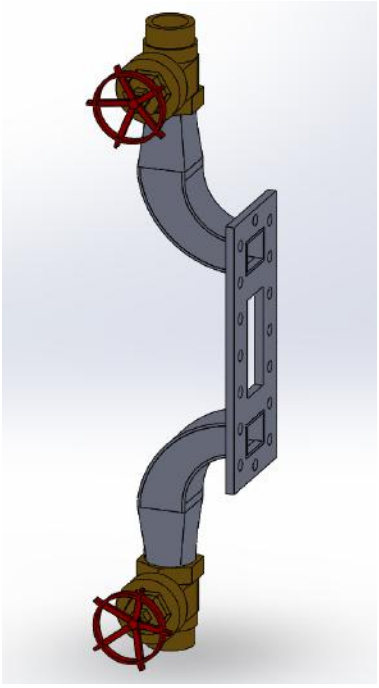

Figure 3.24: Secondary flow chimneys.

These chimneys will enable the regulation of the secondary flows driven by the primary flow.

By shutting the chimney valves no air flow will enter in the secondary flow canals where a depression will be created by the driven flow. This void should act as a low atmospheric pressure resulting in a larger expansion of the plume. The depression will be measured by the four pressure sensors placed on each side of the nozzle (on the Plexiglas frame, see figure 3.21(b)).

Chapter 4

Experimental results

This final chapter discloses the results obtained running tests on the designed test bench.

First, a brief theoretical reminder of the compressible flow phenomena expected is presented.

Secondly, visualizations of "standard flows", where the flow is influenced by a simple change in the motive pressure p_0, are displayed and commented. The cases considered here are:

- An **extremely over-expanded flow** set with $p_0 = 2\ [bar]$.
- An **over-expanded flow** observed for $p_0 = 4\ [bar]$ and $p_0 = 6\ [bar]$

Since the shadowgraph technique allows to visualize the Laplacian of the density $\nabla^2\rho$, the same value is computed from the simulation results in order to effectively compare simulations to reality.

The effect of a closing mechanism downstream of the canal and the secondary flow valves to eject the ambient air are then discussed. These air ejecting devices lower the canal stagnation pressure and thus alter the fluid expansion.

Finally, the end of this chapter will consist in a quick discussion over the various issues and problems encountered while setting up and using the test bench.

4.1 Phenomena description

Before disclosing the results obtained during the tests, it is interesting to go back to the basics of compressible flow phenomena in order to know what to expect and

understand what happens within the flow.

Along the spike of an aerospike nozzle two main phenomena interact: expansion waves with convex deviations of the flow and compression waves with concave deviations of the flow.

The sonic throat is oriented with an angle θ relative to the vertical, so that the flow makes the same angle θ with the horizontal line. That angle θ was set during the pre-design phase as:

$$\theta = \nu\left(M\left(\frac{p_0}{p_a} = \frac{8}{1}\right)\right) = 26.5° \tag{4.1}$$

where ν is the Prandtl-Meyer expansion angle, giving the deviation angle as a function of the final Mach number. In the this case, the final Mach number depends on the ratio between the stagnation pressure and the ambient pressure within the canal because the supersonic flow will be deviated and expanded until it reaches a state of pressure balance with the ambient air. Since the nozzle was designed for an optimum pressure ratio of $\frac{p_0}{p_a} = 8$, the initial direction of the flow will be purely horizontal only for that pressure ratio but the flow will reach supersonic velocities as soon as $p_0 \geq 1.89\,[bar]$. A range of supersonic flow regimes will thus be observable and it is important to understand the phenomena directing the behaviour of the plume. In order explain those regimes the figure 4.1 will be used for the description of the successive phenomena happening in the flow.

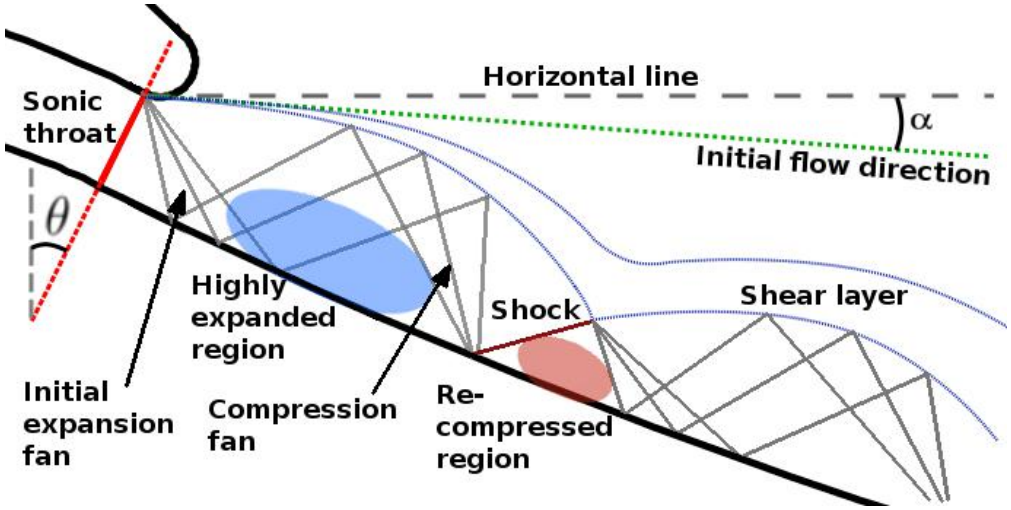

Figure 4.1: Sketch of compressible flow phenomena within an aerospike nozzle.

- Everything starts with the **initial expansion fan** at the sonic throat, as represented in gray on figure 4.1. This initial expansion deviates the flow towards the horizontal direction. As explained earlier the angle between the initial flow direction and the horizontal line is:

$$\alpha = \theta - \nu\left(M\left(p_0/p_a\right)\right)$$

and is equal to zero for the optimum pressure ratio $p_0/p_a = 8$. The value of this initial flow angle α is represented on graph 4.2 with the various visualization points that will be disclosed further in this chapter.

- The initial expansion fan is reflected on the spike towards the shear layer. This reflected expansion fan interacts with the precedent and expands the flow even more which results in a high fluid velocity (and thus high Mach number) and low fluid pressure in what can be described as a **highly expanded region**, shown in blue on figure 4.1. It is important to note that considering the waves as straight lines in every condition is a weak approximation of reality. Since the flow is deviated by these waves, expansion waves curve as well when interacting with each-other. The straight line approximation is only used for a basic explanation of the compressible flow phenomena.

- The expansion waves interact with the shear layer in two different ways: first they deviate it and second they are reflected by it as a compression fan. The deviation of the shear layer is simply due to the fact that the supersonic air travelling through the expansion fan is itself deviated, thus effectively deviating the shear layer separating it form the ambient air. This deviates the flow concavely and thus implies the reflection of the expansion fan as a compression fan. As said before, waves that interact with each-other don't stay straight. This is also true for compression waves and thus drawing them as straight lines is only an approximation.

- Since the compression waves converge they eventually meet and generate an **oblique compression shock**, represented in dark red in figure 4.1. This oblique compression shock slows the flow down and augments its pressure resulting in what can be called a **re-compressed region** shown in light red on figure 4.1.

- From that point onward, the flow behaves similarly as if it was just out of the throat: the re-compressed air leads to a second expansion fan which starts the whole process over again.

- The **shear layer**, separating the supersonic plume from the ambient air, is shown in dark blue on figure 4.1. It drags the air initially at rest in the canal thus augmenting its velocity. As the ambient air is accelerated the shear layer widens because the velocity transition occurs over a larger distance.

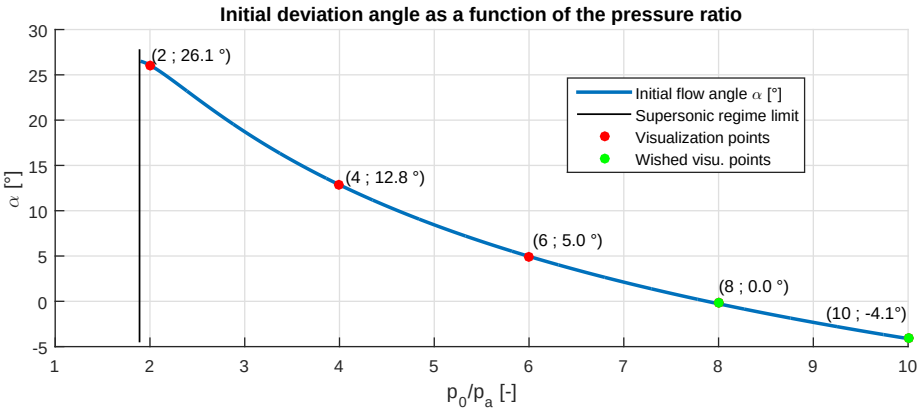

Figure 4.2: Initial flow angle α as a function of the ratio p_0/p_a.

4.2 Standard flows results and comparison with simulations

Extremely over-expanded flow

To observe this type of flow the motive pressure is set to 2 bar. By setting the stagnation pressure to such a low value, the flow is extremely over-expanded, which means that the deviation angle ν of the supersonic air flow at the throat is much

lower than the design angle θ. The resulting initial angle α of the flow is equal to: $\alpha = \theta - \nu = 26.1°$. The plume is thus very thin and remains pressed against the spike. The initial expansion fan at the throat is too small to impose a major deviation of the shear layer and thus is never reflected as a compression fan and no shock appears along the spike. Various Mach lines can be observed along the plume on the shadowgraph visualization on figure 4.3. These lines can be due to small imperfections on the spike walls that then reflect all along the spike flow. The absence of major expansion fan and shock explains the absence of major expanded or re-compressed regions as can be seen on picture 4.3.

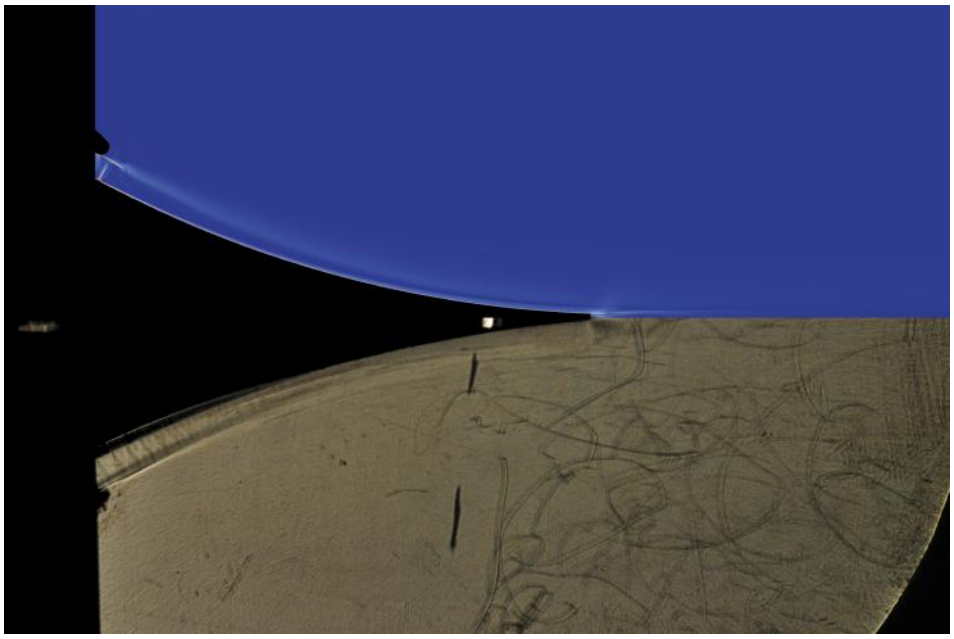

Figure 4.3: Shadowgraph visualization of the flow around the spike for $p_0 = 2\ bar$ (bottom) and equivalent numerical shadowgraph (top).

Over-expanded flow

The next regime to observe is an over-expanded flow. The supersonic flow stagnation pressure is, again, too low to give the plume a horizontal direction but is high enough to noticeably divert the flow from the spike and leads to some highly expanded and re-compressed regions. The two cases disclosed here correspond to motive pressures of 4 *bar* and 6 *bar* giving initial flow directions of 12.8° and 5.0° respectively. These regimes are shown on figure 4.4 ($p_0 = 4\ [bar]$) and figure 4.5 ($p_0 = 6\ [bar]$).

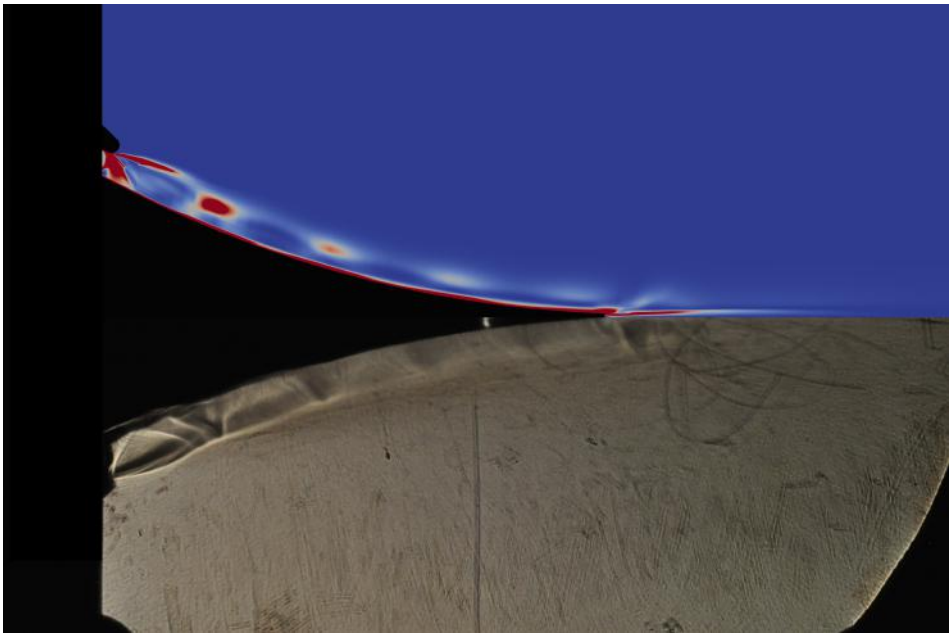

Figure 4.4: Shadowgraph visualization of the flow around the spike for $p_0 = 4\,bar$ (bottom) and equivalent numerical shadowgraph (top).

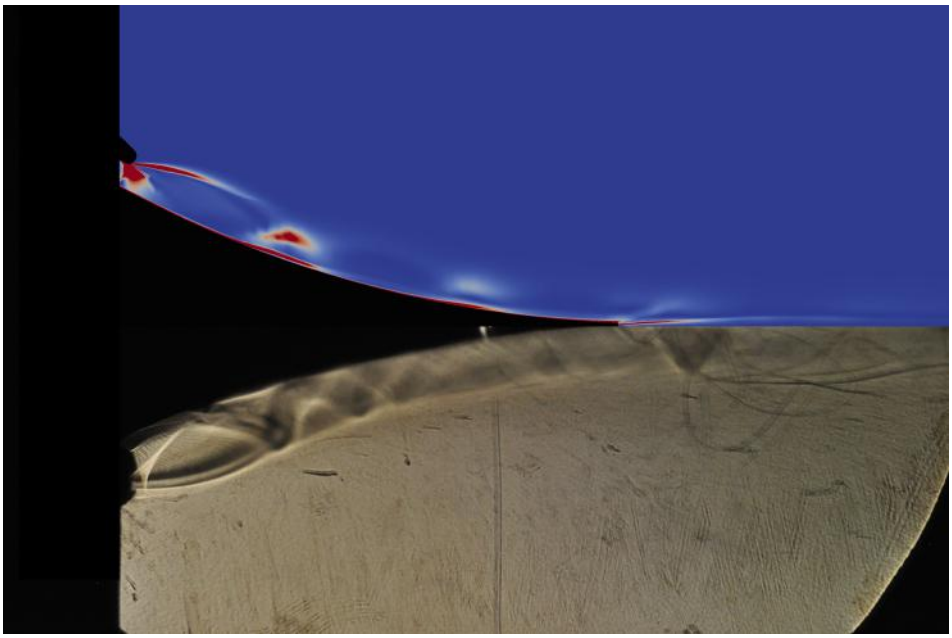

Figure 4.5: Shadowgraph visualization of the flow around the spike for $p_0 = 6\,bar$ (bottom) and equivalent numerical shadowgraph (top).

Once again, in order to link those results with the phenomena described in subsection 4.1 it is interesting to zoom in on certain parts of the flow to explain what is going on with more detail. Figure 4.6 is a close up view of the flow right after the throat. The initial expansion waves and the resulting expansion region are drawn in blue. The reflected compression waves are not drawn on the picture for clarity but as explained earlier they arise from the interaction between the expansion waves and the curved shear layer. They converge towards an oblique shock that generates a re-compressed region, both drawn in red on figure 4.6. The re-compressed region then goes through a second expansion fan and the whole process starts over again.

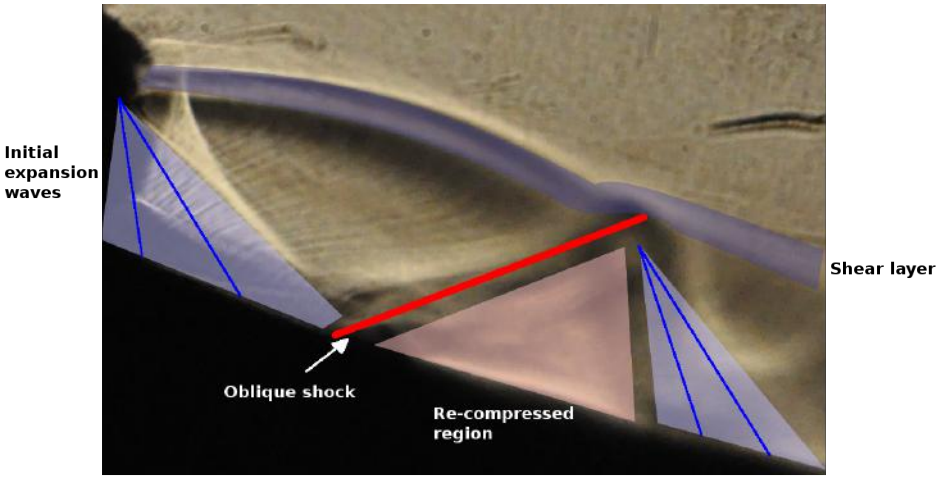

Figure 4.6: Shadowgraph visualization of the flow at the throat with schematics of phenomena.

Another interesting region of the flow is the end of the spike where the two supersonic primary flows interact as represented on figure 4.7. First the two boundary layer detach from the spike and generate a small recirculation region confined between the two primary supersonic flows as shown on figure 4.7. Since the two flows don't arrive perfectly horizontal, an abrupt change of direction has to take place through two oblique shocks. The upper oblique shock is shown in red on figure 4.7. These two shock also lead to a re-compressed region that later expands though an expansion fan. These symmetrical interactions between expansions and compressions are the source of the "Mach diamonds" pattern in the exhaust of nozzles.

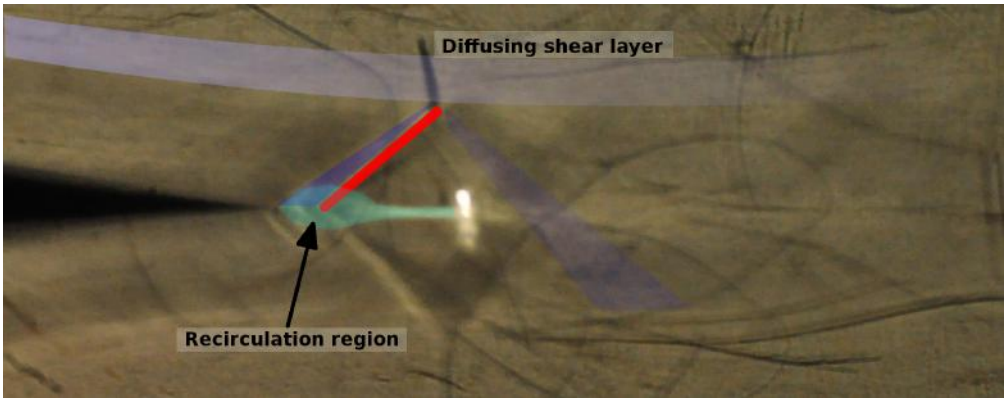

Figure 4.7: Shadowgraph visualization of the flow at the end of the spike with schematics of phenomena on one side of the flow.

A few major differences with the theory described in subsection 4.1 can however be observed. Since the point of this thesis is to give more insight into compressible flow phenomena through experimentation it is important to discuss them in detail.

- A **curvature** of the waves (expansion and compression) can be clearly observed. This means that "expansion waves" could start to converge through interaction with other waves thus becoming "compression waves" and vice versa. They are thus often referred to as "Mach waves". This curvature of the waves can be observed on figure 4.8.

- The oblique shocks are not perfectly thin nor straight.

- The shear layer doesn't start with a null width. This is due to the fact that the shear layer originates from the detachment of two boundary layers: one from the supersonic primary flow and the other from the secondary driven flow. These two boundary layers detach around the end of the spike border thus generating a form of "trailing edge" that turns into the shear layer.

- Finally it is important to notice that all the phenomena tend to diffuse in the flow and become less and less clearly visible downstream of the spike. This is also due to the fact that, as the flow progresses, the boundary layers on the canal side-walls grow and depth effects can no longer be neglected.

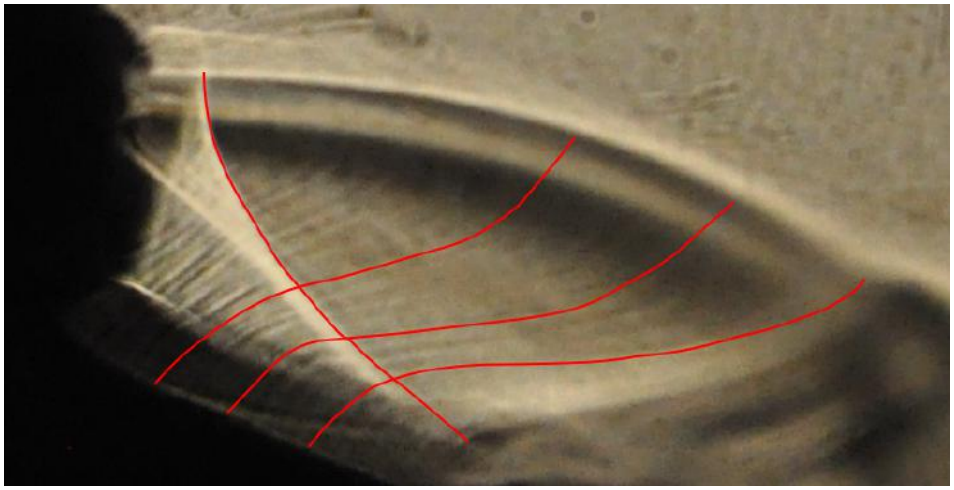

Figure 4.8: Shadowgraph visualization of the flow at the throat with wave curvature drawing.

4.3 Air-ejecting flow results

As explained before, the supersonic air plume interacts with the ambient air through a shear layer. This means that the supersonic flow drags the ambient air that was initially at rest and thus generates secondary driven flows on both of its sides. These secondary flows then exit the canal with the main supersonic flow downstream of the nozzle. This air, which is thus "ejected" out of the canal, needs to be replaced by air coming from the secondary flows chimneys and some recirculating air coming back in from the downstream opening of the canal. If this air can be stopped from getting in the canal, the ejected air wouldn't be replaced and the ambient pressure would thus drop. Two different methods have been implemented to do so and are disclosed in this section.

4.3.1 Secondary flow valves

The first method employed to inhibit the replacement of air within the canal is shutting the chimney valves, preventing thus any ambient air to enter the secondary flows through these chimneys. The ejected air is thus only replaced by the recirculating flow coming back in from the outlet of the nozzle.

Experiments were conducted to compare the flow expansion and the pressure drop for two different configurations : open and closed chimneys. For this test the motive pressure was set to $4\,bar$. The results are presented on fig 4.9. On

this figure the white lines represent the horizontal while the red lines represent the initial flow direction as defined in figure 4.1.

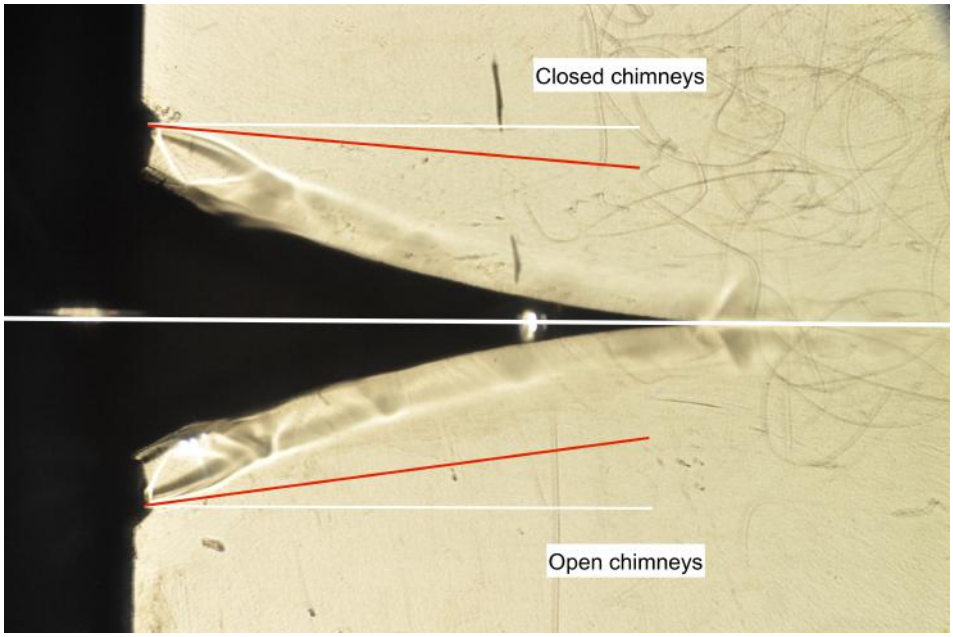

Figure 4.9: Shadowgraph comparison between flows for open and closed chimneys.

It can be seen on figure 4.9 that the difference between the flow expansions of the two case isn't extremely striking. This small differences can be confirmed by the pressure drop measured by the four pressure sensors, and plotted on figure 4.10.

As expected the measured pressure drop is slightly greater in the case of closed chimneys however this difference is rather small. The lowest measured pressure is 0.907 *bar* for open chimneys and 0.903 *bar* for closed chimneys.

The small effect of the valve shutting may be related to the rather low motive pressure set (compared to the optimal expansion pressure of 7.8 *bar* defined in chapter 1). However, because of vibrations of the test bench, it was impractical to set a higher motive pressure to test the effect of the chimney valves. The test bench began to vibrate when a 5 *bar* motive pressure was applied, making flow observations difficult due to movements of the shadowgraph system. This issue, combined with the large amount of condensation created within the nozzle, due to the ambient air humidity brought from the secondary flows, are the reasons all the previously described tests (see section 4.2) were conducted with closed chimneys.

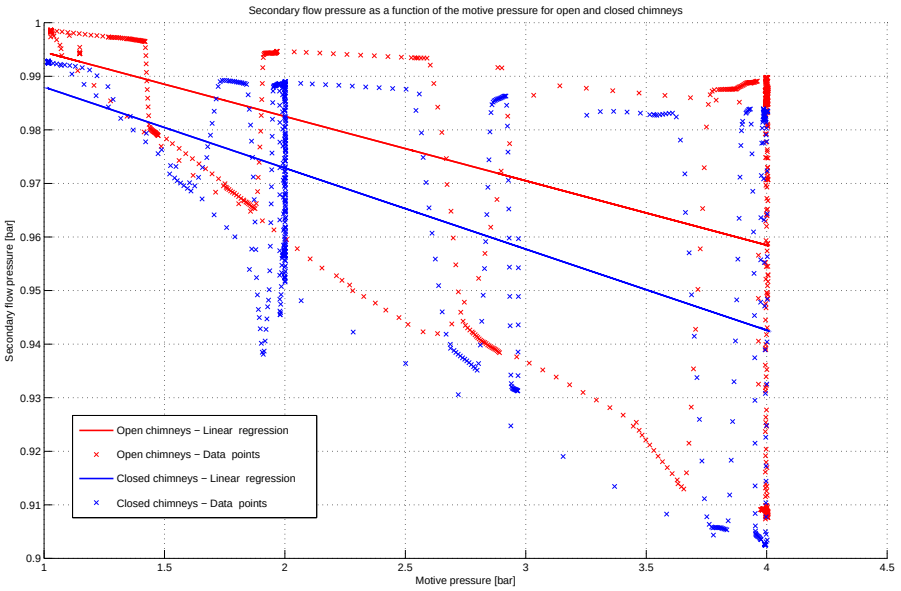

Figure 4.10: Pressure measurements for flows in open and closed chimneys configurations.

The large variations of the data points represented on figure 4.10 are due to the deflection of the flow and the fluid recirculation that is thus created in the canal.

Indeed a straight flow being unstable, the fluid tends to stick to one side of the canal (upper side or bottom side) and come off the other side. In this case the flow doesn't exit the nozzle in the horizontal direction, but is rather directed upwards or downwards. The major consequence of this phenomenon is that a recirculation flow is created in the canal side in which the flow took off while it ejects air on the other side. Hence one of the two secondary flows see its pressure dropping whereas the other one is constantly fed by the recirculation flow (coming from outside of the nozzle) and stays at a pressure close to the atmospheric pressure.

As the nozzle has four pressure sensors, two in each secondary flow canals, these two different pressure are measured resulting in large variation in the data points.

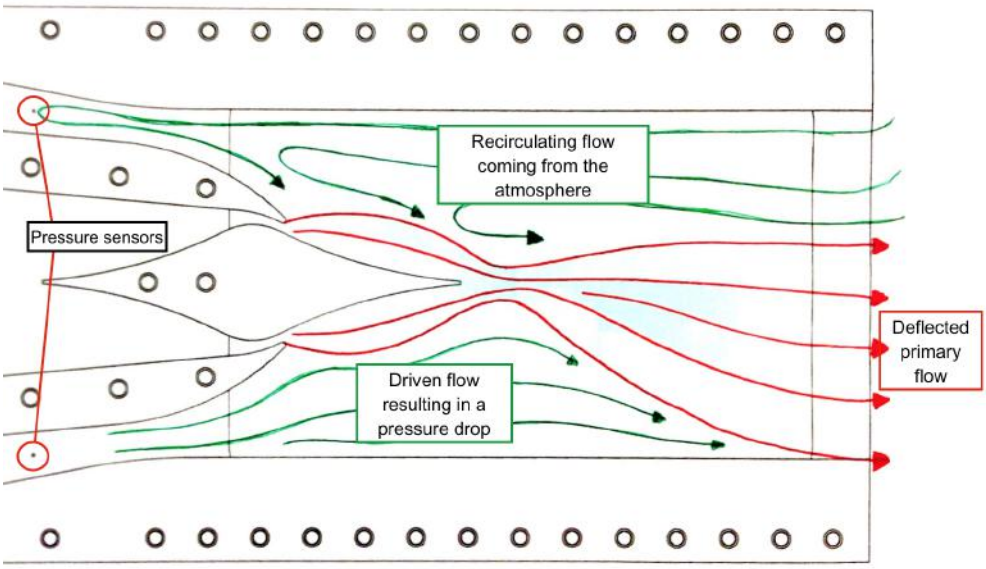

Figure 4.11: Sketch of the flow deflection.

4.3.2 Closing mechanism

The second method implemented to reduce the canal pressure is the installation of a closing mechanism at the end of the nozzle. The main objective is to cut the recirculating flow, thus preventing the air from coming back in the canal and ejecting air more effectively.

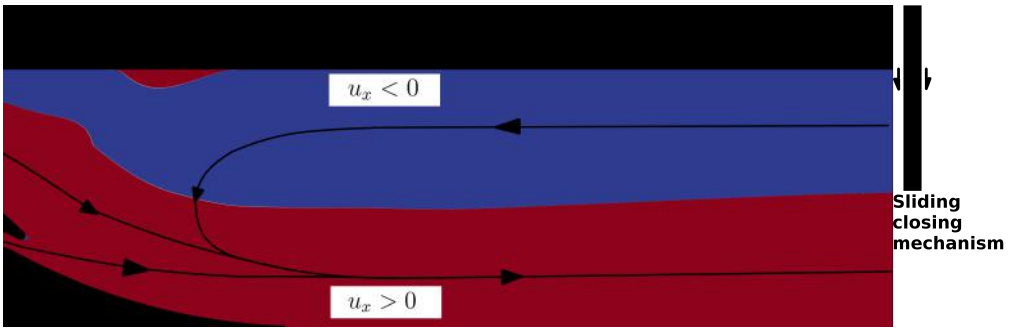

Figure 4.12: Simulation view of positive and negative horizontal velocities within the canal and closing mechanism.

As explained previously, the replacement of the ejected air will be limited and the mechanism will allow to artificially bring the ambient pressure in the canal p_a bellow its original value of 1 bar thus altering the fluid expansion.

As shown on figure 4.13, the closing mechanism is made of two metal plates sliding between the back end of the canal and two fixing pieces that are fixed to the canal with screws.

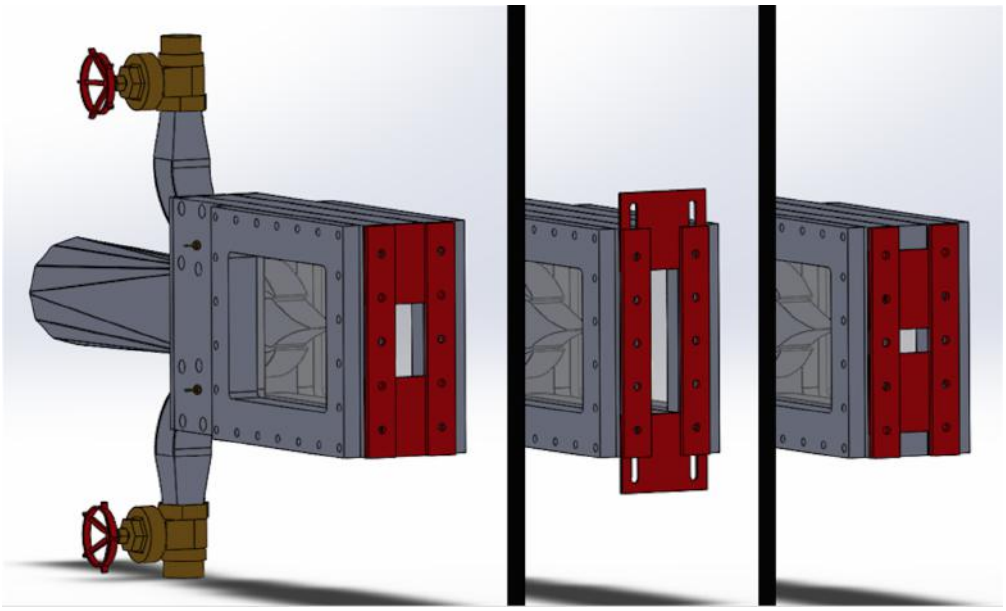

Figure 4.13: Closing mechanism designed to be attached downstream of the nozzle.

For the previously explained reasons (vibrations and condensation) these tests were conducted with closed chimneys, which limits even more the replacement of the ejected air.

Tests were carried out for different apertures of the outlet of the nozzle : 90 mm, 60 mm, 40 mm, and 30 mm (the original aperture, without the closing mechanism, being 120 mm). The visual results are presented on figure 4.14, while the pressure measurements are displayed on figures 4.15, 4.16, 4.17, 4.18 and 4.19.

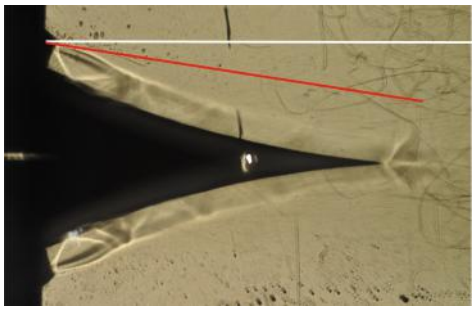

(a) 90 mm outlet.

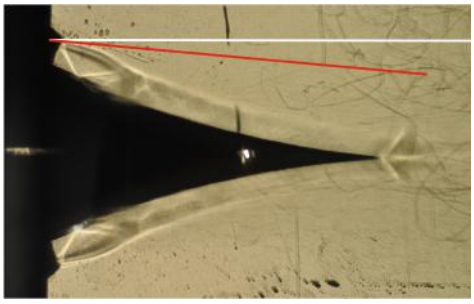

(b) 60 mm outlet.

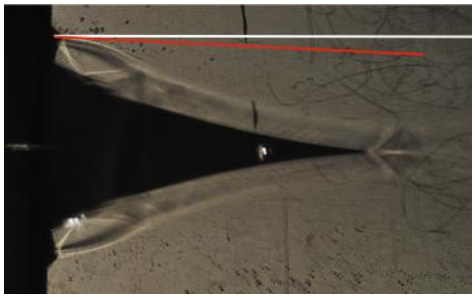

(c) 40 mm outlet.

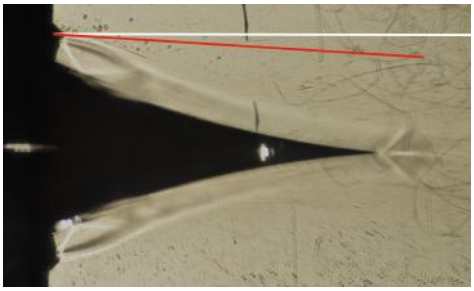

(d) 30 mm outlet.

Figure 4.14: Shadowgraph visualization of the flow around the spike for different outlet apertures.

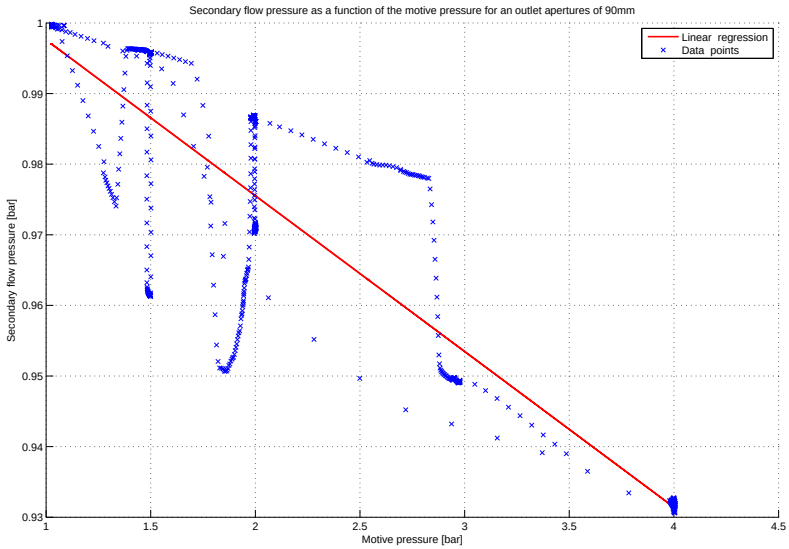

Figure 4.15: Secondary flow pressure as a function of the motive pressure for an outlet aperture of 90 mm.

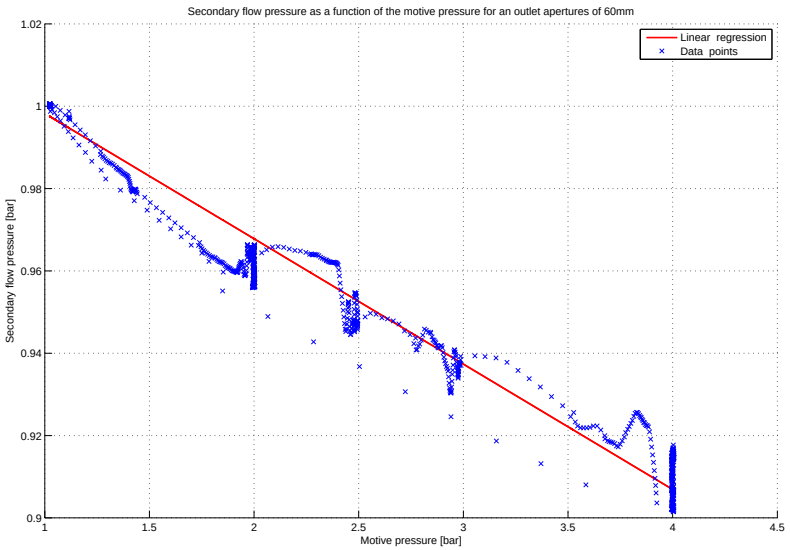

Figure 4.16: Secondary flow pressure as a function of the motive pressure for an outlet aperture of 60 mm.

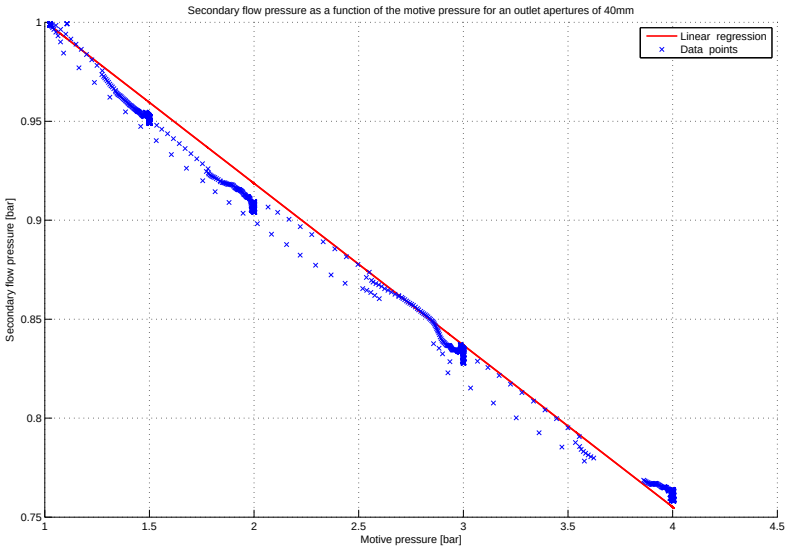

Figure 4.17: Secondary flow pressure as a function of the motive pressure for an outlet aperture of 40 mm.

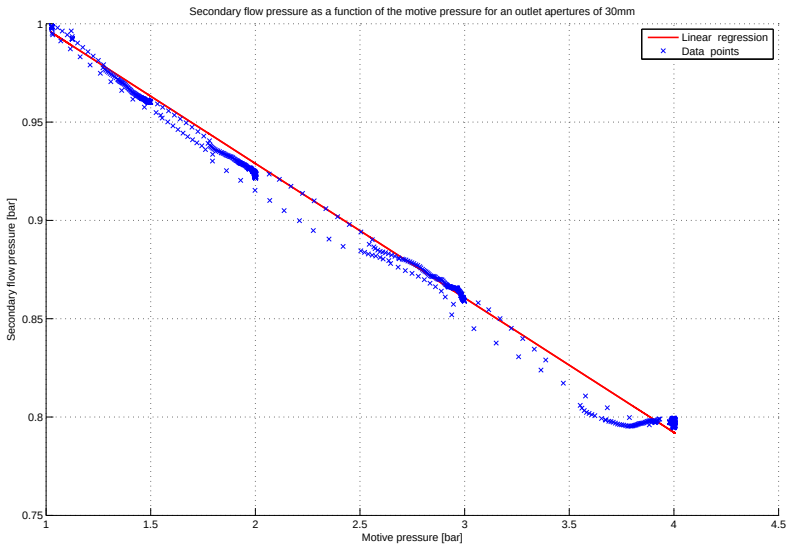

Figure 4.18: Secondary flow pressure as a function of the motive pressure for an outlet aperture of 30 mm.

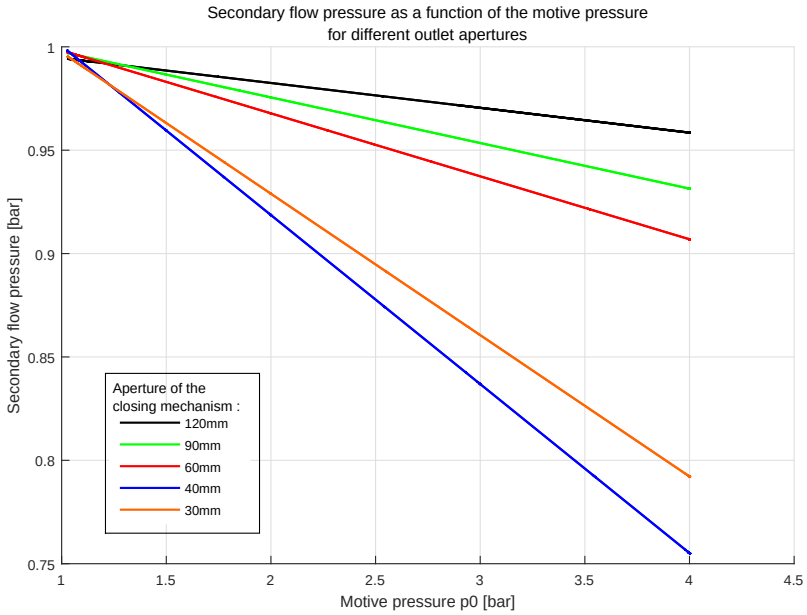

Figure 4.19: Secondary flow pressure as a function of the motive pressure for different outlet apertures.

It can be seen on figures 4.14 and 4.19 that the more the outlet is closed, the more the original flow direction is close to the horizontal and the more the pressure drops in the canal. Exception is made of the 30 mm aperture case, which have a greater original flow direction slope than the 40 mm aperture case. This can be explained by a too small aperture to effectively let all the air flow exit the canal. The closing mechanism cuts the flow at the shear layer and some air is thus reflected against the sliding metal plates back towards the inside of the canal. Since less air is ejected, the pressure doesn't drop as much as for the 40 mm aperture case. Logically, an optimal aperture exists between 30 mm and 40 mm for which the closing mechanism comes right at the edge of the shear layer, allowing the strongest pressure drop in the canal.

It can also be seen on the successive graphs presented on figures 4.15, 4.16, 4.17 and 4.18 that the aperture influences the flow deflection effect described in the previous section. This deflection effect and the pressure imbalance it generates tends to be damped by shutting the closing mechanism, and is almost non-existent for apertures smaller than 40 mm.

4.4 Major issues

While setting up and using the test bench a few issues and problems were encountered that are important to discuss here:

- When leaving the secondary flow valves opened, a flow of driven air coming from the chimneys appears. These secondary flows come from the ambient air which is humid. This humid air gets in contact with the nozzle metal and primary flow, which are very cold due to the expansions of the primary flow gas. The humidity then tends to condensate and droplets of water obstruct the visualization system. This condensation can be observed on figure 4.20.

  As represented on this figure, the condensation hampers the good visualization of the flow expansion since it tends to alter the expansion by mixing wit it and interacting with the shadowgraph refraction pattern. Moreover, the canal had to be cleaned of the condensation between each tests, which is a slow and delicate operation.

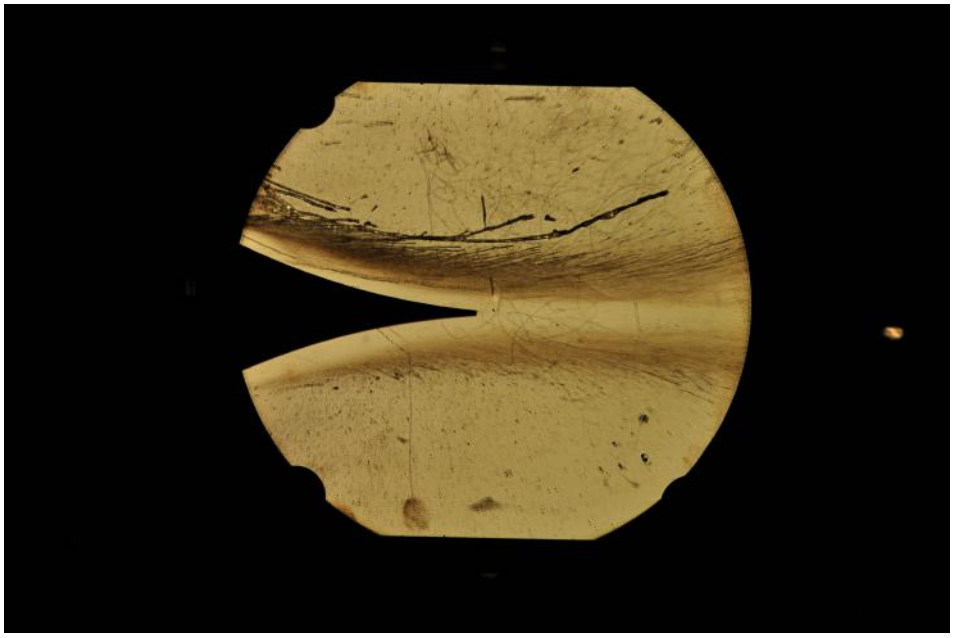

Figure 4.20: Condensation created within the nozzle when conducting tests with open chimneys.

- Another issue related to the secondary flows chimneys come from the vibrations generated when the valves are open. Indeed, the test bench being not very rigid it tends to vibrate when using high motive pressure with open chimneys.

  It seems that the flows through the chimneys unsettle the nozzle balance, creating the vibrations and making visualizations and picture taking difficult. However, these vibrations are almost non-existent when the chimney valves are closed. This indicates that the chimneys should be more rigid or better fixed to the test bench.

- When used at relatively high pressure, the test bench can make computers in the room crash. The men from the AF compressors have already been faced with that problem and suspect that this is due to air vibrations when supersonic high pressure air interacts with stagnant ambient air. The real reason is however still unknown.

- The assembly of the nozzle was done by hand and is thus not perfectly symmetric. Imprecisions have been brought below the 0.1 mm range thanks to great care during the assembly but some inevitable inaccuracies make the flow slightly asymmetric and lead to the flow deflection effect described previously.

- The PMMA was delivered and machined without proper care and is thus slightly scratched. Those scratches can be seen on the shadowgraph visualizations.

- A security valve set to 6 bar made it impossible to test all the flow regimes that were planned to be observed. This is also discussed later on in this work with possible ameliorations that could be brought to the test bench.

Conclusions

An aerospike nozzle has thus been designed and successfully implemented in the pre-existing test bench. As required, the nozzle can be used for teaching purposes by allowing a good visualization of various compressible flow phenomena thanks to the shadowgraph system. A closing mechanism and secondary flow valves allow for a modification of the canal ambient pressure using an air-ejecting effect. This test bench will enable the students from the *Aerodynamics of external flows [LMECA2323]* course to visualize a Prandtl-Meyer expansion fan, a shear layer and oblique compression shocks, hopefully giving them a better understanding of those phenomena.

The first step was a pre-design analysis using compressible flows theory in order to get the generic characteristics of the nozzle like the throat angle and area. The objective was to enable visualization of the various flow regimes: over-expanded, optimally expanded and under-expanded. Then, various machining and visualization criteria were applied to completely define the geometry of the nozzle.

In the second part the OpenFOAM software was used to run simulations and refine the design of the nozzle. After having chosen a numerical model for turbulent flows, an adequate mesh was created and boundary conditions were set. The numerical results then computed allowed to validate the nozzle geometry, as well as predict the value of different variable of interest like pressure, Mach number, fluid velocity and temperature.

The third step of this project was to design the aerospike nozzle that had to be implemented on the pre-existing test bench. Several machining and assembly criteria, as well as the already installed air intake system and visualization device had to be considered in order to do so. The implemented test bench now allows to observe the fluid expansion and the different related phenomena.

These results, as well as their study and comparisons with numerical simulations

are the matter addressed in the last part of this thesis and can be summarized as it follows:

- Shadowgraph visualizations of the flow around the nozzle effectively give a good insight into the behaviour of expansion waves, compression waves and their interaction with each-other as well as with a shear layer.

- An air ejecting system has been successfully implemented and makes it possible to decrease the pressure inside the canal. This pressure drop can be measured using the four pressure sensors set upstream of the secondary flows.

- These visualizations allow for a better understanding of the limitations of the assumptions made during the theoretical studies in the courses of fluid mechanics.

Further research and ameliorations

At the end of this thesis we would like to suggest some ameliorations and further researches that can be conducted in order to get more results. The lack of time and budget unfortunately prevented us to put them into application, but here are some suggestions and ideas :

- First, two types of improvement can be made regarding the secondary flow chimneys. The first one is installing additional fixations for the nozzle. Indeed the test bench isn't very rigid and the nozzle tends to vibrate when the valves of the secondary flows are open. The second one is linking the secondary chimneys to a clean and dry air source. This will allow to limit the apparition of condensation within the nozzle when conducting tests with open valves.

- Then, it is known that high level noises are created by the discharge of a jet of high pressure air through a nozzle and to the air. This is caused by the steep velocity gradient which exists across the boundary of the jet with the ambient fluid.

  Hence in order to limit these noises (and avoid the freezing of computers) it would be interesting to reduce the velocity gradient across the boundary of the jet with the ambient air. This can be done by increasing the canal length with an additional piece as represented on the figure 4.21.

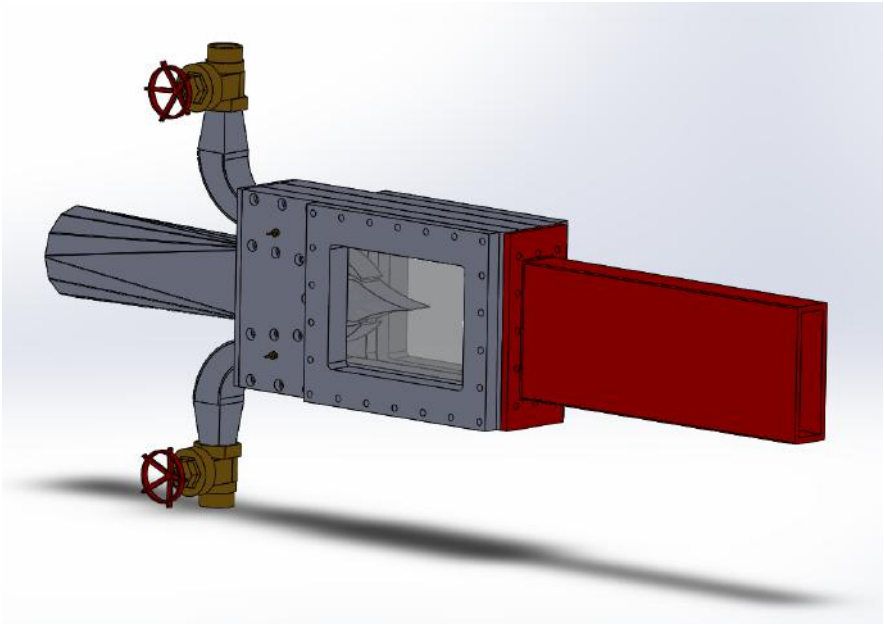

Figure 4.21: Additional piece for limiting the noises generated by the air flow through the nozzle.

Another solution that can be considered is to enlarge the mixing region between the high pressure gas and the ambient air. This method can be observed on aircraft engines since it applies particularly well to their revolution geometry.

- The last substantial improvement to make in order to fully profit of the installation is the change of the security valve placed after the air tank. This valve is limited to 6 *bar* and prevents the user to observe all the expansion regimes allowed by the aerospike nozzle. Exception made of the transition piece, all the parts of the test bench are designed and certified to withstand a 10 bar pressure. Hence tje change of the security valve has to be combined with the replacement of the actual transition piece by a certified one.

Appendix A

Design blueprints

In this appendix are presented the drawings of the different pieces of the designed nozzle. These drawings are developed in the following order : first half of the transition piece, then the canal borders, the spike borders, the spike, the PMMA portholes, the porthole frames and finally the exterior frames.

The following figure displays a semi-spilt view of the nozzle.

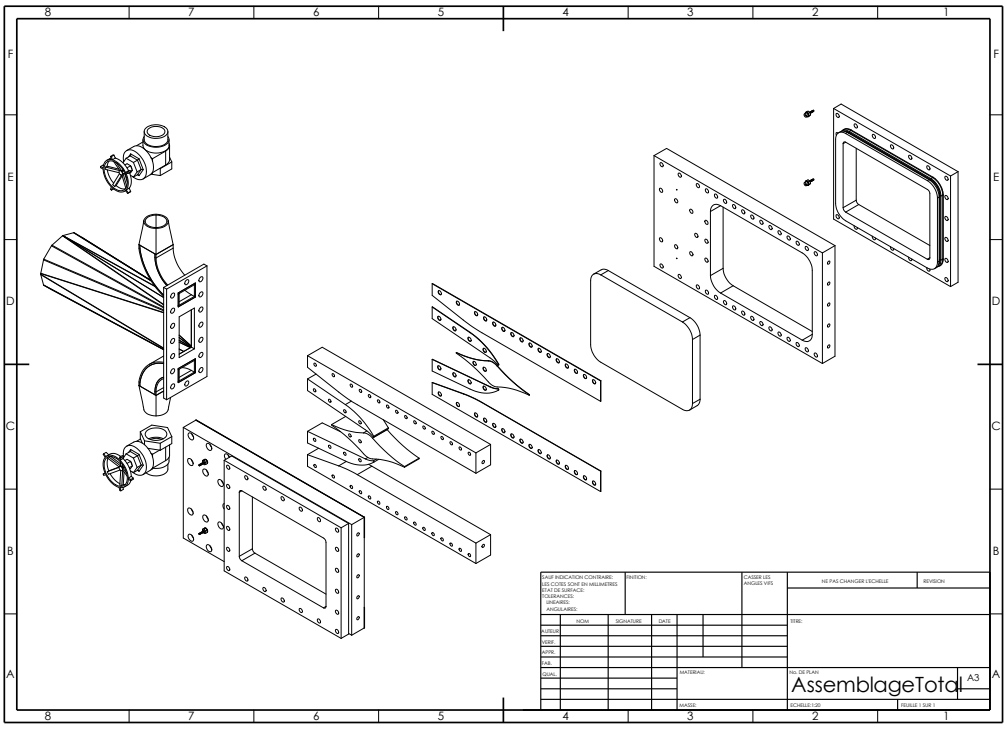

Semi-split view of the nozzle

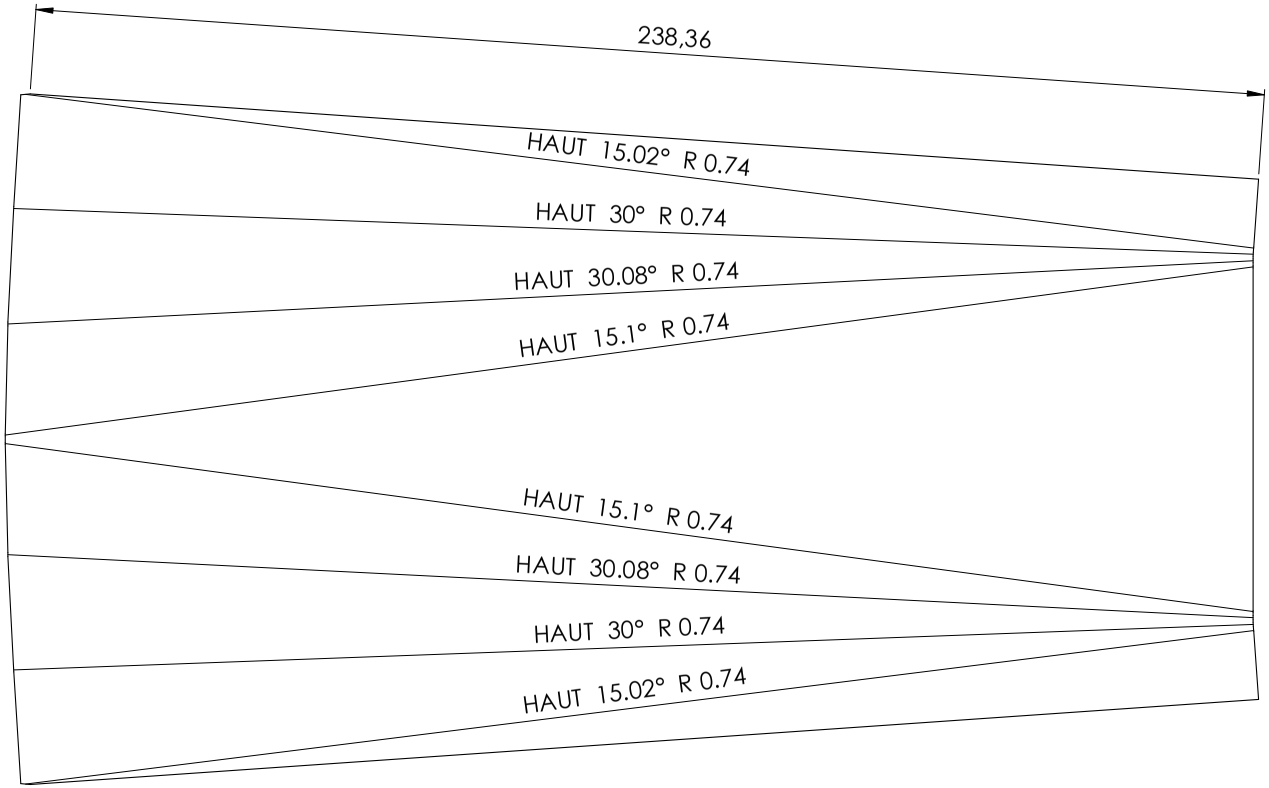

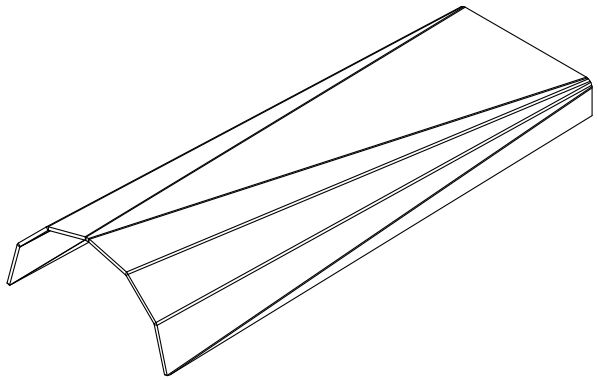

2 Exemplaires

SAUF INDICATION CONTRAIRE: LES COTES SONT EN MILLIMETRES ETAT DE SURFACE: TOLERANCES: LINEAIRES: ANGULAIRES:		FINITION:			CASSER LES ANGLES VIFS	NE PAS CHANGER L'ECHELLE	REVISION
	NOM	SIGNATURE	DATE			TITRE:	
AUTEUR							
VERIF.							
APPR.							
FAB.							
QUAL.				MATERIAU:		No. DE PLAN ToleTransition	A3
				MASSE:		ECHELLE:1:2	FEUILLE 1 SUR 1

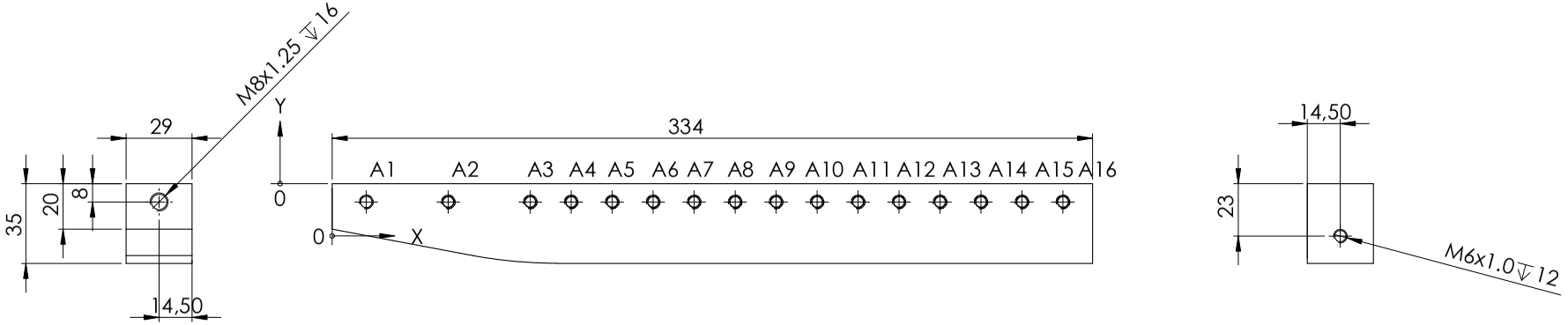

REPERE	POSITION X	POSITION Y	TAILLE
A1	15	-8	⌀ 5 ↧ 14.50 M6x1.0 - 6H ↧ 12
A2	51	-8	⌀ 5 ↧ 14.50 M6x1.0 - 6H ↧ 12
A3	87	-8	⌀ 5 ↧ 14.50 M6x1.0 - 6H ↧ 12
A4	105	-8	⌀ 5 ↧ 14.50 M6x1.0 - 6H ↧ 12
A5	123	-8	⌀ 5 ↧ 14.50 M6x1.0 - 6H ↧ 12
A6	141	-8	⌀ 5 ↧ 14.50 M6x1.0 - 6H ↧ 12
A7	159	-8	⌀ 5 ↧ 14.50 M6x1.0 - 6H ↧ 12
A8	177	-8	⌀ 5 ↧ 14.50 M6x1.0 - 6H ↧ 12
A9	195	-8	⌀ 5 ↧ 14.50 M6x1.0 - 6H ↧ 12
A10	213	-8	⌀ 5 ↧ 14.50 M6x1.0 - 6H ↧ 12
A11	231	-8	⌀ 5 ↧ 14.50 M6x1.0 - 6H ↧ 12
A12	249	-8	⌀ 5 ↧ 14.50 M6x1.0 - 6H ↧ 12
A13	267	-8	⌀ 5 ↧ 14.50 M6x1.0 - 6H ↧ 12
A14	285	-8	⌀ 5 ↧ 14.50 M6x1.0 - 6H ↧ 12
A15	303	-8	⌀ 5 ↧ 14.50 M6x1.0 - 6H ↧ 12
A16	321	-8	⌀ 5 ↧ 14.50 M6x1.0 - 6H ↧ 12

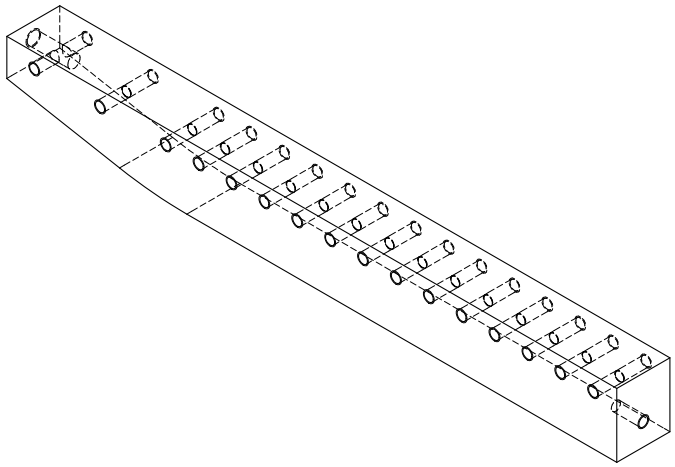

2 Exemplaires

Tolérances générales : $^{+}_{-}$ 0.1mm

SAUF INDICATION CONTRAIRE: LES COTES SONT EN MILLIMETRES ETAT DE SURFACE: TOLERANCES: LINEAIRES: ANGULAIRES:	FINITION:		CASSER LES ANGLES VIFS	NE PAS CHANGER L'ECHELLE		REVISION	
	NOM	SIGNATURE	DATE				TITRE:
AUTEUR							
VERIF.							
APPR.							
FAB.							
QUAL.				MATERIAU:		No. DE PLAN	A3
						CanalUp	
				MASSE:		ECHELLE:1:2	FEUILLE 1 SUR 1

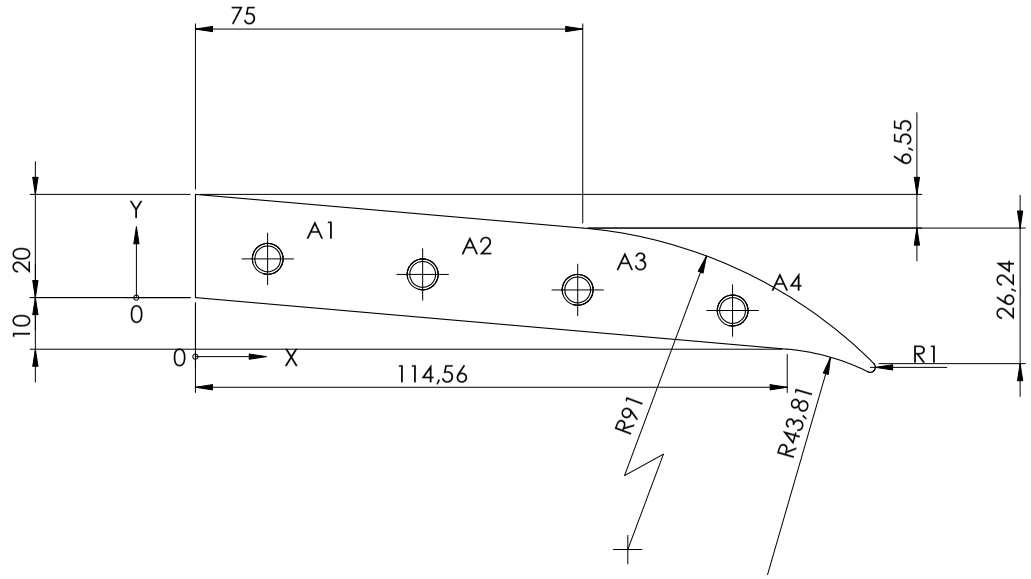

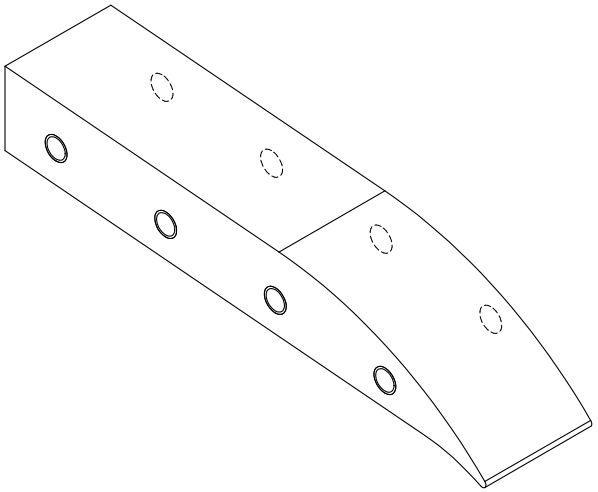

REPERE	POSITION X	POSITION Y	TAILLE
A1	14	7,50	⌀ 5 ↧ 14.50 M6x1.0 - 6H ↧ 12
A2	44	4,50	⌀ 5 ↧ 14.50 M6x1.0 - 6H ↧ 12
A3	74	1,50	⌀ 5 ↧ 14.50 M6x1.0 - 6H ↧ 12
A4	104	-2,50	⌀ 5 ↧ 14.50 M6x1.0 - 6H ↧ 12

2 Exemplaires

Tolérances générales : $^{+}_{-}$ 0.1mm

SAUF INDICATION CONTRAIRE: LES COTES SONT EN MILLIMETRES ETAT DE SURFACE: TOLERANCES: LINEAIRES: ANGULAIRES:		FINITION:		CASSER LES ANGLES VIFS		NE PAS CHANGER L'ECHELLE	REVISION
	NOM	SIGNATURE	DATE			TITRE:	
AUTEUR							
VERIF.							
APPR.							
FAB.							
QUAL.				MATERIAU:		No. DE PLAN SpikeTop	A3
				MASSE:		ECHELLE:1:1	FEUILLE 1 SUR 1

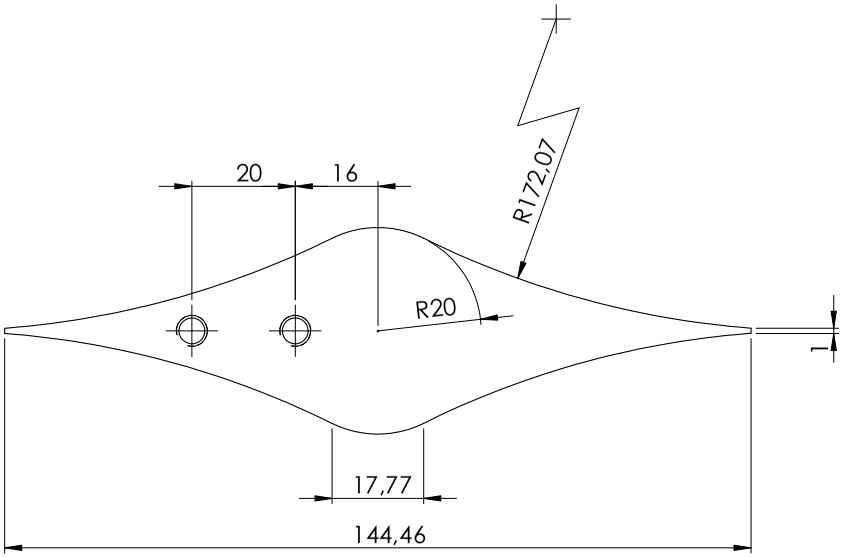

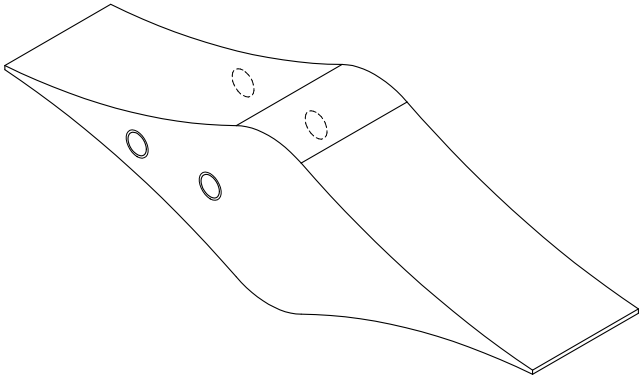

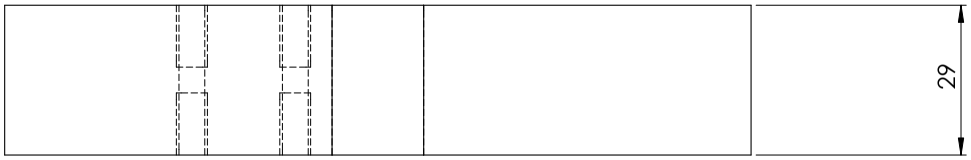

Tolérances générales : $^{+}_{-}$ 0.1mm

SAUF INDICATION CONTRAIRE: LES COTES SONT EN MILLIMETRES ETAT DE SURFACE: TOLERANCES: LINEAIRES: ANGULAIRES:	FINITION:			CASSER LES ANGLES VIFS	NE PAS CHANGER L'ECHELLE	REVISION	
	NOM	SIGNATURE	DATE		TITRE:		
AUTEUR							
VERIF.							
APPR.							
FAB.							
QUAL.				MATERIAU:	No. DE PLAN	A3	
					Spike		
				MASSE:	ECHELLE:1:1	FEUILLE 1 SUR 1	

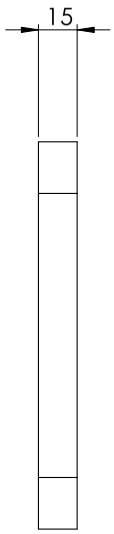

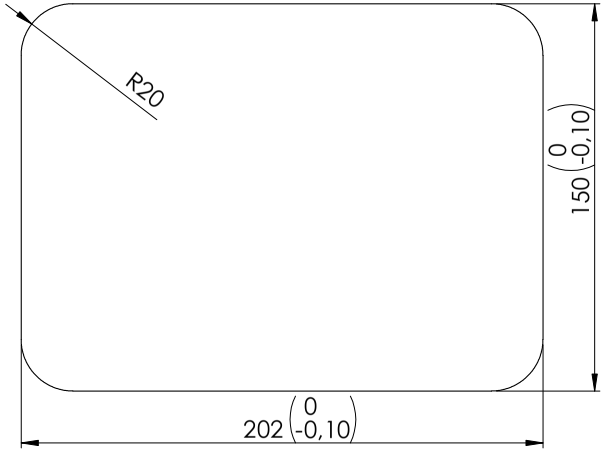

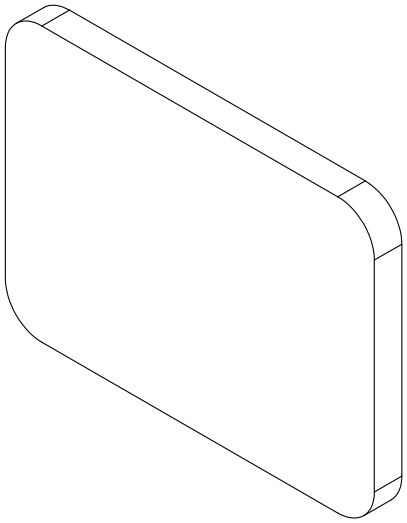

2 Exemplaires

SAUF INDICATION CONTRAIRE: LES COTES SONT EN MILLIMETRES ETAT DE SURFACE: TOLERANCES: LINEAIRES: ANGULAIRES:	FINITION:		CASSER LES ANGLES VIFS	NE PAS CHANGER L'ECHELLE	REVISION		
	NOM	SIGNATURE	DATE				TITRE:
AUTEUR							
VERIF.							
APPR.							
FAB.							
QUAL.				MATERIAU:			No. DE PLAN Plexi
							A3
				MASSE:		ECHELLE:1:2	FEUILLE 1 SUR 1

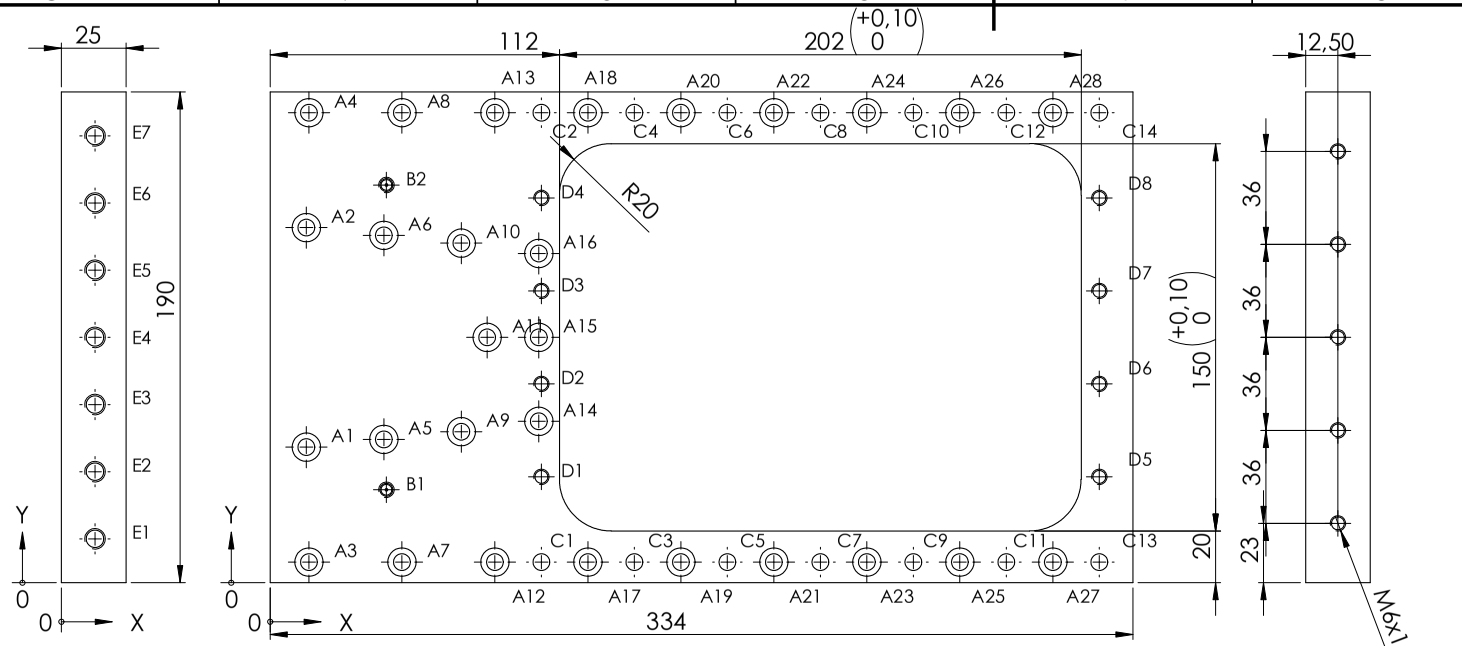

REPERE	POSITION X	POSITION Y	TAILLE
A1	14	52,50	⌀6.50 A TRAVERS TOUT ⌴ ⌀11↧7
A2	14	137,50	⌀6.50 A TRAVERS TOUT ⌴ ⌀11↧7
A3	15	8	⌀6.50 A TRAVERS TOUT ⌴ ⌀11↧7
A4	15	182	⌀6.50 A TRAVERS TOUT ⌴ ⌀11↧7
A5	44	55,50	⌀6.50 A TRAVERS TOUT ⌴ ⌀11↧7
A6	44	134,50	⌀6.50 A TRAVERS TOUT ⌴ ⌀11↧7
A7	51	8	⌀6.50 A TRAVERS TOUT ⌴ ⌀11↧7
A8	51	182	⌀6.50 A TRAVERS TOUT ⌴ ⌀11↧7
A9	74	58,50	⌀6.50 A TRAVERS TOUT ⌴ ⌀11↧7
A10	74	131,50	⌀6.50 A TRAVERS TOUT ⌴ ⌀11↧7
A11	84	95	⌀6.50 A TRAVERS TOUT ⌴ ⌀11↧7
A12	87	8	⌀6.50 A TRAVERS TOUT ⌴ ⌀11↧7
A13	87	182	⌀6.50 A TRAVERS TOUT ⌴ ⌀11↧7
A14	104	62,50	⌀6.50 A TRAVERS TOUT ⌴ ⌀11↧7
A15	104	95	⌀6.50 A TRAVERS TOUT ⌴ ⌀11↧7
A16	104	127,50	⌀6.50 A TRAVERS TOUT ⌴ ⌀11↧7
A17	123	8	⌀6.50 A TRAVERS TOUT ⌴ ⌀11↧7
A18	123	182	⌀6.50 A TRAVERS TOUT ⌴ ⌀11↧7
A19	159	8	⌀6.50 A TRAVERS TOUT ⌴ ⌀11↧7
A20	159	182	⌀6.50 A TRAVERS TOUT ⌴ ⌀11↧7
A21	195	8	⌀6.50 A TRAVERS TOUT ⌴ ⌀11↧7
A22	195	182	⌀6.50 A TRAVERS TOUT ⌴ ⌀11↧7
A23	231	8	⌀6.50 A TRAVERS TOUT ⌴ ⌀11↧7
A24	231	182	⌀6.50 A TRAVERS TOUT ⌴ ⌀11↧7
A25	267	8	⌀6.50 A TRAVERS TOUT ⌴ ⌀11↧7
A26	267	182	⌀6.50 A TRAVERS TOUT ⌴ ⌀11↧7
A27	303	8	⌀6.50 A TRAVERS TOUT ⌴ ⌀11↧7
A28	303	182	⌀6.50 A TRAVERS TOUT ⌴ ⌀11↧7
B1	45	36	⌀1 A TRAVERS TOUT ⌀ 5 ↧ 17 M6x1.0 - 6H ↧ 12
B2	45	154	⌀1 A TRAVERS TOUT ⌀ 5 ↧ 17 M6x1.0 - 6H ↧ 12
C1	105	8	⌀6,50 A TRAVERS TOUT
C2	105	182	⌀6,50 A TRAVERS TOUT
C3	141	8	⌀6,50 A TRAVERS TOUT
C4	141	182	⌀6,50 A TRAVERS TOUT
C5	177	8	⌀6,50 A TRAVERS TOUT
C6	177	182	⌀6,50 A TRAVERS TOUT
C7	213	8	⌀6,50 A TRAVERS TOUT
C8	213	182	⌀6,50 A TRAVERS TOUT
C9	249	8	⌀6,50 A TRAVERS TOUT
C10	249	182	⌀6,50 A TRAVERS TOUT
C11	285	8	⌀6,50 A TRAVERS TOUT
C12	285	182	⌀6,50 A TRAVERS TOUT
C13	321	8	⌀6,50 A TRAVERS TOUT
C14	321	182	⌀6,50 A TRAVERS TOUT
D1	105	41	⌀ 5 ↧ 15 M6x1.0 - 6H ↧ 12
D2	105	77	⌀ 5 ↧ 15 M6x1.0 - 6H ↧ 12
D3	105	113	⌀ 5 ↧ 15 M6x1.0 - 6H ↧ 12
D4	105	149	⌀ 5 ↧ 15 M6x1.0 - 6H ↧ 12
D5	321	41	⌀ 5 ↧ 15 M6x1.0 - 6H ↧ 12
D6	321	77	⌀ 5 ↧ 15 M6x1.0 - 6H ↧ 12
D7	321	113	⌀ 5 ↧ 15 M6x1.0 - 6H ↧ 12
D8	321	149	⌀ 5 ↧ 15 M6x1.0 - 6H ↧ 12
E1	13	17	⌀ 6,80 ↧ 22,25 M8x1.25 - 6H ↧ 16
E2	13	43	⌀ 6,80 ↧ 22,25 M8x1.25 - 6H ↧ 16
E3	13	69	⌀ 6,80 ↧ 22,25 M8x1.25 - 6H ↧ 16
E4	13	95	⌀ 6,80 ↧ 22,25 M8x1.25 - 6H ↧ 16
E5	13	121	⌀ 6,80 ↧ 22,25 M8x1.25 - 6H ↧ 16
E6	13	147	⌀ 6,80 ↧ 22,25 M8x1.25 - 6H ↧ 16
E7	13	173	⌀ 6,80 ↧ 22,25 M8x1.25 - 6H ↧ 16

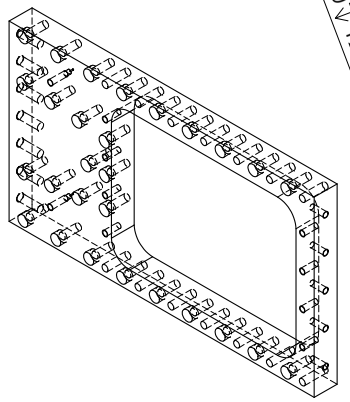

2 Exemplaires

Tolérances générales : $^{+}_{-}$ 0.1mm

SAUF INDICATION CONTRAIRE: LES COTES SONT EN MILLIMETRES ETAT DE SURFACE: TOLERANCES: LINEAIRES: ANGULAIRES:	FINITION:	CASSER LES ANGLES VIFS	NE PAS CHANGER L'ECHELLE / REVISION

	NOM	SIGNATURE	DATE
AUTEUR			
VERIF.			
APPR.			
FAB.			
QUAL.			

MATERIAU:

MASSE:

TITRE:

No. DE PLAN: CadrePlexi

A3

ECHELLE:1:2

FEUILLE 1 SUR 1

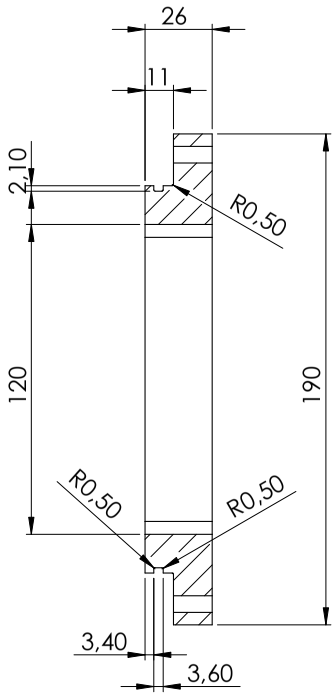

COUPE A-A
ECHELLE 1 : 2

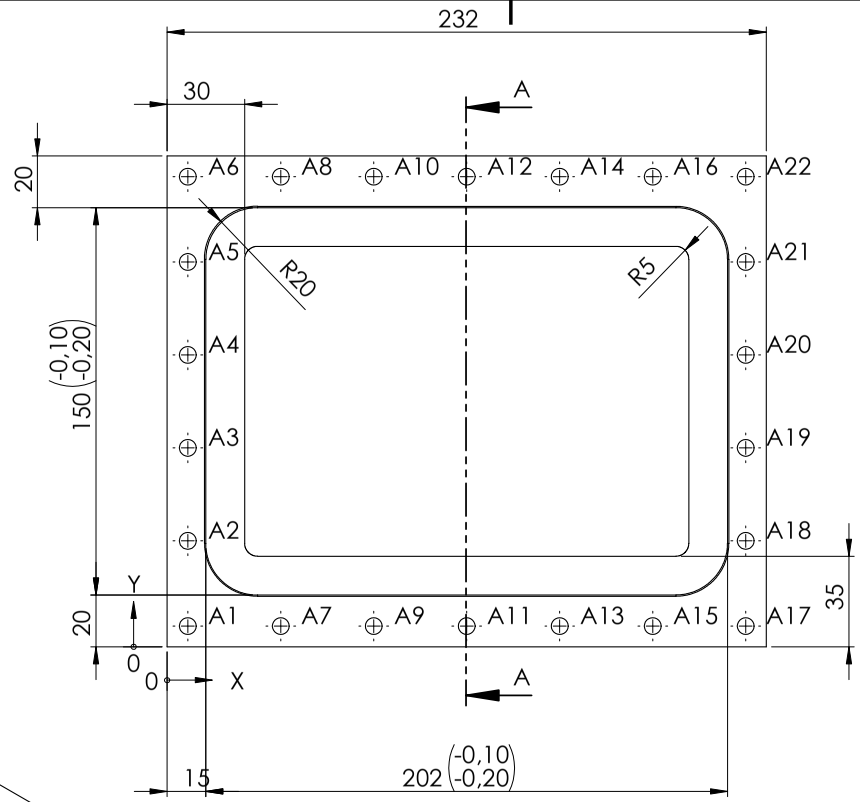

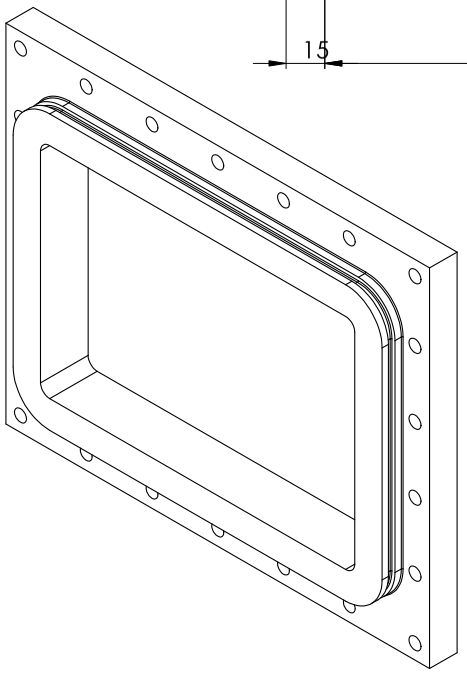

REPERE	POSITION X	POSITION Y	TAILLE
A1	8	8	∅6,50 A TRAVERS TOUT
A2	8	41	∅6,50 A TRAVERS TOUT
A3	8	77	∅6,50 A TRAVERS TOUT
A4	8	113	∅6,50 A TRAVERS TOUT
A5	8	149	∅6,50 A TRAVERS TOUT
A6	8	182	∅6,50 A TRAVERS TOUT
A7	44	8	∅6,50 A TRAVERS TOUT
A8	44	182	∅6,50 A TRAVERS TOUT
A9	80	8	∅6,50 A TRAVERS TOUT
A10	80	182	∅6,50 A TRAVERS TOUT
A11	116	8	∅6,50 A TRAVERS TOUT
A12	116	182	∅6,50 A TRAVERS TOUT
A13	152	8	∅6,50 A TRAVERS TOUT
A14	152	182	∅6,50 A TRAVERS TOUT
A15	188	8	∅6,50 A TRAVERS TOUT
A16	188	182	∅6,50 A TRAVERS TOUT
A17	224	8	∅6,50 A TRAVERS TOUT
A18	224	41	∅6,50 A TRAVERS TOUT
A19	224	77	∅6,50 A TRAVERS TOUT
A20	224	113	∅6,50 A TRAVERS TOUT
A21	224	149	∅6,50 A TRAVERS TOUT
A22	224	182	∅6,50 A TRAVERS TOUT

2 Exemplaires

Tolérances générales : $^{+}_{-}$ 0.1mm

SAUF INDICATION CONTRAIRE: LES COTES SONT EN MILLIMETRES ETAT DE SURFACE: TOLERANCES: LINEAIRES: ANGULAIRES:	FINITION:	CASSER LES ANGLES VIFS	NE PAS CHANGER L'ECHELLE / REVISION

	NOM	SIGNATURE	DATE
AUTEUR			
VERIF.			
APPR.			
FAB.			
QUAL.			

MATERIAU:

MASSE:

TITRE:

No. DE PLAN: CadreExterieur

A3

ECHELLE:1:1

FEUILLE 1 SUR 1

Appendix B

Aerospike Nozzle: Lab procedure

1 Connection to the compressor

1. First verify the right orifice plate is in place between the two part of the stabilization pipe. This plate should have a 60 mm diameter hole in it. If it isn't the right orifice plate replace it (with the flat face facing the output of the compressor).

2. Connect the stabilization pipe to the transition piece of the nozzle. For easier manipulation you can unscrew the flanges located at the elbow (connecting the stabilization pipe to the black flexible pipe), this will allow you to turn the elbow (and orient it horizontally).

3. Connect the pressure an temperature sensors to the test bench. These sensors should be connected to the data acquisition box located behind the test bench. The sensors are the following :
   - P002Ap, connected to the electro-valve (need to be screwed).
   - P100Ap, connected to the pressure sensor on the stabilization pipe (need to be screwed too).
   - T101Ap, connected to the temperature sensor on the stabilization pipe.
   - P102Ap, connected to the differential pressure flow-meter.
   - P104Ap, connected to the multiplexer.

4. Check the horizontality of the canal. If necessary adjust the inclination with the supporting screw under the nozzle.

5. Turn on the data acquisition box and the acquisition card.

6. Set the 4 switches of the multiplexer on PLC.

7. Verify that every flanges and clamping rings are tighten.

8. Engage the brakes of the test bench.

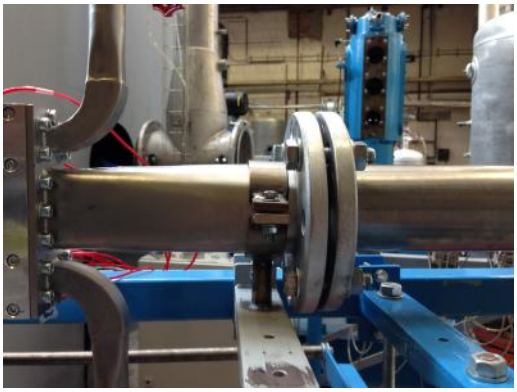

2.

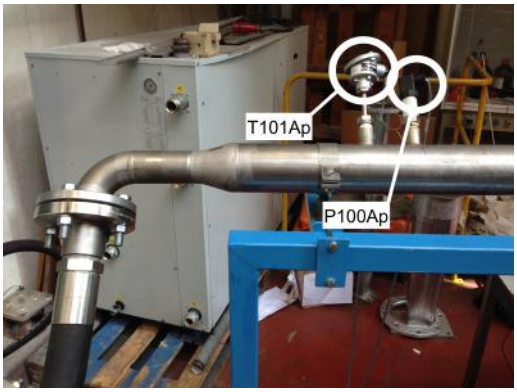

2. & 3.

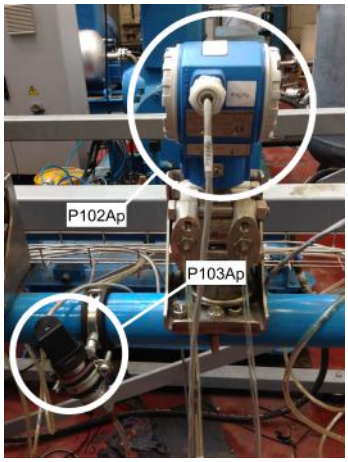

3.

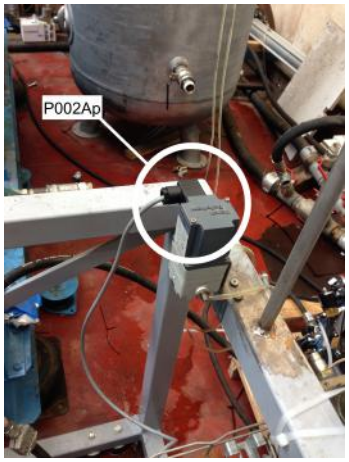

3.

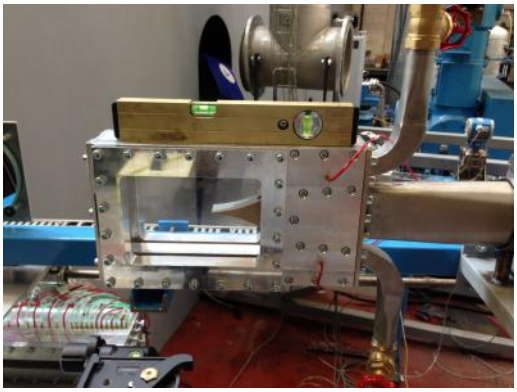

5.

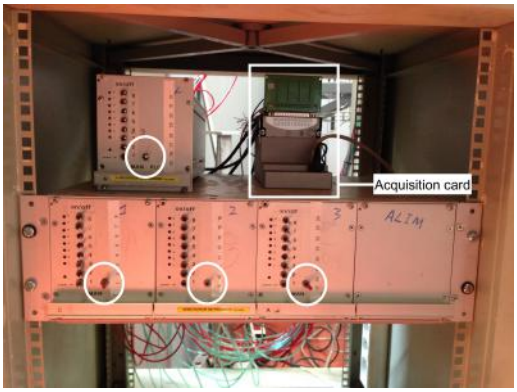

4. & 6.

2 Visualization system installation

1. Place the light source, the diaphragm, the parabolic mirror, the camera holder, the camera and the black background on the table.

2. Orient the camera towards the nozzle to verify that the visualization zone is in the center of the lens. If this is not the case the visualization table has to be lifted up or lowered down

(check afterwards that the table is still horizontal).

3. Place the diaphragm and the parabolic mirror on the same level as the camera lens.
4. Move the mirror towards or away from the diaphragm until the distance between them is equal to the focal distance of the parabolic mirror. This is done by trying to get the reflected light point to be as close to the center of the diaphragm as possible. Once it is done, lock the mirror holder.
5. Place the filter on the table and orient it so that the light rays coming from the mirror are reflected towards the center of the camera's objective.
6. Test the shadowgraph by cracking a match ahead of the parabolic mirror and observing it with the camera.

Shadowed/lightened strips on the upper/lower extremities of the canal mean that the diaphragm or the mirror are not set at the correct height.

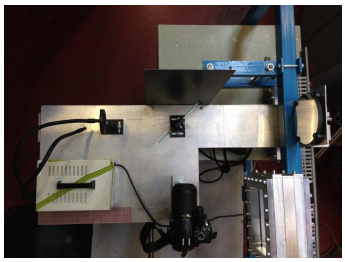
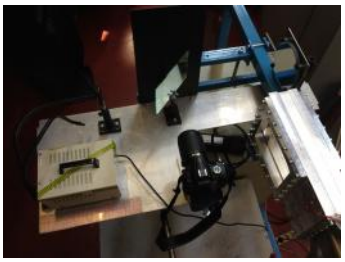
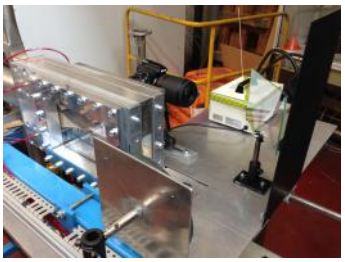

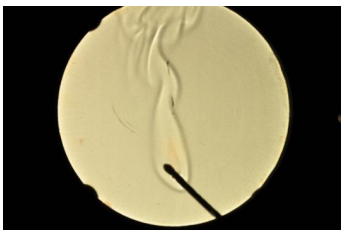
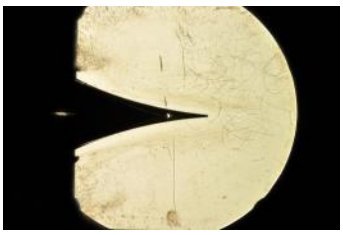

3 Start up of the user interface

1. Turn on the Dell computer LATITUDE 50 with reference number 1o0.069, password being: "labo".
2. Plug in the wire from the multiplexer as well as the USB wire connected to the data acquisition box.
3. On the desktop go to the folder LABO TUYERE AEROSPIKE then launch the file LABO TUYERE.LLB to open LABVIEW.
4. Check that the acquisition board and the internet wire are connected going to: TOOLS → MEASUREMENTS & AUTOMATION EXPLORER... → NI USB-6341 "DEV 3" → AUTO-TEST. If it fails, click on FREE CHASSIS then on BOOK CHASSIS then re-run the auto-test. Close the window once both auto-tests are completed.

5. Click on the EXECUTE arrow on the top left corner of the LABVIEW window, the will open the user interface.
6. Type in the atmospheric pressure and temperature which can be read on the digital weather station in the lab. Type in the air tank pressure ($[bar]$) in the top left corner of the window.
7. Check that the MODE is on AUTOMATIC, leave it that way during the whole session.
8. Check that the pilot pressure is on 0 $[bar]$ for the start of the experiment.

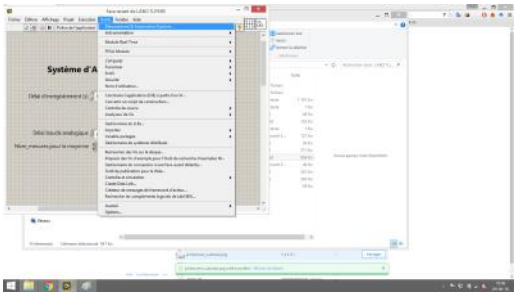

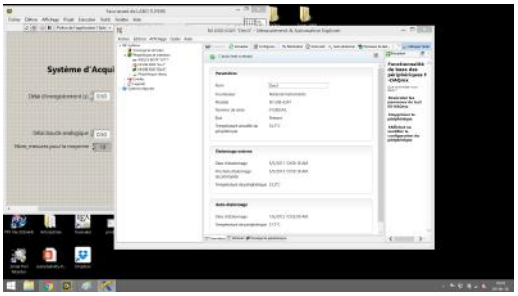

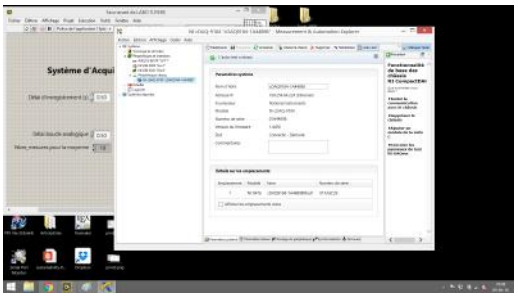

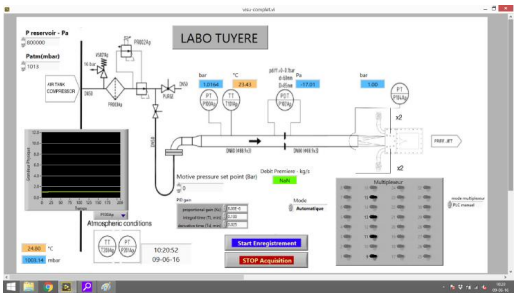

4 Starting up the compressor

1. Check that the three valves between the compressor and the test bench are closed.
2. Check on the compressor that the only opened valve is the one linking the compressor to the air tank.
3. Check that no secondary circuit is open (ask someone from AF COMPRESSORS who is responsible for the compressor).
4. Turn the black knob of the grey housing of a quarter of a turn so that it is in position 1. This will turn the compressor on and PRÊT À DÉMARRER should be written on the interface screen.
5. Push the menu button (F1) on the bottom left.
6. Click the P100 - OPERATEUR icon.
7. Set the load pressure to 8 *bar* and the unload pressure to 7.5 *bar*, and press ENTER.
8. Hold the green button down until a small F appears on the upper right corner of the screen.

9. Leave the compressor in Mise à vide forcée mode for one minute in order to allow the it to warm up.
10. Push the Reset button (F8) on the bottom right to start loading the air tank.
11. Check on the screen that the pressure rises up to 8 [*bar*] and then runs unloaded once this step is done.

8. & 9.

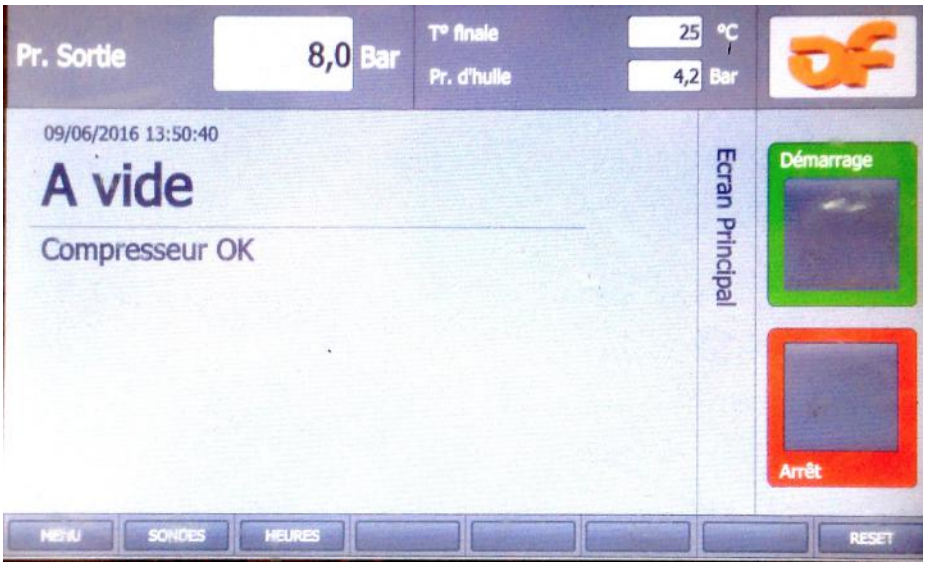

11.

5 Lab procedure

1. Close the red valve towards the test bench and the grey valve downstream the air tank and open the red bypass valve.

2. Set the pilot pressure at 1.2 [*bar*] using the user interface and press enter.
3. Open partially the grey valve connecting the air tank to the test bench and let the air flow through the bypass during 10 to 15 seconds. This cleans the air tank from any possible dirt or particles that might damage the nozzle.
4. Put the motive pressure at 0 *bar*.
5. Open the red valve towards the test bench and then close the bypass valve.
6. Set the wanted pilot pressure and start the lab session with the students. It is better to change the pressure progressively and avoid pressure changes of more than 3 [*bar*].

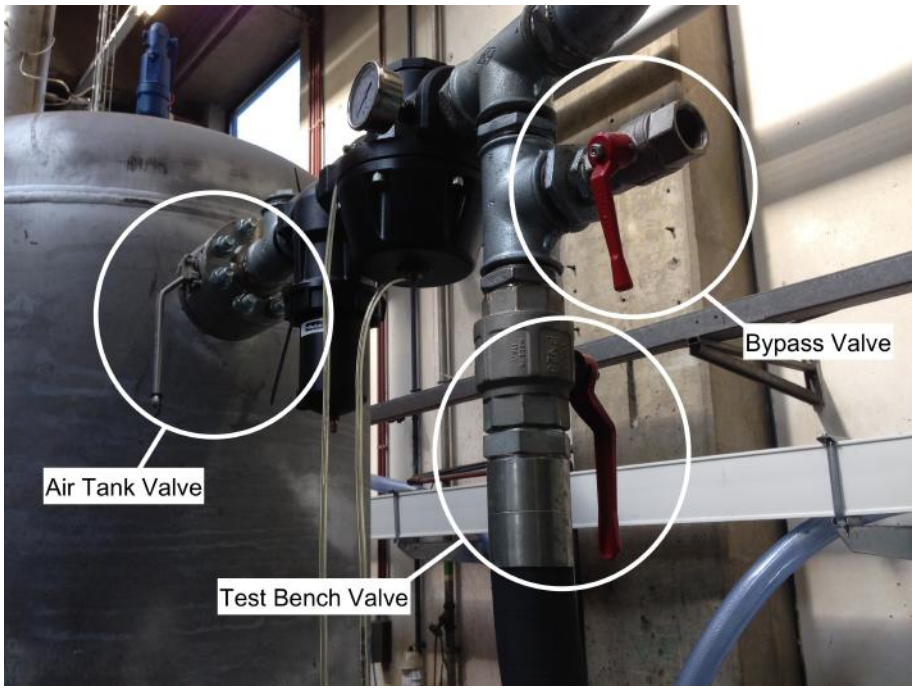

Figure 5: The different valves.

6 Stopping the compressor

1. Set the pilot pressure to 0 [*bar*] then press ENTER.
2. Hold the green button on the interface of the compressor until the message MISE À VIDE FORCÉE appears on the screen.
3. Set the pilot pressure to 2 [*bar*] to empty the air tank. Wait until no more air flows.
4. Set the pilot pressure to 0 [*bar*] then press ENTER.
5. Close the two valves on the air tank and the test bench (the grey one and the red one).
6. Open the valve placed on the bottom of the air tank (below the grey one) in order to make sure that the air tank is completely empty. Close the valve once it is done.

7. Hold the red button down until the compressor stops.
8. Turn the black knob of the compressor back on the position 0.

Bibliography

[1] Aerospike/bell nozzle exhaust plume comparisons. http://www.k-makris.gr/RocketTechnology/Nozzle_Design/nozzle_design.htm. Last online access 18/03/2016. , 3

[2] Altitude compensation effect of an aerospike nozzle. http://www.aerospaceweb.org/design/aerospike/compensation.shtml. Last online access 10/06/2016. , 8

[3] Definition of the constringence, or abbe number. https://en.wikipedia.org/wiki/Abbe_number. Last online access 15/02/2016. 39

[4] Defintion of the refractive index. http://www.britannica.com/science/refractive-index. Last online access 15/02/2016. 39

[5] Exhaust gases' diamond pattern. http://www.allstar.fiu.edu/aero/rocket3.htm. Last online access 08/06/2016.

[6] International standard for differential pressure flow-meter. http://www.iso.org/iso/fr/catalogue_detail?csnumber=28064. Last online access 28/05/2016. 29

[7] Mechanical properties of pmma. http://www.matbase.com/material-categories/natural-and-synthetic-polymers/commodity-polymers/material-properties-of-polymethyl-methacrylate-cast-cast-acrylic-pmma-cast.html#properties. Last online access 23/02/2016. 39, 40

[8] Optical and mechanical properties of crown glass (n-bk7 and others). http://www.crystran.co.uk/optical-materials/optical-glass-n-bk7-and-others. Last online access 23/02/2016. 39

[9] Optical and mechanical properties of fused quarz. http://www.quartz.com/gedata.html. Last online access 23/02/2016. 39

[10] Optical properties of pmma. http://refractiveindex.info/?shelf=organic&book=poly(methyl_methacrylate)&page=Szczurowski. Last online access 23/02/2016. 39

[11] Shadowgraph technique. http://www.thermopedia.com/content/1117/. Last online access 12/05/2016. , 30

[12] Theory overview of flow measurement using differential pressure devices based on iso-5167 standard. http://www.arian.cl/downloads/manarian_flow_cad_software.pdf. Last online access 28/05/2016.

[13] E. Besnard, H. H. Chen, and T. Mueller. Design, manufacturing and test of a plug nozzle rocket engine. Technical report, California State University, 2002.

[14] P. Brenders and M. Sauzeix. *Les nouveaux Précis: Optique MPSI-PCSI-PTSI*. 2003. 39

[15] P. Chatelain. *MECA2323 Aérodynamique des écoulements externes, Partie aérodynamique compressible*. 2012.

[16] D. J. Choudhari and U. V. Asolekar. Efficiency analysis of an aerospike nozzle. *IJERA*, 17:146 – 150, 2012.

[17] A. Davidhazy. *Introduction to shadowgraph and schlieren imaging*. 2006. 30

[18] L. Davidson. *Fluid mechanics, turbulent flow and turbulence modeling*. 2015.

[19] K. Gevers and T. Libbrecht. Conception et réalisation d'un banc d'essai pour la mesure et la visualisation d'écoulements supersoniques en canal. Master's thesis, École Polytechnique de Louvain, 2015. , 4, 28, 31, 34, 39

[20] G. Hagemann, H. Immich, T. V. Nguyen, and G. E. Dumnov. Advanced rocket nozzles. *Journal of Propulsion and Power*, 14:620 – 634, 1998.

[21] I. Hystad. Numerical modelling of turbulent boundary layer. Master's thesis, NTNU - Trondheim, 2014.

[22] J. J. Korte, A. O. Salas, H. J. Dunn, and N. M. Alexandrov. Multidisciplinary approach to aerospike nozzle design. Technical report, NASA, 1997.

[23] P. Lau. Calculation of flow rate from differential pressure devices - orifice plates. http://www.ematem.org/Dokumente/2008_lau_calculat.pdf. Last online access 28/05/2016. 29

[24] V. K. Levaka and S. R. K. Design and flow simulation of truncated aerospike nozzle. *IJRET*, 03:122 – 131, 2014.

[25] C. D. Ltd. Openfoam user guide. `http://cfd.direct/openfoam/user-guide/`. Last online access 10/06/2016.

[26] M. Onofri. Plug nozzles: summary of flow features and engine perfomance. *American Institute of Aeronautics & Astronautics*, 40:1 – 25, 2002.

[27] Rocketdyne. Altitude compensation. `http://www.aerospaceweb.org/design/aerospike/figures/fig11a.jpg`. Last online access 08/06/2016.

[28] S. Sanoob, M. Prince, and B. Sundar. Numerical analysis of aero-spike nozzle for spike length optimization. *Impact Journals*, 1:1 – 14, 2013.

[29] J. R. Simmons. Design and evaluation of dual-expander aeropsike nozzle upper stage engine. Technical report, Air Force Institute of Technology, 2006.

[30] P. A. Thompson. *Compressible-fluid dynamics*. 1972.

[31] C.-H. Wang, Y. Liu, and L.-Z. Qin. Aerospike nozzle contour design and its performance validation. *Acta Astronautica*, 64:1264 – 1275, 2009.

[32] G. Winckelmans. *MECA2322 Mécanique des Fluides et Transferts II: partie sur les écoulements compressibles*. 2009.

[33] G. Winckelmans and V. Legat. *MECA1321 Mécanique des Fluides et Transferts I: partie sur les écoulements turbulents*. 2015.

[34] T. Zebbiche and Z. Youbi. Supersonic plug nozzle design and comparison to the minimum length nozzle configuration. *KSAS International Journal*, 7:27 – 42, 2006.

Rue Archimède, 1 bte L6.11.01, 1348 Louvain-la-Neuve **www.uclouvain.be/epl**